Development of high performance distributed acoustic sensors based on Rayleigh backscattering

By: **Leonardo Marcon**

A thesis submitted in partial fulfillment of the requirements for the Degree of Doctor of Philosophy

Approved by:
Prof. Luca Palmieri, *Supervisor*

Padova, September 30th, 2019

UNIVERSITA' DEGLI STUDI DI PADOVA

Dipartimento di Ingegneria dell'Informazione
Via G. Gradenigo 6/B
35131 Padova (PD), Italy

Development of high performance distributed acoustic sensors based on Rayleigh backscattering

Ph.D Thesis

by Leonardo Marcon

Acknowledgements

TBD.

Leonardo Marcon

UNIVERSITA' DEGLI STUDI DI PADOVA

Dipartimento di Ingegneria dell'Informazione

Abstract

Ph.D Thesis

Development of high performance distributed acoustic sensors based on Rayleigh backscattering

by Leonardo Marcon

Distributed optical fiber sensing is a thriving research field that is finding practical applications in a variety of different fields including processes at extreme temperatures, security and civil engineering. The monitoring of dynamic perturbations, usually defined in the literature as distributed acoustic sensing (DAS), can be realized with excellent performance exploiting Rayleigh backscattering both in time and frequency domain. Devices implementing Rayleigh-based DAS are already commercially available.

In this thesis the results of my three-year research are presented, reporting the development of high performance distributed acoustic sensors based on Rayleigh backscattering, and their applications. The research has focused on improving the spatial resolution of the chirped-pulse phase-sensitive optical time-domain reflectometer and on developing a novel algorithm to realize real distributed acoustic sensing with high spatial resolution and high acoustic bandwidth for the optical frequency-domain reflectometer (OFDR). Finally the early results of a measurement campaign performed in collaboration with the European Organization for Nuclear Research (CERN), where distributed optical fiber sensors were used to monitor superconducting lines and magnets, are presented and discussed.

Contents

List of Figures

List of Tables

Chapter 1

Introduction

1.1 Optical fiber sensors

"When you can measure what you are speaking about, you know something about it, when you cannot express it in numbers, your knowledge is of a meager and unsatisfactory kind; it may be the beginning of knowledge, but you have scarcely, in your thoughts, advanced to the stage of science."

This sentence, which is a quote from a talk of William Thomson, 1st Baron Kelvin, perfectly represents the reason why, along the whole human history, scientists from all around the world have worked tirelessly to develop always new instruments and measuring techniques. As long as human curiosity last, there will always be a need for devices that *show* what could not be seen before, that *light* what was still in the dark, for the sake of satiating our thirst for knowledge and paving another step of the endless path called *Research*.

To measure something in a rigorous way, a sensor is required. Our senses allow to perceive roughly some physical perturbations, like the presence of visible light, a change in temperature, the macroscopic shape of an object, etc. but they do not allow to objectively estimate such quantities, nor they provide a way to accurately compare them. In the broadest definition, a sensor is a device, module, machine, technique or subsystem whose purpose is to detect events or changes in its environment and send the information in a comparable form to one or more receivers. To date, there is an endless amount of different sensors available for various applications.

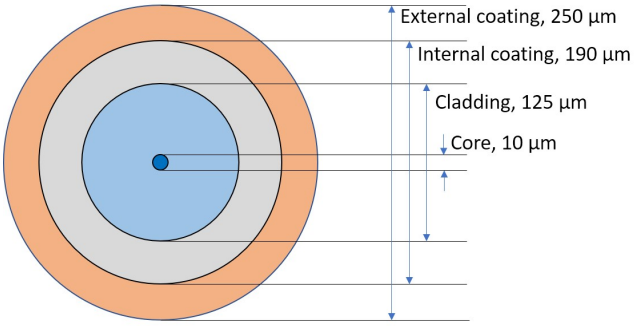

Figure 1.1. *Structure of a standard single-mode fiber*

In this thesis I will present the results of my research that has focus on optical fiber sensors (OFS). Compared to all the others sensors, OFSs guarantee simultaneously a reduced geometrical occupation, an increased resistance to electromagnetic interferences, a high robustness to harsh environments and, in particular, the possibility of performing distributed sensing thanks to the scattering phenomena occurring in the fiber.

1.2 Optical fibers history

Optical fibers are cylindrical dielectric waveguides that allow the propagation of light along the direction of their axis. An optical fiber is mostly made of extremely pure Silicon dioxide (SiO_2: Silica glass) and consists of an inner core surrounded by a cladding. The core is realized by doping the silica glass with Germanium particles that, being heavier than the Silicon ones, slightly increases the density and the refractive index. In this thesis only single-mode fibers, will be considered. The silica glass is frail and easily broken so further layers of polymeric materials, called coatings, are added to increase its robustness during the fabrication process. The structure of a fiber, not to scale, is shown in Figure 1.1.

Going back in time, the guiding of light by refraction, which is the principle that makes fiber optics possible, was first demonstrated by Jacques Babinet and Daniel Colladon in the early 1840s. John Tyndall included a demonstration of such phenomenon in his public lectures in London, 12 years later [1]. Tyndall also wrote about the property of total internal reflection in an introductory book about the nature of light in 1870 [2, 3]. In the late 19th and early 20th centuries, light was guided for entertainment through bent glass rods, while practical applications started appearing early in the twentieth century. Image transmission through tubes was demonstrated independently by the radio experimenter Clarence Hansell and the television pioneer John Logie Baird in the

1920s and in the 1930s, Heinrich Lamm showed that one could transmit images through a bundle of unclad optical fibers and used it for internal medical examinations [4]. Successively Harold Hopkins and Narinder Singh Kapany at Imperial College in London succeeded in making image-transmitting bundles with over 10,000 clad fibers, and subsequently achieved image transmission through a 75 cm long bundle which combined several thousand fibers [5]. Kapany will be the one to introduce the term Fiber Optic in the literature. The first practical fiber optic semi-flexible gastroscope was patented by Basil Hirschowitz, C. Wilbur Peters, and Lawrence E. Curtiss, researchers at the University of Michigan, in 1956. In the process of developing the gastroscope, Curtiss produced the first glass-clad fibers; previous optical fibers had relied on air or impractical oils and waxes as the low-index cladding material. A variety of other image transmission applications soon followed.The first working fiber-optical data transmission system was demonstrated by German physicist Manfred Börner at Telefunken Research Labs in Ulm in 1965, which was followed by the first patent application for this technology in 1966 [6] NASA used fiber optics in the television cameras that were sent to the moon. At the time, the use in the cameras was classified confidential, and employees handling the cameras had to be supervised by someone with an appropriate security clearance [7].

Charles K. Kao and George A. Hockham of the British company Standard Telephones and Cables (STC) were the first, in 1965, to promote the idea that the attenuation in optical fibers could be reduced below 20 decibels per kilometer (dB/km), making fibers a practical communication medium [4]. They proposed that the attenuation in fibers available at the time was caused by impurities that could be removed, rather than by fundamental physical effects such as scattering. They correctly and systematically theorized the loss properties for optical fiber, and pointed out the right material to use for such fibers—silica glass with high purity. This discovery earned Kao the Nobel Prize in Physics in 2009. The crucial attenuation limit of 20 dB/km was first achieved in 1970 by researchers Robert D. Maurer, Donald Keck, Peter C. Schultz, and Frank Zimar working for American glass maker Corning Glass Works [4]. They demonstrated a fiber with 17 dB/km attenuation by doping silica glass with titanium.

Attenuation in modern optical cables is far less than in electrical copper cables, leading to long-haul fiber connections with repeater distances of 70–150 kilometers. The erbium-doped fiber amplifier, which reduced the cost of long-distance fiber systems by reducing or eliminating optical-electrical-optical repeaters, was co-developed by teams led by David N. Payne of the University of Southampton and Emmanuel Desurvire at

Bell Labs in 1986. The emerging field of photonic crystals led to the development in 1991 of photonic-crystal fiber [8], which guides light by diffraction from a periodic structure, rather than by total internal reflection. The first photonic crystal fibers became commercially available in 2000. Photonic crystal fibers can carry higher power than conventional fibers and their wavelength-dependent properties can be manipulated to improve performance.

To date, optical fibers find wide usage in fiber-optic communications, where they actually allow Internet as we know it as they guarantee transmission over longer distances and at much higher data rates than electrical cables. Fibers are also used for illumination and imaging, and are often wrapped in bundles so they may be used to carry light into, or images out of confined spaces, as in the case of a fiberscope. Specially designed fibers are also used for a variety of other applications, some of them being fiber optic sensors and fiber lasers.

1.3 Different kinds of optical fiber sensors

Optical fiber sensors are devices that use light to convey the information which they sense. A typical optical fiber sensor system consists of the sensor itself that is probed by the input light which it modulates in accordance with the value of the measurand [9]. The rapid advances made along the years in the technology for optical fibers communications, including low-loss fibers [10], reliable laser diodes and progressively more efficient transmitting/receiving electronics, led to pioneering thoughts about applying this technology to physical [11] and chemical [12] sensing. Optical sensors can be generally divided into two categories, namely point sensors and distributed sensors. Point sensors can be generally identified with Fiber Bragg Gratings while distributed sensors exploits a scattering phenomena (Raman, Brillouin or Rayleigh) to investigate the whole length of the fiber [13].

A fiber Bragg grating (FBG) is a reflective structure in an optical fiber resulting from a periodic modulation of the effective refractive index in the core of the fiber over a length of a few millimeters or centimeters [14, 15]. The FBG reflects only the wavelength λ_B corresponding to $m\lambda_B = 2n_{eff}\Lambda$ where Λ is the grating period. Any stress acting on the FBG (strain or temperature) causes a variation of the grating period, thus inducing a corresponding change in the Bragg wavelength λ_B. The good sensitivity, wavelength

encoding and low dependence of power intensity makes these devices very attractive to the sensor community [13].

The term distributed measurement indicates that the measurement system allows determination of the spatial distribution of the measured parameter [14]. Distributed sensing techniques are based on the recording and analysis of the scattered light at every location along the fiber. Light scattering is associated with inhomogeneities in the propagation medium. Different types of inhomogeneities give rise to different scattering phenomena, ranging from density fluctuation generating Rayleigh scattering to thermally excited acoustic waves (or phonons) and molecular vibrations causing Brillouin and Raman scattering.Distributed sensing techniques are based on the recording and analysis of the scattered light at every location along the fiber. Light scattering is associated with inhomogeneities in the propagation medium. Different types of inhomogeneities give rise to different scattering phenomena, ranging from density fluctuation generating Rayleigh scattering to thermally excited acoustic waves (or phonons) and molecular vibrations causing Brillouin and Raman scattering [13]. Distributed sensors can be realized either in time domain, by sending single light pulses to interrogate the fiber or in frequency domain by using broadband CW signals.

1.4 Thesis structure

In this thesis the main results achieved during my three-year Ph.D. program will be presented. The researches can be mainly divided into three temporal slots, with the first, the longest, spent at University of Padova working mostly on optical frequency domain reflectometry; the second, spent at Universidad de Alcala‘ working on optical time domain reflectometry; and finally the third, spent at the European Organization for Nuclear Research (CERN) collaborating on the project MAG-DAS.

To guarantee a clearer description of the different topics, the structure of the thesis will be organized as follow:

In chapter 2, the physics of the scattering phenomena occurring in a standard optical fiber, namely Raman, Brillouin and Rayleigh, will be reviewed. Rayleigh scattering will be analyzed in detail as it is the basis of all the schemes and devices researched during my Ph.D. program. A pragmatic review of the thermo-optic and elasto-optic effects will be presented, highlighting the issues and the features of interest.

In chapter 3, the original results of my research on optical time domain reflectometry (OTDR), and in particular on the performance of the chirped-pulse ϕ-OTDR will be presented. After introducing the already standard experimental setup, a novel mathematical model describing the stress-induced virtual perturbations affecting the measurement is described and its experimental validation is proposed. Afterwards, the issue of the limited spatial resolution achievable with time domain setups is tackled and an original method, based on sub-band processing, that mitigates the problem by guaranteeing a 15-fold spatial resolution improvement is described.

In chapter 4, the focus be on optical frequency domain reflectometry (OFDR) where, after describing the standard setup and highlighting its performance and limitation, a novel algorithm to realized high-resolution, high-bandwidth distributed acousting sensing is proposed. Such algorithm is one of the firsts to exploit the phase of the backscattering signal which changes linearly with the applied perturbations.

Finally, in chapter 5, the early results of the experiments performed at the main laboratories of the European Organization for Nuclear Research (CERN), during our collaboration in the European Project MAG-DAS, will be presented. Thanks to the uniques instrumentations available in their laboratories, the thermal response of different samples of fibers with specific thermal properties have been evaluated at cryogenic temperature as low as 5 K. Thanks to the calibration curves extracted from such measurements, the distributed monitoring of the cooldown of a superconducting power cable have performed, showing results in agreement with the electrical sensors. Finally the cooldown and the powering of an HTS magnet have been monitored highlighting unexpected features and effects that could not be observed before with conventional sensors.

Bibliography

[1] R. J. Bates, "Optical Switching and Networking Handbook," New York: McGraw-Hill, (2001).

[2] J. Tyndall, "Total Reflexion", Notes about Light, (1870).

[3] J. Tyndall, "Six Lectures on Light," New York: D. Appleton, (1873).

[4] J. Hecht, "City of Light: The Story of Fiber Optics (revised ed.)," Oxford University (2004).

[5] H. H. Hopkins, and N. S. Kapany, "A flexible fiberscope, using static scanning", Nature, **173**(4392), 39–41 (1954).

[6] M. Börner, "Electro-optical transmission system utilizing lasers", US patent (1966).

[7] Nasa, "Lunar Television Camera. Pre-installation Acceptance Test Plan," NASA, (1968).

[8] P. Russell, "Photonic Crystal Fibers," Science, **299**(5605), 358–62 (2003).

[9] A. H. Hartog, "An Introduction to Distributed Optical Fibre Sensors", CRC Press (2017).

[10] D. B. Keck, R. D. Maurer, and P. C. Schultz, "On the ultimate lower limit of attenuation in glass optical waveguides," Appl. Phys. Lett., **22**(7), 307–309 (1973).

[11] J. A. Bucaro, H. D. Dardy, and E. F. Carome, "Optical fiber acoustic sensor," Appl. Opt., **16**(7), 1761–1762 (1977).

[12] J. O. W. Norris, "Current status and prospects for the use of optical fibers in chemical analysis. A review.", Analyst, **114**(11), 1359–1372 (1989).

[13] D.A. Krohn, T. MacDougall, and A. Mendez, "Fiber optic sensors: fundamentals and applications," Bellingham, WA: Spie Press (2014).

[14] L. Thévenaz, "Advanced fiber optics," EPFL press, 2011.

[15] A. Othonos and K. Kalli, "Fiber Bragg gratings: Fundamentals and Applications in Telecommunications and Sensing," Boston: Artech House, 1999

Chapter 2

Scattering in optical fibers

2.1 Introduction

When light travels through a transparent medium such as silica glass, most of the energy propagates forward, experiencing a loss from the medium's attenuation. However, a small portion of the light undergoes scattering, which is the diffusion of a light beam into a multitude of other beams radiated in a range of directions as a result of the physical interaction between the lights photons and the matter of the transmitting medium [1]. There are several scattering mechanisms that occur in silica glass [2], the most relevant being Rayleigh, Raman, and Brillouin scattering. Rayleigh scattering is an elastic scattering phenomenon which occurs when photons collide with inhomogeneities in the waveguide. Such inhomogeneities can include voids, density variations, impurities, composition fluctuations, structural variations, and other nanoscopic defects of dimension much lower than the optical wavelength [3]. Raman scattering is an inelastic scattering phenomenon and occurs when traveling photons interact with thermally excited molecular vibrations [4]. Finally, Brillouin scattering is another inelastic scattering phenomenon which occurs when traveling photons interact with bulk structural vibrations [5].
Any incident wavelength will produce the scattering effects, but their effects could be stronger or weaker depending on the given scattering effect and its intrinsic wavelength dependence. Furthermore, scattering effects can be further classified as either spontaneous or stimulated. Spontaneous scattering refers to a linear process where the interaction between the light's photons and the scattering centers are not perturbed by the incident light wave. Conversely, when the optical intensity of the traveling light wave increases above a certain level (threshold), the excess light energy modifies the

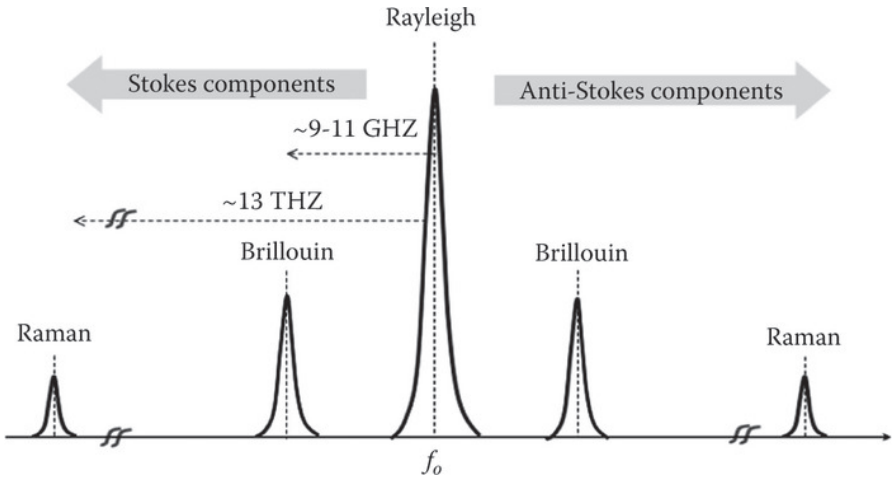

Figure 2.1. *Scattering spectrum for a standard optical fiber*

scattering properties of the medium resulting in a stronger and more efficient scattering process, or stimulated scattering [1]. While Raman and Brillouin scattering can be either spontaneous or stimulated, Rayleigh is intrinsically spontaneous.
In this chapter the Raman and Brillouin scattering processes will be briefly introduced while the Rayleigh backscattering will be analyzed in detail. Then the thermo-optic and the elasto-optic effects will be described with a particular focus on their temperature dependence.

2.2 Scattering processes

In optical fibers made of silica glass (amorphous SiO_2) there are three main scattering phenomena occurring, namely Raman, Brillouin and Rayleigh. Scattering phenomena can be elastic, when the energy of the photons constituting the optical wave does not change after the interactions with the medium constituents, or inelastic, when energy is exchanged between the photons and the medium constituents. For the case of elastic scattering the dimension of the constituents with respect to the wavelength of the optical wave determine the dominant phenomena. If the wavelength is much larger than the constituents the dominant phenomena is Rayleigh scattering, otherwise Mie scattering prevails. In our case Mie scattering can be neglected as the optical wavelengths generally considered are tens of times larger than the dimensions of the fiber inhomogeneities. Based on the amount of the energy exchanged between photons and medium constituent and on the nature of the energy exchange, inelastic scattering phenomena can be divided into Raman scattering and Brillouin scattering [6]. Since a photon energy change can be

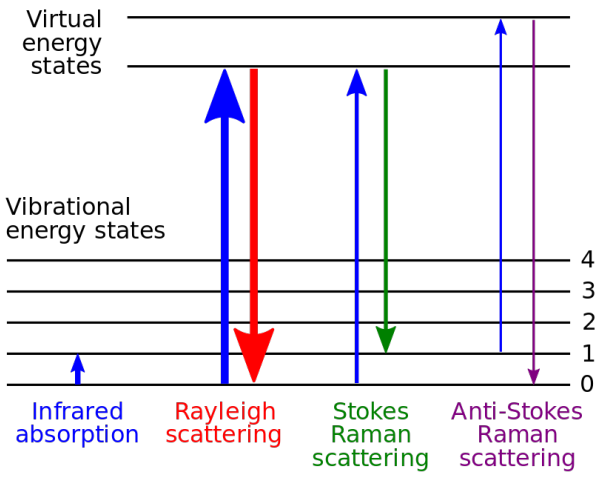

Figure 2.2. *Energy-level diagram showing the states involved in Raman spectrum.*

seen as a frequency shift, it is interesting to observe the scattering spectrum for standard optical fibers, which is shown in Figure 2.1.

2.2.1 Raman scattering

Spontaneous Raman scattering is an inelastic process resulting from the interaction of the incident light beam with vibrational modes of the glass molecules. Raman scattering radiates scattered photons that have been upshifted (anti-Stokes components) or downshifted (Stokes components) with respect to the incident optical frequency. As can be seen in Figure 2.2 Raman scattering can be viewed as an electron transition process where an incident photon is absorbed and produces a transition from a vibrational-rotational level of the ground state to a virtual (time-dependent) excited state, followed by a transition back down to a level adjacent to the starting level.

Since the vibrational levels of the ground state are populated according to Boltzmann's law, the electronic populations at higher levels increase as the temperature rises. Therefore, the anti-Stokes components, which experience an energy gain, are particularly sensitive to temperature, and thus are used as the detection mechanism in distributed fiber sensing systems. At high temperatures the molecular vibrations are highly excited, and the Raman sidebands are of equal intensity. Conversely, at very cold temperatures, the bands practically disappear. Hence, temperature sensing via Raman scattering has intrinsic limitations on both the upper and lower temperature range.

Spontaneous Raman scattering is usually negligible since its intensity is at least three

order of magnitude lower than that of Rayleigh scattering. However, if a sufficiently intense optical pump is injected in the fiber the scattering process becomes self-stimulated due to a third-order non-linear process, as the temporal beating between the pump and Stokes waves stimulates the vibrational states of silica molecules. Such stimulus grows rapidly as an increasing pump energy is transferred to the medium. In the stimulated regime, the growth of the Stokes signal is exponential and much more efficient than in the anti-Stokes scattering, which requires populated vibrational levels. The Raman frequency shift in fused silica is $\Delta f_R = 13.2\text{THz}$, which corresponds to the inverse of the response time of molecular vibrations [7]. The Raman shift can be significantly engineered by use of different dopants inside the fiber core [8] while two factors contribute to enhance the Raman gain in fibers: the relatively high doping of the core or a reduction of the effective core area, leading to higher power confinement and therefore larger gains. These modified fibers are often used in Raman amplifiers and lasers.

2.2.2 Brillouin scattering

Spontaneous Brillouin scattering is an inelastic scattering process between the photons of an incident light beam and the density (index) variations induced on the medium by a pressure wave (acoustic wave) traveling within the glass material. This acoustic wave may be set off spontaneously by thermally induced molecular vibrations in the structural lattice. Because the pressure variations are periodic, the induced refractive index fluctuations act as a distributed reflector (similar to the fiber Bragg gratings which are fixed periodic variation of the effective refractive index of the core of the fiber), reflecting light in a given direction and of a given wavelength as can be seen in Figure 2.3. Furthermore, a Doppler frequency shift is induced between the incident beam and the scattered ones because of the relative movement and difference in propagation velocity between the light beams and the traveling acoustic wave. In other words, the scattered light beams are reflected back from a moving grating. Diffraction from a retreating acoustic wave produces a downshifted scattered beam or Stokes component. Conversely, a refracted beam from an approaching acoustic wave produces an upshifted scattered wave or anti-Stokes component. The Doppler-frequency shift is maximum in the backward direction and zero in the forward direction. The frequency shift depends on the acoustic velocity in the glass which is a function of the refractive index. Since the refractive index is a function of temperature and strain, as described in the next

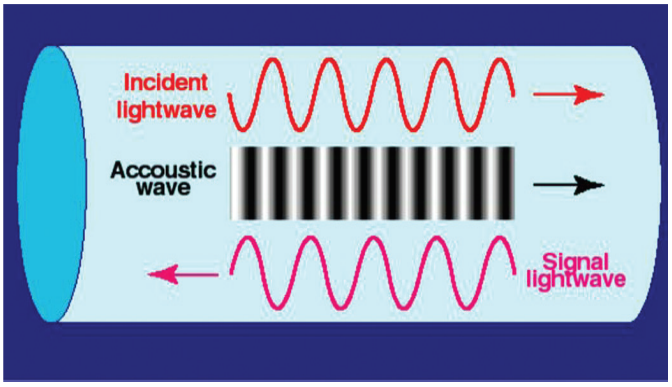

Figure 2.3. *Basic Brillouin scattering mechanism.*

section, it allows for the intrinsic capability of Brillouin scattering to perform distributed temperature and strain measurements by measuring the spectral shifts on the Stokes and anti-Stokes scattering spectra [1].

Compared to Raman, the Brillouin scattering spectrum consists of very narrow (less than 100 MHz) Stokes and anti-Stokes spectral lines, shifted by only a few tens of gigahertz from the incident-light wavelength. These quantitative differences have made Brillouin scattering far more versatile than Raman scattering in distributed sensing for the many reasons. Firstly, Brillouin scattering in glasses is sensitive to strain and temperature in its frequency and intensity, whereas the Raman strain-dependent frequency shift is only readily detected in crystalline materials [9, 10]. Thus, the ability to measure precisely the frequency shift of the Brillouin scattering has allowed distributed sensing technology to provide strain as well as temperature data. Moreover some interrogation approaches even allow the strain and temperature to be determined independently [11]. Secondly, the very narrow linewidth of the Brillouin process enabled Brillouin measurements to be carried out over significantly long distances [12]. Finally, the spontaneous Brillouin backscatter signal is substantially stronger (by about one order of magnitude) than the Raman anti-Stokes backscatter, although that advantage is mitigated by the weaker sensitivity.

The previously described process represents the spontaneous form of Brillouin scattering. A stimulated version also exists that has practically the same mechanisms but a slightly different inducing cause. Stimulated Brillouin scattering (SBS) is generated by an intense incident optical signal that has an optical power above the spontaneous Brillouin threshold. This intense light wave causes mechanical vibrations in the fiber's glass molecules due to a third-order non-linear process, inducing a periodic index Bragg grating just as was the case in the spontaneous Brillouin scattering mechanism. Since

the efficiency of the non-linear process is not high, a long interaction length between the fiber and the pump is required, as well as a highly coherent light source.

2.2.3 Rayleigh scattering

Scattering is the process by which small amounts of forward-traveling light is redirected by interactions with inhomogeneities in the glass from which the fiber is formed. The most prominent of these interactions, Rayleigh scattering may arises from voids, impurities, composition fluctuations, structural variations, and other nanoscopic defects of the medium structure, but in optical fiber the main contribution comes from thermodynamically driven fluctuations in the density of the glass. When the fiber is drawn, its principal composite material, silica, is softened at a very high temperature (≈2000°), and this results in a thermal agitation of the material molecules, thus in fluctuations in the density of the material over short distances in the order of less than 100 nm. As the fiber exit the furnace, it is cooled at a very fast pace (less than 1 s) to temperatures well below the softening temperature (indeed, this rapid cooling is required in order to apply a protective polymer coating) and its viscosity increases rapidly as it cools. As a result, the glass becomes kinetically limited in reordering the density distribution to a value corresponding to room temperature and the inhomogeneities results frozen as they are. Statistically, the density distribution is considered equivalent to that of a material heated at a fictive temperature T_f, which, for fibers drawn at 2000°C, is around $T_f = 1500$°C. The density variations are thus randomly fixed in the fiber and form a low-level three-dimensional roughness of the refractive index which does not change in time as long as the fiber is not heated above the softening temperature [9].

Propagation of light through a dielectric medium involves the electric field polarizing the molecules through which it travels, and the molecular polarization, in turn, results in a secondary field being radiated with a phase delay. In a homogeneous medium (i.e. where the refractive index is uniform), all polarizing fields are in phase and cancel in all but the forward direction [13]. The phase shift induced in this process retards the electromagnetic wave, and this effect accounts for the slower propagation velocity compared with free space (propagation delay). Now, when the medium is slightly inhomogeneous, the regions of refractive index different from the mean may be regarded as isolated scatterers. These scatterers re-radiate a small fraction of the light in all directions, and because they are anomalies in an otherwise homogeneous medium, their polarizing

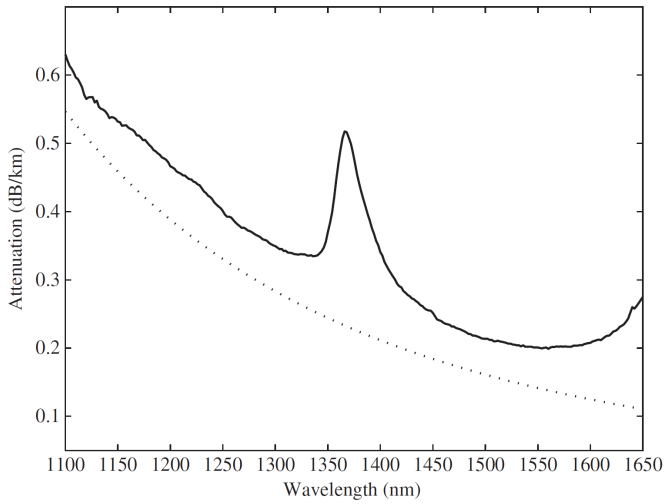

Figure 2.4. *Losses in a single mode optical fiber as a function of the wavelength (Solid line); Rayleigh scattering contribution to the losses (Dashed line)*

fields are not completely canceled. They may then be regarded as individual dipoles that radiate with a toroidal electric field pattern about the dipole axis. The accumulation of all such scatters gives rise to Rayleigh scattering. Since the light diffused by Rayleigh scattering radiates in all directions, it does not necessary couple back to a guided mode of the fiber and most of it is then lost. Losses due to Rayleigh backscattering are the main contribution to the attenuation experienced by light signal during propagation the optical fibers. It can be shown [14, 15] that the attenuation coefficient α_{rs} [dB/km] related to this contribution can be estimated by:

$$\alpha_{rs} = (10 \log e) \frac{8\pi^3}{3\lambda^4} \left(n^2 - 1\right)^2 k C_T T_f \tag{2.1}$$

where n is the fiber mean refractive index, k is the Boltzman constant, C_T the isothermal compressibility and T_f is the aforementioned equivalent temperature.

In modern telecommunication fibers, Rayleigh scattering dictates the minimum achievable loss. The usual attenuation spectrum for a typical single-mode, step-index index fiber is plotted as a function of wavelength in Figure 2.4. As can be seen, for single-mode optical fibers the total attenuation is in the neighbor of 0.2 dB/km (0.35 dB/km) at 1550 nm (1310 nm) and the contribution due to Rayleigh scattering is about 0.15 dB/km (0.28 dB/km) [6]. The total loss (solid line) shows a minimum in the so called 'third window', near 1550 nm: at this wavelength, the reduction in loss for increasing wavelength shown by Rayleigh scattering starts being compensated by the infrared absorption. Rayleigh scattering is elastic: to first order, the energy of the scattered photons is the same as

that of the incident photons, so the wavelength is preserved in the scattering process. Rayleigh scattering also, by and large, preserves the polarization of the incident light: in silica, about 5% of the scattered light intensity emerges in the polarization orthogonal to that of the incident light, whereas 95% remains in the original polarization. The depolarization effect is thought to be due to a small-scale anisotropy of the polarizability of microscopic scattering regions in the glasses that are randomly orientated [16]. Thus, if scatterers are anisotropic and not aligned to the incident electric field, the induced dipoles do not align perfectly to that field. Therefore, in such a case, the scattered light has a component in the orthogonal polarization to that of the incident light. However, in order to observe the depolarization effect in the backscattered light, the fiber must be of the single-mode type: in multimode fibers, the state of polarization is generally scrambled, unless extreme care is taken to launch only the lowest-order mode and then to prevent mode-coupling.

Of the whole amount of light scattered, a small percentage is reflected in the opposite direction with respect to the propagation of the light. This little echo is called Rayleigh backscattering and allows to use standard optical fiber as a sensor. Rayleigh scattering in optical fiber is per se independent of almost any external physical field for a wide range of conditions [13, 17, 18]. Actually, in Rayleigh-based distributed optical fiber sensors the scattering itself is used only to track and to reveal propagation effects (in the most wide sense), which are the real sensing mechanisms. These propagation effects include attenuation and gain, phase interference and polarization variation, and all of them can be exploited to implement a Rayleigh-based distributed sensor. It's worthwhile remarking that these propagation effects may affect also Raman- and Brillouin-based sensors, but they are usually neglected just because Raman and Brillouin scattering offer direct sensing mechanisms. Because of this peculiar characteristic, Rayleigh-based distributed sensors are potentially sensitive to many different physical fields, beside temperature and strain.

2.3 Thermo-optic and elasto-optic effects

As discussed in the previous section, Rayleigh backscattering allows to realize a distributed sensor from a standard optical fiber by tracking the perturbation-induced changes in the propagation of a known light signal. Since in this thesis the focus is in distributed sensing of vibration events and temperature changes, which influence the

local refractive index of the perturbed fiber section through the so called thermo-optic and elasto-optic effect, it becomes fundamental to describe the practical equations used to model such phenomena. A complete analysis can be found in the references [19, 20] where the model are derived from a material science and molecular physics point of view.

The thermo-optic effect can be represented as a local variation of the optical fiber mean refractive index n induced by a temperature change ΔT acting over a section S of the fiber:

$$n(z) = \begin{cases} n, & z \notin S \\ n + \alpha_{TO}(T)\Delta T, & z \in S \end{cases} \tag{2.2}$$

where $\alpha_{TO}(T)$ is called thermo-optic coefficient and as can be seen is a function of the absolute temperature of the fiber T. While for temperatures close to the standard room temperature, i.e. $T_r \approx 300$ K, such coefficient has a known value and can be considered constant, thus making eq. (2.2) linear, for temperatures $T \neq T_r$ or if ΔT is intense, the non-linear behavior of the coefficient must be taken into account. Unfortunately the development of a complete theoretical model for the temperature-dependent thermo-optic coefficient $\alpha_{TO}(T)$ is a difficult task since it depends not only on the glass used, but also on the dopant of the fiber core, on the coating applied to the fiber and by many other side parameters. As we will see in details in Chapter 5 the easiest way to account for the non-linear behavior of $\alpha_{TO}(T)$ for a particular fiber under test is to experimentally monitor a sample of the same fiber during controlled thermal cycles over the temperature interval of interest. From such data it is possible to create an ad-hoc temperature vs thermal response map that can be applied during the actual experiments. It is important to note however, that such map will not allow to extract the real evolution of the thermo-optic coefficient, since it will includes also the effects of length variations and strain induced by different expansion/contraction of the coating with respect to the silica glass. As we will see, the onset of such contemporaneous phenomena is not necessary a drawback since it will allow to perform temperature sensing even at cryogenic temperatures, where the pure thermo-optic coefficient of silica is negligible [19].
When a strain acts on a section S of the fiber, it induces a deformation of the relative positions of the scattering centers in S and it stimulates a change in the local refractive index through the elasto-optic effect. The deformation changes the phase relations

between the coherent backscattering contributions generated by different scattering centers, shifting the local interference pattern. The elasto-optic effect, or photoelasticity, deals with the artificial change in the refractive index of a solid under the application of a mechanical stress/strain, and was initially quantified by Neumann in 1841 and then theoretically analyzed by Pockels. The elasto-optic effect can be represented with a model analogous to the one developed for the thermo-optic effect:

$$n(z) = \begin{cases} n, & z \notin S \\ n + \alpha_{EO}(T)\Delta\varepsilon, & z \in S \end{cases} \tag{2.3}$$

where $\Delta\varepsilon$ is the strain applied to a section S of the fiber and α_{EO} is the elasto-optic coefficient. Without entering too much in the field of material science, for moderate strain $\Delta\varepsilon$ an equation representing α_{EO} can be identified:

$$\alpha_{EO} = -\frac{1}{2}n^3\left[(1-\nu)p_{1,2} - \nu p_{1,1}\right], \tag{2.4}$$

where ν is the silica's Poisson ratio defined as the negative of the ratio of the transverse strain to the axial strain and $p_{1,1} \approx 0.113$ and $p_{1,2} \approx 0.252$ are the elements of interest in the photo-elastic tensor of silica glass. The shift of the local backscattering signal pattern induced by a strain is usually dominated by the effects of the physical deformations, which usually exhibits an opposite sign than the elasto-optic effect. Moreover, similarly to the case of the thermo-optic effect, the elasto-optic coefficient becomes negligible at cryogenic temperature.

The thermo-optic and the combination of physical deformation/elasto-optic effects generates completely analogous changes in the refractive index of the fiber, which are indistinguishable by a standard distributed measurement based on Rayleigh backscattering. This has been an important issue since the very early stages of the research in this field and many setups have tried to solve the issue. While different schemes have been tested, the most common solution consists in inserting a second independent fiber, eventually with slightly different thermal or elastic properties, close to the actual sensing fiber. By solving the linear system of equations defined measuring both time at the same time the temperature and strain changes affecting the sensing fiber can be decoupled.

Bibliography

[1] D.A. Krohn, T. MacDougall, and A. Mendez, "Fiber optic sensors: fundamentals and applications," Bellingham, WA: Spie Press (2014).

[2] R.D. Maurer, "Light scattering by glasses," J. Chem. Phys., **25**(6), 1206-1209 (1956).

[3] S. Sakaguchi, and T. Shinichi, "Rayleigh scattering of silica core optical fiber after heat treatment," Appl. Optics, **37**(33), 7708-7711 (1998).

[4] M. A. Farahani, and G. Torsten, "Spontaneous Raman scattering in optical fibers with modulated probe light for distributed temperature Raman remote sensing," J. Light. Technol., **17**(8), 1379 (1999).

[5] A. Kobyakov, M. Sauer, and D. Chowdhury, "Stimulated Brillouin scattering in optical fibers," Adv. Opt. Photon. **2**(1), 1-59 (2010)

[6] L. Thévenaz, "Advanced fiber optics," EPFL press, 2011.

[7] R. H. Stolen, J. P. Gordon, W. J. Tomlinson, and H. A. Haus, "Raman response function of silica core fibers," J. Opt. Soc. Am. B, **6**, 1159–1166 (1989).

[8] M. N. Islam, "Raman Amplifiers for telecommunications 1: Physical Principles," Springer, (2004).

[9] A. H. Hartog, "An Introduction to Distributed Optical Fibre Sensors", CRC Press (2017).

[10] R.S. Krishnan, "Temperature variations of the Raman frequencies in diamond," Proc. Indian Acad. Sci. (Math. Sci.) **24**(1), 45–57 (1946).

[11] S.M. Maughan, H. H. Kee, and T. P. Newson, "Simultaneous distributed fibre temperature and strain sensor using microwave coherent detection of spontaneous Brillouin backscatter," Meas. Sci. Technol., **12**(7), 834-842 (2001).

[12] M.N. Alahbabi, Y.-T. Cho, and T. P. Newson, "150-km-range distributed temperature sensor based on coherent detection of spontaneous Brillouin backscatter and in-line Raman amplification," J. Opt. Soc. Am. B, **22**(6), 1321–1324 (2005).

[13] I.L. Fabelinskii, "Molecular scattering of light," Plenum Press, New York (1968).

[14] R. Maurer, "Glass fibers for optical communications," Proceedings IEEE, **61**, 452–462 (1973).

[15] G . Keiser, "Optical Fiber Communications," Mc Graw Hill, 2000.

[16] R.B. Sosman, "Properties of silica," Chemical Catalog Company Inc., New York (1927).

[17] R.W. Boyd, "Nonlinear optics. 3rd ed," Newyork: Academic Press (2008).

[18] L. Palmieri and L. Schenato, "Distributed Optical Fiber Sensing Based on Rayleigh Scattering," The Open Optics Journal **7**(1), 104-127 (2013).

[19] J. Komma, C. Schwarz, G. Hofmann, D. Heinert, and R. Nawrodt, "Thermo-optic coefficientof silicon at 1550 nm and cryogenic temperatures," Appl. Phys. Lett., **101**(4), 041905 (2012)

[20] J. S. Sirkis and H. W. Haslach, "Interferometric stain measurement by arbitrarily configured surface-mounted, optical fibers," J. Light. Technol., **8**(10), 1497–1503 (1990).

Chapter 3

Optical time-domain reflectometry

3.1 Introduction

Optical time domain reflectometry (OTDR) was first proposed by Barnoski and Jensen in 1976 [1] as a novel technique to characterize the losses of a single-mode fiber. It uses a laser to send single pulses in the fiber and monitor the fiber backscattering as a function of the light round-trip time, which can be converted to positions by knowing the fiber refractive index and the speed of light. The properties of the interrogation pulse used, namely its amplitude and temporal width, determines the performance of the OTDR. Given the aforementioned time-positions duality, the spatial resolution is directly proportional to half the temporal length of the pulse [2], while the measurement range depends on the amount of power coupled to the fiber which determines the measurement signal-to-noise ratio (SNR). To increase the spatial resolution short pulses must be uses, thus reducing the power coupled to the fiber and the measurement range. The amplitude of the pulse cannot be increased arbitrarily due to the onset of non-linear phenomena, like modulation instability [3], which impair the measurement.

If the laser source used to implement the OTDR scheme is coherent, the backscattering contributions from different scattering centers sum coherently. Consequently, the backscattering signal appears affected by speckle noise, also known as Rayleigh fading noise [4, 5]. To mitigate this source of noise, the standard OTDR uses low coherence (i.e. wide bandwidth) optical pulses, so to minimize coherent interference. On the other hand, however, these fringes of interference are related to the positions of the scattering

centers, which are constant as long as the fiber is not heated up above a critical temperature in the order of several hundreds of degrees Celsius. At more practical temperatures, the so called "Rayleigh fading noise" is actually a deterministic fingerprint, unique to each fiber. When the fiber undergoes a strain or a temperature variation, the relative positions of the scattering centers changes, inducing a deterministic and predictable variation in the fringe pattern. This is exactly the basic principle of phase-OTDR (ϕ-OTDR) [6] which employs narrow-band, highly coherent optical pulses to enhance the interference fringes. ϕ-OTDR based distributed acoustic sensors (DAS) [7, 8] are the most commonly available schemes to date due to their good performance and reduced costs. ϕ-OTDR schemes share the same resolutions and measurement range of standard OTDR, thus they are more befitted to those DAS applications where a very high spatial resolution is not necessary [9, 10]. Since the effect of any perturbation acting on the fiber induces a non proportional change in the amplitude of the speckle-like pattern of the received backscattering signal, ϕ-OTDR schemes allow only qualitative measurements. Moreover, when the amplitude received is particularly low due to Rayleigh fading, the measurement may not be accurate. In recent years, many efforts have been spent to reduce such drawbacks [11–13] which can be strongly mitigated by introducing a linear chirp into the input pulse [14]. The chirped-pulse ϕ-OTDR setup guarantees a linear measurement of the perturbations, while securing an increased robustness to coherent fading and high sensitivities to temperature and strain (e.g. millikelvin and nanostrain) [15]. Such sensitivities increase the impact of distortions so far considered negligible, like the cumulative round trip time changes induced by perturbations acting on the fiber on all the backscattering components generated from further fiber sections. While the measurement error induced by such distortion is negligible in the majority of cases, even where long perimeters are monitored [10][16], if a section of the fiber undergoes an intense environmental perturbation, it may become significant. The cumulative round trip time change appears in the measurement performed with a chirped-pulse ϕ-OTDR as a distributed, homogeneous, virtual perturbation that may potentially be corrected using a suitable model. Moreover, the spatial resolution of the chirped-pulse ϕ-OTDR remains limited by the input pulse width.

While the term DAS can generally refer to any dynamic perturbation, in the literature it is principally used for strain perturbations. It it important to highlight thus that dynamic temperature sensing or hybrid dynamic temperature-strain sensors have been

developed as well. Since the temperature and strain effects are cumulative, all hybrid setups implement techniques to discriminate the two perturbations [17], e.g a combination of scattering phenomena, namely Rayleigh and Brillouin [18] or Rayleigh and Raman [19].

In this chapter the setup of a standard chirped-pulse ϕ-OTDR will be discussed and its performance will be analyzed. An original mathematical model for the virtual perturbations induced by a stress acting on the fiber, when the measurement is performed by a chirped-pulse ϕ-OTDR has been developed during my Ph.D. program. We have then experimentally validated the model by inducing a temperature change on a known span of fiber while monitoring the subsequent perturbations in a further fiber section kept at rest. The experimental results are then analyzed and compared with the theoretical ones. Finally, the results of my research on a method to improve the spatial resolution of chirped-pulse ϕ-OTDR by means of sub-bands processing, without reducing the input pulse width, will be presented.

3.2 Chirped-pulse ϕ-OTDR setup

The chirped-pulse ϕ-OTDR scheme [14] originates from the principle that a refractive index change Δn in the fiber can be compensated (in terms of the shape of the trace) by a frequency shift Δv of the pulse sent into the fiber [8]. This is the same principle as used in [20], and is typically implemented by performing a laser frequency sweep. Instead of requiring a time-consuming frequency sweep to determine Δv and calculate Δn, a single, linearly chirped pulse can be used. As we noted, a variation of the refractive index has the same effect of a variation of the pulse frequency; however, in the case a chirped pulse whose frequency is linearly varied in time, a small frequency varaition corresponds to slighlty anticipating or delaying the pulse delay. As a result, in a chirped-pulse phi-OTDR a small local variation of the refractive index manifests itself as a small anticipation/delay of the corresponding section of the backscattered trace.

Although it is a general concern in conventional ϕ-OTDR systems to have flat-phase profiles, it should be clear that the optical pulses used in a ϕ-OTDR can in principle have any arbitrary phase profile, and therefore any arbitrary spectral content. What is important to avoid is additional noise in the trace so that the phase profile does not change from pulse to pulse (i.e. that the laser source has to be strongly coherent). Therefore, except for the fact that the detection bandwidth should be higher in the

case of chirped-pulses, no extra noise source should be expected in the chirped-pulse implementation over the traditional one, and therefore similar spatial resolutions and sensing ranges should be achievable in both methods.

To describe the chirped-pulse ϕ-OTDR sensor, it is convenient to start by describing a pulse $P(t,z)$, with a rectangular intensity profile of amplitude E_0, width τ_p and an instantaneous frequency profile $\upsilon(t) = \upsilon_0 + (\delta\upsilon/2 - \delta\upsilon \cdot [t/\tau_p])$. $P(t,z)$ is therefore a linearly chirped-pulse with a spectral content $\delta\upsilon$, around a central frequency υ_0, and frequency slope $\delta\upsilon/\tau_p$. The propagation of $P(t,z)$ along an optical fiber is described by:

$$P_{std}(t,z) = E_0 rect\left[\frac{(t-\beta_1(z)}{\tau_p}\right] e^{j2\pi(\upsilon_0+\frac{\delta\upsilon}{\tau_p}[t-\beta_1(z)])(t-\beta_1(z))}, \tag{3.1}$$

where t is the time and z the position along the fiber, $z = 0$ being the fiber entrance where the pulses are launched and $t = 0$ the moment when the front part of the pulse enters the fiber in $z = 0$ and $\beta_1 = \int_0^z n_g(z)dz/c$ is the propagation delay. $rect(x) = 1$ when $0 \leq x \leq 1$ and zero elsewhere, c is the speed of light in the vacuum and $n_g(z)$ is the local refractive index of the fiber at the pulse central frequency υ_0. The spectral content $\delta\upsilon$ is assumed to be small in comparison to the center frequency and υ_0 to be away from resonant frequencies of the fiber. As the pulse $P(t,z)$ propagates along the fiber, at each instant t each infinitesimal part of $P(t,z)$ will generate a counter-propagating wave via Rayleigh backscattering. The backscattered signal is therefore continuously generated, and different parts of backscattered signals generated at different instants will overlap to produce the ϕ-OTDR signal $E(t)$, received at $z = 0$, at a given time t. The reflection of $P(t,z)$ in each location of the fiber z is described by the fiber's Rayleigh backscattering profile function $r(z)$. $E(t)$ will be given by the convolution of $P(t,z)$ and $r(z)$, for the fiber section $z \in [(t-\tau_p)\cdot c/(2n), t\cdot c/(2n)]$:

$$E(t) = \int_{z=tc/2n-\tau_p c/2n}^{tc/2n} r(z)\cdot E_0 \cdot e^{j2\pi(\upsilon_0+\delta\upsilon/2-\delta\upsilon/\tau_p(t-2\beta_1))(t-2\beta_1)} \tag{3.2}$$

Note that while the signal $E(t)$ is generated from the interference of reflections occurring in a fiber section with 1/2 of the pulse width, it accounts for the passage of the entire pulse $P(t,z)$. This characteristic is the basis for the well known fact that the spatial resolution for OTDR systems is determined by 1/2 of the pulse width. Figure 1 depicts the reflections of the pulse $P(t,z)$ as it propagates along the fiber which will generate $E(t)$. The contribution to $E(t)$ will be given by a convolution of $P(t,z)$ with the fiber sections

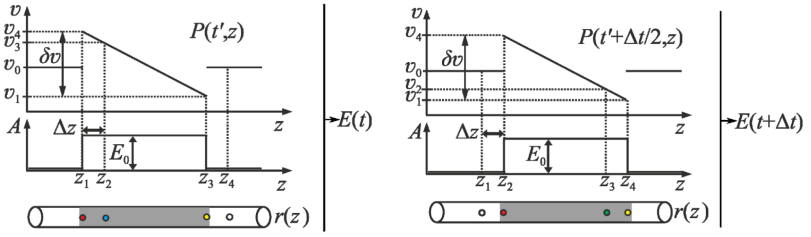

Figure 3.1. *Reflection of the pulse $P(t,z)$ as it propagates along the fiber. Reproduced with permission from [14]*

$z \in [z_1, z_2], [z_2, z_3]$, which reflect the instantaneous frequencies $\upsilon \in [\upsilon_4, \upsilon_3], [\upsilon_3, \upsilon_1]$, respectively, as shown in Figure 3.1(a). The contribution to $E(t + \Delta t)$ will be given by a convolution of $P(t, z)$ with the fiber sections $z \in [z_2, z_3], [z_3, z_4]$ which reflect the instantaneous frequencies $\upsilon \in [\upsilon_4, \upsilon_2], [\upsilon_2, \upsilon_1]$, respectively, as shown in Figure 3.1(b). For a small enough Δt, so that $[z_1, z_2], [z_3, z_4] \ll [z_2, z_3]$, then the contributions to $E(t)$ and $E(t + \Delta t)$ generated from reflections in $[z_1, z_2], [z_3, z_4]$ are essentially negligible. In this case, $E(t)$ and $E(t+\Delta t)$ can be thought of as generated from reflections of the same fiber section $[z_2, z_3]$, by pulses with frequencies $\upsilon \in [\upsilon_3, \upsilon_1]$ and $\upsilon \in [\upsilon_4, \upsilon_2] = [\upsilon_3, \upsilon_1] + \Delta\upsilon$, respectively, i.e., two pulses with a frequency shift $\Delta\upsilon$ between them. In this case, if n remains constant along $[z_2, z_3]$, then $E(t) \neq E(t + \Delta t)$. However, if a homogeneous Δn occurs, then the Δn is compensated by the frequency shift $\delta\upsilon$ and therefore $E(t) = E(t + \Delta t)$. This can be mathematically directly derived from (3.2), assuming that the contributions to the integral from $[z_1, z_2]$ (to $E(t)$) and $[z_3, z_4]$ (to $E(t + \Delta t)$ are negligible. In practice, this relation holds if Δn is small enough. The relation between these quantities can be derived by analyzing the phase difference $\phi_{i,j}$ between the backscattered waves reflected from the fiber locations z_i, z_j, similarly to what is derived in [20]:

$$\phi_{i,j} = 2\pi \frac{2n(z_i - z_j}{c} \left(\upsilon_0 + \frac{\delta\upsilon}{2} - \frac{\delta\upsilon}{\tau_p} \left[2t - \frac{2n(z_i + z_j)}{c} \right] \right) \tag{3.3}$$

From Eq. (3.3) it follows that a small variation Δn can be compensated by a longitudinal shift of the trace Δt (after neglecting terms of small amplitude and taking into account a factor of 2 owned to the fact that the pulse is reflected from a fiber section with 1/2 of the pulse length). The relationship between Δn and Δt is given by:

$$\frac{\Delta n}{n} = -\frac{1}{\upsilon_0} \frac{\delta\upsilon}{\tau_p} \Delta t \tag{3.4}$$

A similar derivation can be done for strain changes, which in addition lead to a change

in the relative positions of z_i, z_j. The measuring principle of the chirped-pulse ϕ-OTDR sensor derives from this result. If a Δn occurs at a certain location of the fiber z, then the local ϕ-OTDR pattern $E(t)$ will be longitudinal ly shifted by a Δt at that location, correspondent to the $\Delta \upsilon$ which compensates for the Δn. Note that local Δt changes among two different traces can be determined along the fiber by calculating a local correlation of the trace segments obtained for the two consecutive measurements. The measurement of Δn along the fiber then allows for distributed temperature measurements ΔT. A similar derivation can be performed for applied strains $\Delta\varepsilon$, (which are translated into shifts of the scattering positions of the fiber Δz). If a $\Delta\varepsilon$ occurs then $E(t)$ will be longitudinaly shifted by a Δt, which will be added to existing Δt caused by ΔT (if existant). The relation between Δt and the quantities ΔT and $\Delta\varepsilon$ is given by [20]:

$$\begin{aligned} -\frac{1}{\upsilon_0}\frac{\delta\upsilon}{\tau_p}\Delta t = \frac{\Delta\upsilon}{\upsilon_0} \approx -0.78 \cdot \Delta\varepsilon \\ -\frac{1}{\upsilon_0}\frac{\delta\upsilon}{\tau_p}\Delta t = \frac{\Delta\upsilon}{\upsilon_0} \approx -(6.92 \cdot 10^{-}6) \cdot \Delta T \end{aligned} \tag{3.5}$$

In this case, the measurement is essentially continuous, and the minimum detectable Δn is determined by the chirp ($\delta\upsilon/\tau_p$) and the sampling (and bandwidth) with which $E(t)$ is detected. For large Δn, the contributions of $[z_1, z_2], [z_3, z_4]$ may become relevant and introduce significant deformations to the ϕ-OTDR trace, thus limiting the validity of the approach. Experimental results indicate that to ensure correct measurements, the maximum measurable Δn should correspond to a frequency change $\Delta\upsilon$ such that $\Delta\upsilon/\delta\upsilon \approx 2-3\%$. This imposes a maximum measurable Δt which should correspond to $2-3\%$ of the pulse length (τ_p). Since the measurements can be made quite fast (there is no requirement for a frequency sweep and single-shot acquisitions are feasible) the expectable changes from trace to trace should be quite small. Measurements of large Δn variations (which typically should take long times to develop) can be also be done, in this case accumulating the measured delay values (Δt) between consecutive traces. In this way, values of Δn which are correspondent to a $\Delta\upsilon$ arbitrarily larger than $\delta\upsilon$ can be detected, as long as the errors accumulated between the consecutive measurements are kept small. This allows for fast measurements of temperature or strain, with high resolution and over long ranges.

3.2.1 Measuring technique

While traditional ϕ-OTDR measure intensity variations of all the points of the trace over time, the chirped-pulse ϕ-OTDR sensor analyses the longitudinal ϕ-OTDR trace shifts $\Lambda(t)$ which occurs along the fiber. The fiber is measured at two different times t_1, t_2, by sending two equal pulses $P_1(t,z), P_2(t,z)$ into the fiber, from which result two traces $E_1(t), E_2(t)$. Note that, as in standard ϕ-OTDR, the pattern $E(t)$ is associated with a fiber position z, by $t = 2nz/c$. The $\Lambda(t)$ occurred between the signals $E_1(t)$ and $E_2(t)$ is calculated by cross-correlating the section of $E_1(t), E_2(t)$ extracted with a moving window, defined by a certain correlation time τ_{corr}:

$$\Lambda(t) = max(E_1(t - \tau_{corr}, t + \tau_{corr}) * E_2(t - \tau_{corr}, t + \tau_{corr})), \tag{3.6}$$

Here τ_{corr} should be of the order of τ_p, and will set the spatial resolution. The temperature/strain variations which occurred in the fiber between t_1, t_2, can then be calculated using Eq. (3.5). A continuous measurement of temperature/strain along time is possible by simply integrating the successive measurements obtained for $[E_1(t), E_2(t)]$, $[E_2(t), E_3(t)] \ldots$, $[E_{n-1}(t), E_n(t)]$. However, a simple analysis will show that this is not the best way to minimize the cumulative errors of a measurement. For very small values of index change, close to the resolution of the sensor (set by the chirp and the sampling of $E(t)$), the error will increase due to quantization error. For large values of index change, the error will increase because the contributions for $E(t)$ generated from $[z_1, z_2], [z_3, z_4]$ (see Figure 3.1) are no longer negligible. Therefore, for a certain measurement setup, there will be a certain range of index change values for which the measurement error is minimum. An efficient way of minimizing the error in case of small variations is then to use the measurement of consecutive traces as a first estimate and then compare pairs of $[E_i(t), E_j(t)]$ that are more spaced in time, and for which the calculated temperature/strain variations are close to the shifts where the error is known to be minimum.

3.2.2 Experimental setup

The standard experimental setup used to measure temperature/strain changes with the chirped-pulse ϕ-OTDR is depicted in Figure 3.2. It is based on a traditional ϕ-OTDR scheme, but introducing a linear chirp in the pulse through the current control of the laser. The light source is a laser diode (LD) with a linewidth greater than 1 MHz

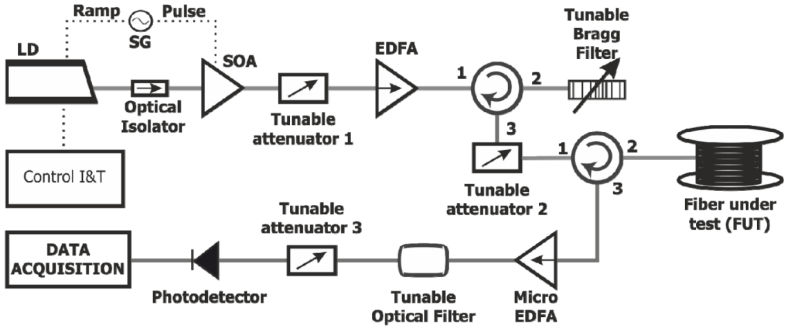

Figure 3.2. *Schematic representation of the chirped-pulse ϕ-OTDR setup (the acronyms are explained in the text). Reproduced with permission from [14]*

emitting a continuous wave in the C band (around 1550 nm). The LD is driven by a standard current and temperature controller to select the laser central wavelength. A secondary current control applies a repeated electric ramp signal in the laser driver, which introduced a linear chirp at certain times in the output laser light. This light is then gated in the time domain by a semiconductor optical amplifier (SOA), which driver is synchronized with the secondary laser current control, thus generating linearly chirped-pulses. The SOA had rise/fall times in the order of 1 ns, and is driven by a waveform signal generator (SG) to create square pulses. An optical isolator is used between the LD and the SOA to avoid laser instabilities due to reflections in the following devices. An erbium-doped fiber amplifier (EDFA) is used to amplify the pulse peak power to achieve longer sensing distances. Between the SOA and the EDFA, a variable optical attenuator is introduced to control the EDFA input power and to avoid possible nonlinearities generated in it. Note that if no nonlinearities occur in the EDFA, this attenuator (attenuator 1) is not required in the setup, since the power of the optical pulse injected into the fiber can be tuned using only attenuator 2. In order to filter the amplified spontaneous emission (ASE) added by the EDFA, a tunable fiber Bragg grating (FBG) working in reflection is inserted. Before injecting the optical pulse in the fiber under test (FUT), another tunable attenuator controls the input power to avoid nonlinearities in the fiber, mainly due to modulation instability (MI) [3]. The backscattered signal is amplified with another EDFA and filtered with a proper optical filter. Finally, the light is received by a photodetector with a large bandwidth and acquired by a high-speed digitizer with high sampling rate. Furthermore, to avoid damaging the photodetector, another tunable attenuator controls its input power. In comparison with traditional ϕ-OTDR systems, here the detection bandwidth and digitizing speed need to be much

higher, as they should cover the total bandwidth of the chirp signal used.

3.3 Stress-induced "virtual" perturbations

During my Ph.D. program, we have developed an original model for the virtual perturbation induced by the cumulative round trip time delay change, which has been then experimentally validated. The extremely high sensitivities of the chirped-pulse ϕ-OTDR increase the impact of distortions so far considered negligible, like the cumulative round trip time changes induced by perturbations acting on the fiber on all the backscattering components generated from further fiber sections. The cumulative round trip time change appears in the measurement performed with a chirped-pulse ϕ-OTDR as a small distributed, homogeneous, virtual perturbation that may potentially be corrected using a suitable model. In this section then, we start by mathematically describing the changes in the refractive index induced by a perturbation acting on the fiber and then we consider how they propagate in the theoretical measurement procedure of the chirped-pulse ϕ-OTDR to derive the model of the corresponding virtual perturbation. We then realize an experiment where the chirped-pulse ϕ-OTDR monitors two sections of a standard fiber, the first experiencing a temperature change and the second kept at rest. The theoretical results obtained from feeding the model with the temperature change applied on the first section of the fiber are validated by comparing them with the virtual perturbation measured on the second section of the fiber. The theoretical model can be exploited by an algorithm that for each stress acting on the fiber computes the corresponding virtual perturbation and corrects it, further improving the quality of the chirped-pulse ϕ-OTDR.

3.3.1 Theoretical Model

As the input pulse $P(t, z)$ of a chirped-pulse ϕ-OTDR, with central frequency υ_0, total chirp applied δ_υ and width τ_p propagates along the fiber, a small portion of its power $B(t)$ gets back-reflected due to Rayleigh backscattering. The round trip time of the light $t_{RT}(z)$ is accurately measured:

$$t_{RT}(z) = 2 \int_0^z \frac{n(\zeta)}{c} d\zeta, \tag{3.7}$$

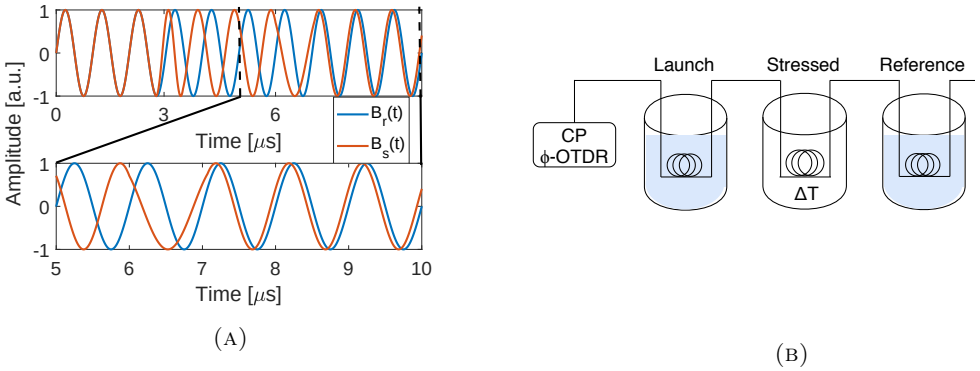

(A) (B)

Figure 3.3. *(a) Consequences of a localized stress on a simplified $B(t)$. On the bottom is shown a detail of the traces after the perturbation; (b) Schematic representation of the setup.*

where $n(z)$ is the refractive index of the fiber, and used to map each contribution of $B(t)$ to the positions of the fiber that generates it. While the fiber is kept at rest, consecutive interrogations with identical input pulses always generate the same backscattering trace $B(t)$. Differently, when a perturbation $\xi(t)$ acts on an arbitrary section of the fiber $I = [z_i, z_j]$, due to thermo-optic and/or elasto-optic effects the local refractive index $n(I)$ changes by $\Delta n(t)$. Considering then a reference backscattering trace $B_r(t)$ acquired before the perturbation and a stressed backscattering trace $B_s(t)$ acquired during the perturbation, the difference they will present is a local shift induced by $\Delta n(t)$ on $B_s(t)$ for all $t = t_{RT}(I)$. This difference is represented in the first plot of Figure 3.3a where the reference and stressed traces are perfectly overlapped until $t = 3$ μs when a shift appears. In chirped-pulse ϕ-OTDR the measurement begins by dividing both $B_r(t)$ and $B_s(t)$ into corresponding windows. For each couple of corresponding windows, that represent different positions of the fiber, a cross-correlation operation is performed and all the resulting central peaks are monitored. Due to the shift introduced by $\Delta n(t)$ in $B_s(t)$, the correlation peaks of the couples of windows corresponding to the fiber section I will shift by Δt:

$$\frac{\Delta n(t)}{n} = -\left(\frac{1}{\upsilon_0}\right)\left(\frac{\delta\upsilon}{\tau_p}\right)\Delta t. \tag{3.8}$$

By measuring the time-delay Δt and inverting eq. (3.8), it is possible to extract the value of $\Delta n(t)$ which is linearly proportional to the perturbation stressing the fiber. Due to the sensitivity of the correlation operation, the chirped-pulse ϕ-OTDR allows to sense temperature and strain changes with resolutions in the order of few millikelvin and nanostrain respectively. From eq. (3.7) it can be seen that the refractive index change in

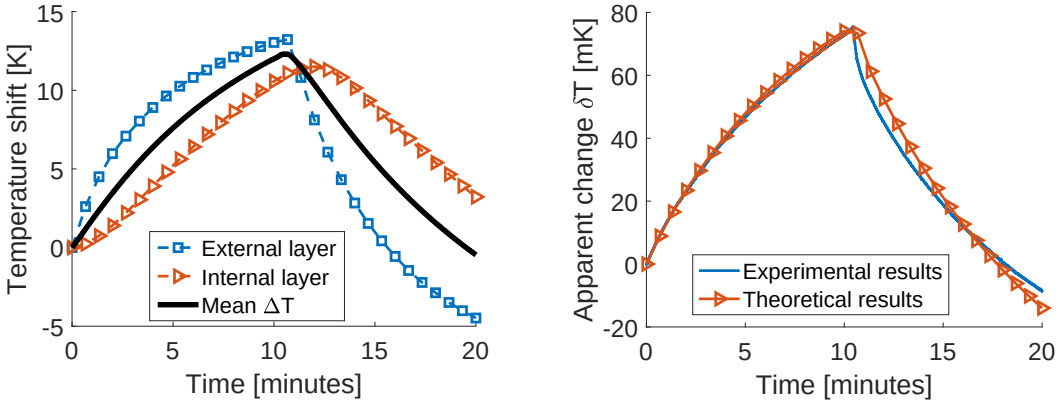

(A) (B)

Figure 3.4. *(a) Temperature changes in the stressed fiber measured in different positions (marked lines); Mean temperature change of the stressed fiber (black solid line). (b) Measured virtual temperature change in the reference fiber (blue line) compared with the expected result (marked red line).*

the section I of the fiber causes a corresponding change $\Delta t_{RT}(t)$ common to all position $z > z_j$. This distortion induces a small shift to all the corresponding components of $B_s(t)$ as visualized in detail in the second plot of Figure 3.3a, where after $t > 7\mu$s, even if no perturbation is applied, the two traces are not as perfectly overlapped as they were at the beginning. The time-delay estimation procedure described above will identify this small delay as a "virtual" perturbation, i.e. as a measured perturbation when there is no real applied stress in that fiber section. Luckily, this virtual perturbation will generally be negligible in realistic settings, and moreover can be easily corrected as we will show below.

It is convenient to develop the theoretical model describing the virtual perturbation starting from a temperature change, since it allows to reach a more general expression. It will be immediate afterwards to derive the equations of the virtual perturbation when the original perturbation is a strain. When a section of fiber L at room temperature experiences a temperature change $\Delta T(t)$ the length of the fiber changes due to thermal expansion, $\tilde{L}(t) = L + \Delta L(t)$, and the local refractive index changes due to the thermo-optic effect, $\tilde{n}(t) = n + \Delta n(t)$. The linear length variation $\Delta L(t) = \alpha \Delta T(t) L$ can be estimated through the amorphous silica linear thermal expansion coefficient $\alpha \approx 0.55 \times 10^{-6}$ $[^{\circ}C^{-1}]$ [21], while the linear refractive index change $\Delta n(t) = \zeta_T \Delta T(t) n$ is proportional to the thermo-optic coefficient of the fiber $\zeta_T = \approx 6.92 \times 10^{-6}$ [20]. The common round trip time shift $\Delta t_{RT}(t)$ for all positions after $\tilde{L}(t)$ can then be expressed

as:

$$\begin{aligned}\Delta t_{RT}(t) &= 2\left[\int_0^{\tilde{L}(t)} \frac{\tilde{n}(t)}{c} dz - \int_0^{L} \frac{n}{c} dz\right] = \\ &= 2\frac{\tilde{n}(t)\tilde{L}(t)}{c} - 2\frac{nL}{c} \approx 2\frac{n\Delta L(t)}{c} + 2\frac{\Delta n(t)L}{c}\end{aligned} \tag{3.9}$$

where the term proportional to $\Delta n(t)\Delta L(t)$ is neglected since it is many orders of magnitude lower than the others. According to eq. (3.8), the round trip time delay change $\Delta t_{RT}(t)$ appears to the instrument as caused by a distributed, homogeneous, virtual temperature change $\delta T(t)$ that modifies the refractive index of the fiber for all positions after $z > z_j$:

$$-\left(\frac{1}{\upsilon_0}\right)\left(\frac{\delta\upsilon}{\tau_p}\right)\Delta t_{RT}(t) = \frac{\Delta n_{RT}(t)}{n} = \zeta_T \delta T(t). \tag{3.10}$$

By substituting eq. (3.9) in (3.10), and solving for $\delta T(t)$ we get:

$$\begin{aligned}\delta T(t) =& K\frac{1}{\zeta_T}\frac{1}{\upsilon_0}\frac{\delta\upsilon}{\tau_p}\left[2\frac{n\Delta L(t)}{c} + 2\frac{\Delta n(t)L}{c}\right] = \\ & K\frac{1}{\zeta_T}\frac{1}{\upsilon_0}\frac{\delta\upsilon}{\tau_p}\frac{2nL}{c}\left[\alpha\Delta T(t) + \zeta_T\Delta T(t)\right].\end{aligned} \tag{3.11}$$

where the first term is related only to the thermal expansion and the second only to the thermo-optic effect. The two terms differ only for the coefficients α and ζ, thus the contribution of the thermo-optic effect on $\delta T(t)$ is about one order of magnitude higher than the one induced by thermal expansion. A constant scaling factor K has been added in the model because the actual values of the thermo-optic coefficient ζ and of the thermal expansion coefficient α of the fiber used may differ slightly from the values reported in the literature. As can be seen in eq. (3.11), the magnitude of the virtual perturbation depends linearly on the characteristics of the original perturbation applied, namely L and $\Delta T(t)$, and on the sensitivity of the instrument, defined by the chirp rate $\delta\upsilon/\tau_p$.

When strain is the original perturbation considered $\Delta\varepsilon(t)$, the contribution of elasto-optic coefficient to the round trip time change is much larger than the contribution caused by the dimensional change in the fiber, so we can consider only:

$$\delta\varepsilon(t) = K\frac{1}{\zeta_\varepsilon}\frac{1}{\upsilon_0}\frac{\delta\upsilon}{\tau_p}\frac{2\Delta n_\varepsilon(t)L}{c} \tag{3.12}$$

where $\zeta_\varepsilon = 0.78$ [20] is the elasto-optic coefficient of the fiber and $\Delta n_\varepsilon(t) = \zeta_\varepsilon\Delta\varepsilon(t)n$ is the change in the fiber refractive index caused by the strain due to the elasto-optic

effect.

3.3.2 Experimental setup

The setup used to validate the model is schematically represented in Figure 3.3b, where a standard fiber of total length $L = 18.6$ km, divided into three different sections called respectively launch, stressed and reference, is connected to a standard chirped-pulse ϕ-OTDR [14]. The laser source, centered at a wavelength of $\lambda_0 = 1.55$ μm, is modulated at a rate of $F_s = 1000$ Hz to generate chirped-pulses with a width of $\tau_p = 100$ ns and a total applied chirp of $\delta\upsilon = 1$ GHz. Such parameters, which are left untouched during the whole experiment, guarantee good SNR and sensitivity over the whole length of the fiber, while limiting resources and storage capacity consumption. The launch fiber is $L_L = 0.9$ km long and it is kept at rest to acquire an estimate of the laser phase noise, used in post-processing to correct all the measurement taken from the other fiber sections [15]. The temperature change $\Delta T(t)$ is induced on the stressed fiber, which is $L_S = 16.3$ km long, by submerging it in warm, and successively cold, water. Finally the reference fiber, which is $L_R = 1.4$ km long, is used to measure the virtual perturbation $\delta T(t)$ induced by the previous temperature change $\Delta T(t)$. As can be seen from Figure 3.3b, the launch and reference fibers are immersed into room temperature water, represented by a light blue color, to partially isolate them from external perturbations. The choice of using water to induce the temperature change $\Delta T(t)$ in the stressed fiber L_S is due to the high thermal capacity of water. A fast thermalization of the stressed fiber is important since it speeds up the experiment, reducing the impact of instrument-related noise and remaining environmental noise on the measurement. To avoid the effect of floating of the coils during the experiment, a little weight is leaned on their top, thus anchoring them to the bottom of the buckets.

3.3.3 Results

The measurement started by submerging the stressed fiber L_S in a bucket containing water at a temperature $\Delta T_H \approx 15$ K higher than the room temperature. To allow a sufficient thermalization the setup was left resting for 10 minutes, then the fiber was moved from the warm water to the cold, at a temperature $\Delta T_C \approx 8$ K lower than the room temperature, for 10 more minutes. The amount of water in the buckets was sufficient to consider the water temperatures as constants during the thermalization process. The

cool-down phase provides a further proof that the virtual perturbation in the reference fiber is indeed induced by the temperature change in the stressed fiber and not related to random environmental changes. Due to the fiber low thermal conductivity and its coiled geometry, the temperature change experienced by the different layers of the stressed fiber L_S is not uniform and the chirped-pulse ϕ-OTDR measures a position-depended perturbation $\Delta T(z,t)$. This is clearly visible in Figure 3.4a where the temperature changes measured at an outer (blue line, square marker) and inner (red line, triangular marker) layer, are represented. As can be seen, during both thermal phases the temperature of the layer closer to the water shows an immediate exponential-like response, which agrees with the Newtonian laws of heating and cooling, while the change in the inner one is delayed and shows an almost linear change corresponding to the same exponential behavior but with a much larger time constant. Since both the thermo-optic effect and thermal expansions are linear phenomena with respect to the temperature changes, it is convenient to average the position-dependent perturbations $\Delta T(z,t)$ into an equivalent uniform temperature change $\Delta T(t)$, reported in Figure 3.4a as a black solid line.
The apparent perturbations $\delta T(z,t)$ induced by the temperature change in the stressed fiber are measured along the whole reference fiber. Due to instrument-related noise and remaining environmental stresses, the terms $\delta T(z,t)$ along the reference fiber represent position-dependent replicas of the same virtual perturbation with an added, arbitrary, temporal evolution, which can be averaged to obtain the desired $\delta T(t)$. The results are shown in Figure 3.4b where the experimental virtual perturbation (blue solid line) is compared with the theoretical one (red marked line). The theoretical curve was computed using the model of eq. (3.11) with $K = 0.78$, $\Delta L = L_S$ and the equivalent uniform temperature change measured in the stressed fiber $\Delta T(t)$ as parameters. As can be seen, the curves show a great agreement during the whole experiment, even if a slight mismatch is visible during the cool down. This mismatch can be explained by a number of reasons: position-dependent ambient noise, strain induced in the fiber during the bucket exchange phase, imperfect reference updating [14], etc. These effects can be smoothed down by the averaging operation of the terms $\delta T(z,t)$ along the position axis, but cannot be completely removed. The increasing difference in time between the traces is better visualized by computing the standard deviation of the $\delta T(z,t)$ terms along the position axis for each time instant. The result is shown in Figure 3.5, where the instant standard variation is added to the averaged measurement. As can be noticed, the

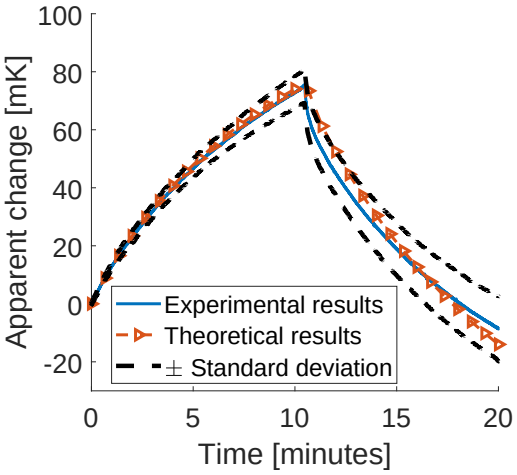

Figure 3.5. *Experimental data with standard deviation bounds.*

standard deviation is monotonically growing in time, with the cumulation of all these sources of drift.

3.3.4 Conclusion

A mathematical model of the stress-induced virtual perturbation measured by a chirped-pulse ϕ-OTDR has been proposed and validated. The parameters of the model, which depends on the original stress and on the measurement procedure of the instrument, have been highlighted and discussed. We have then performed an experiment where the temperature of a known section of fiber was changed, and the consequent virtual perturbation has been monitored. The theoretical results were compared with the experimental ones showing a convincing agreement. The model can be used to estimate and progressively correct the errors introduced by perturbations acting on the fiber, thus improving the quality of the measurement performed with chirped-pulse ϕ-OTDR, especially when weak perturbations are being monitored. Nevertheless, it should be noted that the effect of these "induced virtual perturbations" should be negligible in the vast majority of practical cases, since the values of stress required to observe these "virtual" perturbations are quite high in comparison with the type of stimuli that can be induced in regular field installations.

3.4 High-resolution chirped-pulse ϕ-OTDR

Chirped-pulse phase-sensitive optical time-domain reflectometry (chirped-pulse ϕ-OTDR) allows the interrogation of tens of kilometers of optical fiber with high sensitivities of

millikelvin and nanostrain. With respect to standard ϕ-OTDR, its shows increased robustness to coherent fading and allows a linear monitoring of the perturbations acting on the fiber. Its spatial resolution however is still in the order of tens of meters, constrained by the input pulse width that must be kept large enough to ensure proper processing and sufficient signal-to-noise ratio (SNR).

During my Ph.D. program we have then developed a method based on sub-bands processing to improve the spatial resolution of the chirped-pulse ϕ-OTDR scheme without reducing the width of the optical pulse. An optical carrier at a proper frequency is added to the interrogating pulse, allowing the extraction of the fiber response to the chirped-pulse from the received signal. By using proper digital filters, the spectrum of the fiber response is divided into multiple sub-bands, eventually overlapped, being conceptually analogous to the spectra of the fiber response generated by multiple slightly delayed short pulses. The analysis of any one of these sub-bands guarantees then results characterized by high spatial resolution but significantly reduced SNR. By performing a proper averaging operation during the analysis of the multiple sub-bands, a strong mitigation of the SNR reduction can be achieved. Starting from the description of the standard chirped-pulse ϕ-OTDR setup, we derive a mathematical model of the backscattering signal generated by the proposed interrogation signal (i.e. containing a linearly chirped-pulse with an added optical carrier). We then accurately describe the sub-bands processing analyzing in detail the averaging operation used to mitigate the SNR reduction. In addition, we propose an experimental setup to demonstrate the spatial resolution enhancement guaranteed by the sub-bands processing and we compare the results with those obtained from a standard chirped-pulse ϕ-OTDR. By accepting a modest reduction of the measurement SNR, which however does not affect the quality of the results, experimental results demonstrate that a 15-fold improvement of the spatial resolution can be achieved. Finally, we discuss the advantages of using overlapped sub-bands to increase the number of terms in the averaging operation and we optimize the overlap factor.

3.4.1 Theoretical model

In a chirped-pulse ϕ-OTDR [14] the input pulse $P_{std}(t, z)$ can be defined as:

$$P_{std}(t, z) = E_0 rect\left[\frac{(t - \beta_1(z)}{\tau_p}\right] P_{cp}(t, z), \tag{3.13}$$

where E_0 is the pulse field amplitude, $\beta_1(z) = \int_0^z n_g(z)dz/c$ is the propagation delay, τ_p is the pulse width and:

$$P_{cp}(t,z) = e^{j2\pi(\upsilon_0 + \frac{\delta\upsilon}{\tau_p}[t-\beta_1(z)])(t-\beta_1(z))}, \tag{3.14}$$

is the linearly chirped term with total applied chirp $\delta\upsilon$. As the pulse propagates along the fiber, it generates a Rayleigh backscattering signal that represents the fiber response to the chirped-pulse. This response can be described as the convolution of the input pulse with the fiber Rayleigh backscattering profile function $r(z)$:

$$E_{std}(t) = P_{std}(t,z) * r(z). \tag{3.15}$$

Upon detection $E_{std}(t)$ is converted from the optical to the electrical domain:

$$I_{std}(t) = E_{std}(t)E^*_{std}(t) \tag{3.16}$$

where, as for any OTDR setup, each time instant t can be associated with a fiber position z by $t = 2nz/c$. When a perturbation acts on a position z_0 of the fiber, it induces a change Δn in the local refractive index [22]. When a chirped-pulse ϕ-OTDR is used to interrogate the fiber, in correspondence to the position z_0, Δn generates a linearly proportional longitudinal shift Λ of the local pattern of $I_{std}(t)$:

$$\frac{\Delta n}{n} = -\left(\frac{1}{\upsilon_0}\right)\left(\frac{\delta\upsilon}{\tau_p}\right)\Lambda, \tag{3.17}$$

which can be immediately translated to the temperature change or strain that generated it through the relations in (3.5) [20]. By monitoring the longitudinal shifts in the pattern of $I_{std}(t)$ along the whole fiber, the perturbations affecting the fiber can be completely characterized. The measurement procedure of a standard chirped-pulse ϕ-OTDR starts by interrogating the fiber with two identical pulses. Those pulses generate two traces, called respectively reference $I_{std,r}(t)$ and measurement $I_{std,m}(t)$, obtained with a time difference δt. The shifts $\Lambda(t)$ over the temporal trace are calculated by a cross-correlation calculated over a moving window along $I_{std,r}(t)$ and $I_{std,m}(t)$, defined by a correlation time $\tau_c = \tau_p$, which define the spatial resolution:

$$I_{xcorr}(t) = I_{std,r}(t-\tau_c, t+\tau_c) * I_{std,m}(t-\tau_c, t+\tau_c), \tag{3.18}$$

$$\Lambda(t) = max(I_{xcorr}(t)). \tag{3.19}$$

Then, using equations (3.5), $\Lambda(t)$ are converted to the corresponding temperature or strain changes. Any improvement in the spatial resolution of the chirped-pulse ϕ-OTDR is hindered by the direct detection in 3.16, which scrambles the useful information contained in the fiber response to the chirped-pulse $E_{std}(t)$. The easiest way to solve such an issue and extract $E_{std}(t)$ consists in implementing a coherent receiver, but the necessity of a highly coherent laser, as well as the increased phase noise induced by the presence of a local oscillator makes this alternative unappealing. To measure $E_{std}(t)$, we modify the interrogating signal of the chirped-pulse ϕ-OTDR in 3.13 by adding to the input pulse a separate optical carrier, so that:

$$P(t,z) = E_0 rect\left[\frac{(t-\beta_1(z)}{\tau_p}\right](P_{oc}(t,z) + P_{cp}(t,z)), \tag{3.20}$$

where:

$$\begin{aligned} P_{oc}(t,z) &= e^{j2\pi(\upsilon_0-\tilde{\upsilon_0})(t-\beta_1(z))}, \\ P_{cp}(t,z) &= e^{j2\pi(\upsilon_0+\frac{\delta\upsilon}{\tau_p}[t-\beta_1(z)])(t-\beta_1(z))}, \end{aligned} \tag{3.21}$$

are respectively the optical carrier, centered at the optical frequency $\upsilon_0 - \tilde{\upsilon_0}$, and of the chirped-pulse in 3.13. An example of the $P(t,z)$ spectrum is shown in Figure 3.6a(a). Due to the linearity of the convolution, the propagation of the modified $P(t,z)$ along the fiber can be modeled as the generation of two different backscattering components:

$$E(t) = P(t,z) * r(z) = E_{oc}(t) + E_{cp}(t), \tag{3.22}$$

and upon reception the electrical signal becomes:

$$I(t) = E(t)E^*(t) = I_{bb}(t) + I_{pb}(t), \tag{3.23}$$

where $I_{bb}(t) = |E_{oc}(t)|^2 + |E_{cp}(t)|^2$ and, by calling $\mathcal{R}(\cdot)$ the real part operator, $I_{pb}(t) = 2\mathcal{R}(E_{oc}(t)E^*_{cp}(t))$. As can be seen in Figure 3.6a(b), the spectrum $I_{bb}(f) = \mathcal{F}(I_{bb}(t))$ is a baseband, triangularly shaped term and, if we neglect the contribution of the carrier, it corresponds to the spectrum of the signal received by the standard chirped-pulse ϕ-OTDR in 3.16. The spectrum $I_{pb}(f) = \mathcal{F}(I_{pb}(t))$ is passband instead and, considering the optical carrier as a pure spectral line, it represents the desired fiber response to the chirped-pulse $E_{cp}(t)$. Given that the spectral width of $I_{bb}(f)$ is twice the spectral width

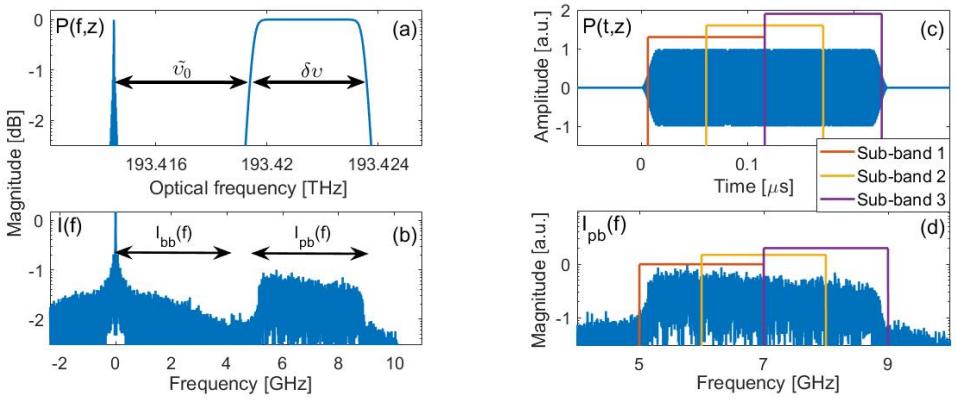

(A) (B)

Figure 3.6. *(a) Optical spectrum of the input pulse $P(t,z)$, with $\delta\upsilon = 4$ GHz and $\tilde{\delta\upsilon} = 5$ GHz. (b) Electrical spectrum of the received backscattering signal $I(t)$ with highlighted baseband and passband terms. (c) Input optical pulse $P(t,z)$ with three overlapping sub-windows ($N = 2$, $F = 2$). (d) Pass-band term $I_{pb}(f)$ divided into three sub-bands ($N = 2$, $F = 2$). Each sub-band corresponds to the Rayleigh spectral response associated to one of the sub-windows in (c).*

of $P_{cp}(t,z)$, the frequency shift in 3.20 must be at least $\tilde{\upsilon_0} \geq 2\delta\upsilon$ to avoid overlaps with the spectrum of $I_{pb}(f)$. In the following analysis we will focus on $I_{pb}(f)$ which, assuming that the condition for the frequency shift $\tilde{\upsilon_0}$ is verified, can be extracted from the received signal $I(f)$ by proper digital filtering. Due to the linear chirp applied to $P_{cp}(t,z)$, any sub-window of the input pulse in 3.19 generates a specific sub-band in $I_{pb}(f)$, as can be seen in Figure 3.6b(c) and 3.6b(d). The spectrum of each sub-band corresponds to the spectrum generated when interrogating the fiber with a single short pulse, thus its analysis guarantees a sharp spatial resolution (i.e. improved with respect to the use of the entire chirp pulse), but at the cost of a reduced SNR. Such a reduction can be mitigated exploiting the redundant information contained in the sub-bands: since they are extracted from the same pulse they correspond to almost simultaneous measurements, thus they contain information about the same perturbations. In addition, the receiver noise affecting the different high-resolution ϕ-OTDR section is uncorrelated, and therefore a suitable averaging operation, which takes into account the small temporal shifts introduced during the sub-bands' extraction, guarantees a strong mitigation of the SNR reduction while allowing high spatial resolution measurements. The algorithm starts like the conventional chirped-pulse ϕ-OTDR, by acquiring the reference $I_r(t)$ and measurement $I_m(t)$ traces at time instants separated by δt. Then, the corresponding passband components $I_{pb,r}(f)$ and $I_{pb,m}(f)$ are extracted using a digital bandpass filter of width $\delta\upsilon$. As mentioned above, the spatial resolution of an OTDR setup is proportional to

the length of the pulse used to investigate the fiber. Therefore, to improve the spatial resolution by a factor N, it is necessary to split $I_{pb,r}(f)$ and $I_{pb,m}(f)$ into N independent sub-bands $I^n_{pb,r}(f)$, $I^n_{pb,m}(f)$, $n = 1, \dots N$ of width $\Delta W = \delta\upsilon/N$ and to adapt the correlation time accordingly $\tilde{\tau_c} = \tau_p/N$. Each pair (reference and measurement) of spectral sub-bands is the converted back to time-domain after synchronizing them to account for the time shift induced during the filtering process:

$$\begin{aligned} I^n_{pb,r}(t) &= \mathcal{F}^{-1}\{e^{-j2\pi f(n-1)\tilde{\tau_c}} I^n_{pb,r}(f)\}, \\ I^n_{pb,m}(t) &= \mathcal{F}^{-1}\{e^{-j2\pi f(n-1)\tilde{\tau_c}} I^n_{pb,m}(f)\}. \end{aligned} \tag{3.24}$$

The cross-correlation traces in 3.18 are computed for each corresponding pair of $I^n_{pb,r}(t)$ and $I^n_{pb,m}(t)$, using the reduced correlation time $\tilde{\tau_c}$:

$$I^n_{xcorr}(t) = I^n_{pb,r}(t - \tilde{\tau_c}, t + \tilde{\tau_c}) * I^n_{pb,m}(t - \tilde{\tau_c}, t + \tilde{\tau_c}) \tag{3.25}$$

and then averaged into a single one:

$$I_{xcorr}(t) = \frac{1}{N} \sum_{n=1}^{N} I^n_{xcorr}(t). \tag{3.26}$$

The shifts $\Lambda(t)$ along the fiber are then extracted using the operation in 3.19 and converted to the corresponding temperature or strain change through the equations in 3.5. The averaging of the cross-correlation traces $I^n_{xcorr}(t)$ in 3.26 is the key operation of thus method for increasing the spatial resolution of the chirped-pulse ϕ-OTDR and mitigate the critical SNR reduction induced when dividing $I_pb(f)$ into sub-bands. The extraction of $\Lambda(t)$ in 3.19 works properly only when the central correlation peak is the highest, but if two traces with low SNR are used in 3.25, noise-induced side peaks at random lags may exhibits higher magnitudes. In such cases, $\Lambda(t)$ extracted from 3.19 is random and does not represent the perturbation affecting the fiber. Even after averaging all the shifts extracted from the N different correlation traces, the results will be comparable to the ones obtained using directly a single short pulse, thus generally with an SNR being too low to be useful. However, since the noise-induced side peaks in 3.13 appears at different lags for different cross-correlation traces, by averaging $I^n_{xcorr}(t)$ their amplitude can be significantly dampened, allowing a correct extraction of the central correlation peak shift. The shift of the central correlation peak is affected by the low SNR of the $I_(pb, r)^n(t)$ and $I_(pb, m)^n(t)$ traces as well, so the $\Lambda(t)$ extracted from 3.19 will exhibit

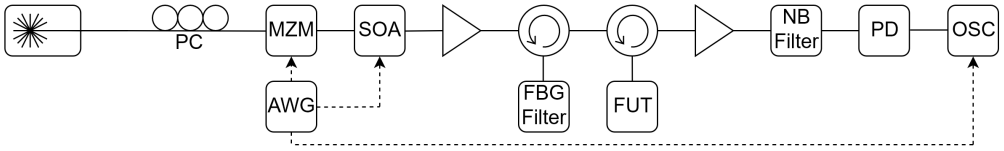

Figure 3.7. *Schematic representation of the experimental setup (the acronyms are explained in the text).*

a residual noise, even after the averaging operation in 3.26. Increasing the number of averaged terms by partially overlap consecutive sub-bands allows however for a further improvement. Defining the shift between the central frequency of consecutive sub-bands as $\delta W = \Delta W/F$, with F being an integer number called overlap factor, the abovementioned N independent sub-bands can be extracted from $I_p b(f)$ by setting $F = 1$, while a larger number $K = F(N-1)+1 > N$ of partially overlapped sub-bands can be extracted setting $F > 1$. The noise affecting progressively more overlapped sub-bands exhibits a growing degree of correlation, so the efficiency of the averaging operation will decrease for high values of F. Since the time required to perform the analysis is proportional to the number of generated sub-bands K, increasing F too much will only result in useless waste of computational time. In section V, the optimal choice for the overlap factor, which maximizes the SNR mitigation provided by 3.26, but keeps the analysis efficient, will be identified as a function of the algorithm parameters.

3.4.2 Experimental setup

Figure 3.7 shows the setup used to experimentally demonstrate the performance of the method based on sub-bands processing. A coherent, continuous-wave laser at $\lambda_0 = 1550$ nm is connected to a Mach-Zehnder modulator (MZM) after passing a polarization controller (PC), to avoid polarization dependent losses in the modulator. The MZM modulates the amplitude of the laser output according to a driving signal generated by the arbitrary waveform generator (AWG) which consists of rectangular chirped-pulses sent at rate $R \approx 1.67$ kHz with temporal width $\tau_p = 200$ ns, total applied chirp $\delta\upsilon = 4$ GHz, and frequency shift $\tilde{\upsilon_0} = 5$ GHz. As will be demonstrated in Section V, the optimum overlap factor for such parameters is $F = 7$. A semiconductor optical amplifier (SOA) with rise time of $\approx$1 ns and driven by a different but synchronized channel of the AWG is used to increase the extinction ratio of the pulses. The optical spectrum of the modulated signal at the output of the SOA exhibits a central carrier with two symmetrical flat sidebands of same width $\delta\upsilon$, but opposite chirp rate, representing the

spectrum of the linearly chirped-pulses. By adjusting the MZM bias voltage, the amplitude of the carrier is reduced to match the peak amplitude of the sidebands, thus avoiding photodetector saturation due to strong DC components. To compensate the losses introduced mostly by the MZM, an erbium-doped fiber amplifier (EDFA) is inserted, so that the pulse power is boosted as much as possible, but avoiding the onset of nonlinear effects like modulation instability. The amplified spontaneous emission noise (ASE) introduced by the EDFA is removed by a standard reflective fiber Bragg grating filter (FBG), centered at λ_0, before launching the pulses into the fiber under test (FUT). The backscattering signal $E(t)$ generated by the FUT, which spectrum still exhibits a double sideband modulation, is amplified by a second EDFA at the receiver front-end, followed by a narrow band (NB) optical filter. The bandwidth of the NB filter is tuned to suppress one of the chirped sidebands as well as the ASE. Note that while the choice of which sideband must be suppressed is irrelevant for the performance of the method, their chirp rate shows opposite sign, influencing the sign of the results if not properly corrected. Finally, a 12 GHz photodetector (PD) followed by an oscilloscope (OSC) with an input bandwidth of 13 GHz and a sampling rate of 40 GSa/s, triggered by the AWG, is used to collect the received traces $I(t)$. Such traces are then digitally lowpass filtered at $f_{LPF} = 9.5$ GHz to remove high-frequency noise. The FUT consists of a standard singlemode optical fiber of length $L_{FUT} \approx 100$ m bounded to an aluminum alloy wire accessible in various points. The FUT can be heated up through Joule effect by applying a voltage V_{FUT} between any two accessible points. The fiber-wire bundle is covered by a thick polymeric coating that allows for partial isolation from external perturbations, thus ideally securing a uniform and efficient temperature change.

3.4.3 Results

To experimentally demonstrate the spatial resolution improvement provided by subbands processing, a segment of the FUT of length $L_p = 2.5$ m, centered around position $z = 33.5$ m, has been heated up uniformly by applying a constant voltage $V_{FUT} = 1.2$ V to the metallic wire. The oscilloscope is set to acquire 2^{14} traces at a rate R, monitoring the perturbation acting on the fiber for about 9 seconds. To smooth down fast environmental changes that could reduce the quality of the correlation operation in 3.25, the traces collected every three consecutive acquisitions have been averaged, limiting the effective measurement rate to $R_{eff} \approx 550$ Hz. To secure a visible temperature change,

two arbitrary traces separated by $\delta t = 0.24$ s, have been selected as $I_r(t)$ and $I_m(t)$ and the corresponding passband terms $I_{pb,r}(f)$ and $I_{pb,m}(f)$ have been extracted with a digital rectangular passband filter of width δv.

The discussed method has then been executed by fixing the overlap factor to the optimal value of $F = 7$, for different values of $N = [1, 2, 4, 8, 10, 13, 15]$, corresponding respectively to spatial resolutions of $SR = [20, 10, 5, 2.5, 2, 1.5, 1.3]$ m and a total number of sub-bands $K = [1, 8, 22, 50, 64, 81, 94]$. Results are shown in Figure 3.8a, where we can see that, for the values of $N < 8$, corresponding to spatial resolutions larger than $L_p = 2.5$ m, the longitudinal shift Λ of the local pattern of the backscattering trace $I^n_{pb,m}(t)$ occupies at most a fraction of the correlation window $\tilde{\tau_c}$. Consequently, the correlation operation in 3.25 is not be strongly affected by Λ, and the measured results show a hot-spot with distorted magnitude, spread over a section of the fiber proportional to the spatial resolution. This effect can be seen in Figure 3.8a where the amplitudes and the full-width at half-maximum of the temperature changes, which represents the spatial extent of the hot spot between the two temperature changes equal to half of the maximum value, measured for values of $N \leq 4$ are visibly different from the applied temperature change (represented in the figure by the black dashed line). For values of $N \geq 8$ the size of the correlation window $\tilde{\tau_c}$ is equal or shorter than the perturbed segment L_p, so the correlation operation correctly estimate the temperature-induced shifts and the results of the discussed method agree with the real temperature change applied. Observing the lines corresponding to $N \geq 8$ in Figure 3.8a, the effects of the increased spatial resolution can be verified by the sharper transitions in the temperature profile. Finally, Figure 3.8a also shows a minimum effect on the quality of the measurements, although the better spatial resolution demonstrated. This result confirms that the averaging operation between the correlation traces $I^n_{xcorr}(t)$ computed from overlapped sub-bands is an effective solution for compensating the SNR reduction expected due to the spatial resolution improvement. It must be pointed out that the change in the interrogating pulse indeed does not influence the high performance of the standard chirped-pulse ϕ-OTDR setup like the robustness to signal fading, the high sensitivity or the possibility of performing dynamic measurements. This can be verified by changing the temperature of the fiber section around the position $z = 33.5$ m during the 9 s. The results are shown in Figure 3.8b(b) and 3.8b(c) where a linearly increasing temperature change can be observed without distortion. For this experiment the parameters were set to $N = 15$ and $F = 7$, thus guaranteeing a spatial resolution of $SR = 1.3$ m. As can

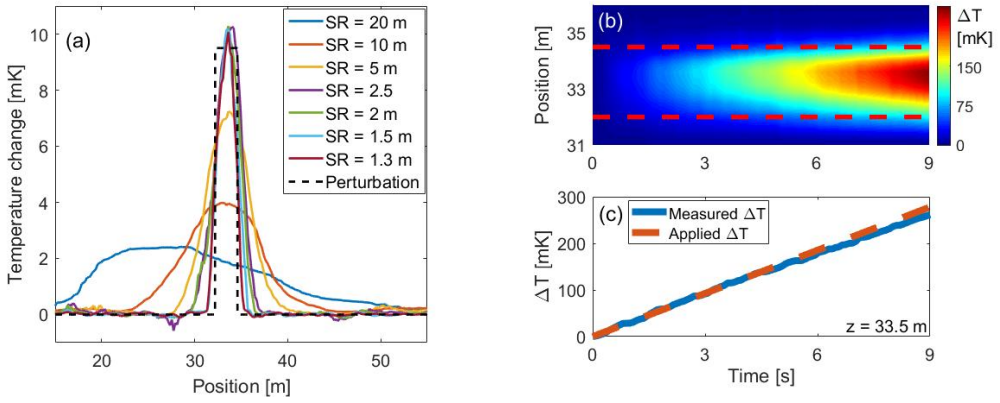

(A) (B)

Figure 3.8. *Temperature changes measured for different spatial resolutions with fixed overlap factor $F = 7$. The black dashed line represents the applied temperature change. (b) Temperature change measured over a temporal interval of 9 seconds (using $N = 10$ and $F = 7$). The red dashed lines identify the heated fiber section of length L_p. (c) Comparison between the measured temperature change magnitude with respect to the applied one.*

be seen, the magnitude of the measured temperature change closely follows the applied perturbation one and its position is correctly identified, spread over a fiber section of length L_p.

To compare the advantages in monitoring long perturbations obtained by the sub-bands processing with respect to the original standard chirped-pulse ϕ-OTDR, a temperature change has been induced on a segment of the fiber of length $L_p = 25$ m, centered around position $z = 37$ m. As before, the temperature change was generated through Joule heating of the metallic wire bounded to the fiber but, given the increased length, to guarantee a visible perturbation the voltage applied was raised to $V_{FUT} = 8$ V. The traces have been first collected using the standard chirped-pulse ϕ-OTDR setup, sending pulses of width $\tau_p = 200$ ns providing a spatial resolution of $SR = 20$ m.

After the acquisition, the power supply was turned off to let the fiber cools down to room temperature before turning it on again with the same V_{FUT} to acquire the traces with the high-resolution setup. The results of the two analysis are shown in Figure 3.9a where the blue line represent the temperature profile extracted with the original setup, while the red one represent the high-resolution curve obtained through sub-bands processing. The traces used as reference and measurement were separated by $\delta t = 0.24$ s for both analysis and the parameters for the sub-bands processing were set to $N = 15$, $F = 7$. As can be seen, the results obtained from both setups correctly identify the position and the magnitude of the perturbation but, as expected, the transient of the trace

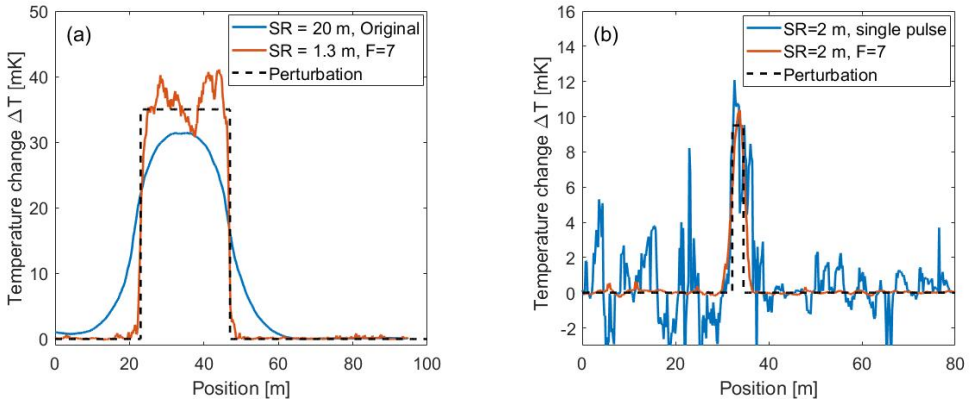

(A) (B)

Figure 3.9. *(a) Temperature change over 25 meters measured with the original chirped-pulse ϕ-OTDR method ($SR = 20$ m) (blue line) and with the high resolution method ($SR = 2$ m,$F = 7$) (red line). (b) Comparison between the temperature profile measured with the original method and pulses of $\tau_p = 20$ ns, providing a spatial resolution $SR = 2$ m (blue line) and the temperature profile measured with the high resolution method using pulses of $\tau_p = 200$ ns and setting $N = 10$, thus $SR = 2$ m and $F = 7$.*

computed from the original chirped-pulse ϕ-OTDR is much longer than the transient of the trace extracted applying sub-bands processing. Moreover, the increased spatial resolution allows a more accurate evaluation of the perturbation affecting the fiber: the trace obtained by applying sub-bands processing highlights a non-uniform temperature change along the perturbed section of the fiber that is hidden in the traced obtained with the standard setup, due to the low spatial resolution. The high-resolution trace exhibits once again a worse SNR than the trace measured with the original setup, as can be easily seen along the whole trace in 3.9a. Nevertheless, such an SNR reduction does not influence the quality of the measurement. A final demonstration of the performance improvement provided by the method has been performed by comparing the measurement of a temperature change induced over a section of the fiber of length $L_p = 2.5$ m, extracted initially with the original chirped-pulse ϕ-OTDR sending pulses of width $\tau_p = 20$ ns corresponding to a spatial resolution of $SR = 2$ m, and then with the high-resolution setup using pulses of $\tau_p = 200$ ns, $N = 10$ guaranteeing the same spatial resolution of $SR = 2$ m, and overlap factor $F = 7$. As can be seen in Figure 3.9b, the temperature profile measured with sub-bands processing accurately exhibits a much higher measurement quality compared to the temperature profile change obtained with the standard setup. Indeed, while the measured temperature change matches the applied perturbation in both cases, the measurement with the standard setup shows high spikes, which are comparable to the magnitude of the applied perturbation. This

result demonstrates the significant measurement improvement provided by the setup and sub-band processing discussed so far.

3.4.4 Overlap factor optimization

The theoretical section introduced the idea of extracting overlapped sub-bands from the spectrum $I_{pb}(f)$ to increase the number of traces averaged in 3.26 and improve the mitigation of the SNR reduction introduced by the sub-bands processing. To extract overlapped sub-bands, the central frequency of the passband filter is shifted of steps of $\delta W = \Delta W/F$, where F is an integer number called overlap factor. When $F = 1$, the usual N independent sub-bands are extracted, while when $F > 1$, $K = F(N-1)+1 > N$ overlapped sub-bands are generated. Assuming the noise affecting $I_{pb}(f)$ to be white, the N independent sub-bands extracted will have uncorrelated noise. This can secure the maximum efficiency in the averaging process described in 3.26, thus reducing the error in the estimation of the shifts $\Lambda(t)$ of the central correlation peak of a factor proportional to $\sqrt{N}$. For increasing values of F, the noise affecting overlapped sub-bands becomes progressively more correlated and the efficiency of the averaging process is reduced. Nevertheless, the number of terms available for averaging increases by a factor proportional to F, over-compensating the reduced efficiency and providing a net gain in the mitigation of the SNR reduction. For high values of F, the gain saturates, thus the generation of many sub-bands K unnecessarily increases the computational time of the analysis. The total chirp $\delta\upsilon$ applied to the pulse affects the optimum overlap factor, since for a given F a larger chirp implies a larger bandwidth of the K sub-bands, thus a lower noise correlation. It is thus necessary to perform a overlap factor optimization every time the pulse parameters are changed. To identify the optimum value of F, a definition of the trace SNR must be introduced:

$$SNR_F = \frac{max(\Lambda_F(t))}{std(\Lambda_F(t_u n))} \tag{3.27}$$

where $\Lambda_F(t)$ are the shifts measured when setting a particular F, and $t_u n$ represents the longest unperturbed window of the trace. Thanks to the linearity of the equations in 3.5, the SNR analysis as a function of F is performed by heating up a segment of the FUT of length $L_p = 2.5$ m, centered around position $z = 33.5$ m and interrogating the fiber with pulses of $\tau_p = 200$ ns, total applied chirp $\delta\upsilon = 4$ GHz, and frequency shift $\tilde{\upsilon_0} \approx 5$ GHz. The maximum temperature change measured is then compared with the

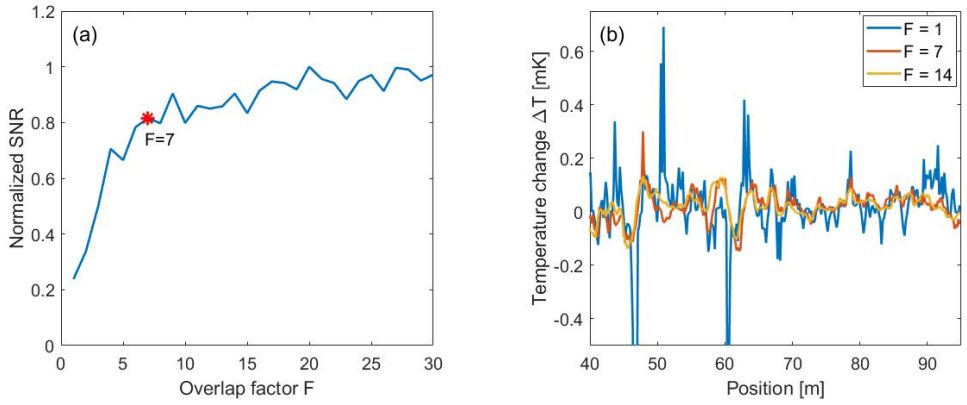

(A) (B)

Figure 3.10. *(a) Normalized SNR for different values of F. Highlighted is the optimal trade-off value of F; (b) Comparison between the unperturbed sections of the fiber measured for different values of F*

standard deviation computed over the positions $z > 35$ m, remembering that $t = 2nz/c$, where the fiber remains unperturbed. The overlap factor F has been varied from 1 to 30 and the resulting SNR_F are shown in Figure 3.10a, after normalizing them with respect to the highest one. As can be seen in the figure, the SNR shows an increasing behavior for increasing values of F, but after $F = 7$ the improvement becomes insignificant. An overlap factor greater than $F = 7$ does not provide then a significant advantage, so such a value can be taken as the optimum overlap factor for the new configuration. The effects of the SNR saturation for high values of F is shown in Figure 3.10b where a comparison between the trace measured without overlapping sub-bands (i.e. with $F = 1$) and with overlapped sub-bands of factor $F = 7$ and $F = 14$ is represented. As can be seen, there is a huge reduction of the noise between the case with $F = 1$ and the cases with $F > 1$, but there are almost no visible differences between the traces measured for $F = 7$ and $F = 14$. Considering that the number of sub-bands analyzed for $F = 14$ is twice as large than for $F = 7$, the increased computational time makes the small obtained improvement unappealing.

3.4.5 Conclusions

A method to improve the spatial resolution of chirped-pulse ϕ-OTDR systems based on sub-bands processing have been described and a 15-fold improvement have been experimental demonstrated. The division of the fiber response to the chirped-pulse into sub-bands, and the consequent processing, allows to convert a measurement performed with a long pulse, characterized by a bad spatial resolution, in a measurement with high

spatial resolution at the cost of a slightly reduced SNR. The total chirp in each sub-band however is reduced with respect to the original pulse, proportionally limiting the maximum measurable temperature or strain change. This issue can be readily avoided by comparing traces separated by a small temporal windows and keeping trace of the previous changes. To avoid distortions in the linear chirp generated by the Mach-Zehnder modulator, the magnitude of the chirped side-bands of the input pulse was reduced, limiting the maximum measurement range. By implementing more precise techniques to realize the chirped side-bands or by finding a different way to add the optical carrier to the input pulse, without increasing the phase noise, such limitation can be relaxed.

Bibliography

[1] M. K. Barnoski and S. M. Jensen, "Fiber waveguides: a novel technique for investigating attenuation characteristics," Appl. Opt., **15**(9), 2112 (1976).

[2] L. Palmieri and L. Schenato, "Distributed Optical Fiber Sensing Based on Rayleigh Scattering," The Open Optics Journal **7**(1), 104-127 (2013).

[3] H. F. Martins, S. Martin-Lopez, P. Corredera, P. Salgado, O. Frazão, and M. González-Herráez, "Modulation instability-induced fading in phase-sensitive optical time-domain reflectometry," Opt. Lett., **38**(6), 872–874 (2013).

[4] P. Healey, "Fading in heterodyne OTDR," Electron. Lett., **20**(1), 30–32 (1984).

[5] K. Shimizu, T. Horiguchi, and Y. Koyamada, "Characteristics and reduction of coherent fading noise in Rayleigh backscattering measurement for optical fibers and components," J. Light. Technol. **10**(7), 982–987 (1992).

[6] E. Bodtker, B. Tromborg, J. Mark, and C. J. Nielsen, "Heterodyne OTDR at 0.82 μm," Electron. Lett. 19(10), 361–362 (1983).

[7] J. C. Juarez, E. W. Maier, K. N. Choi, and H. F. Taylor, "Distributed fiber-optic intrusion sensor system," J. Light. Technol., **23**(6), 2081–2087 (2005).

[8] X. Bao and L. Chen, "Recent Progress in Distributed Fiber Optic Sensors," Sensors, **12**(7), 8601–8639 (2012).

[9] Z. He, Q. Liu, X. Fan, D. Chen, S. Wang, G. Yang, "Fiber-optic distributed acoustic sensors (DAS) and applications in railway perimeter security," in Proc. SPIE 10821, 1082102 (2018);

[10] F. Peng, H. Wu, X.-H. Jia, Y.-J. Rao, Z.-N. Wang, and Z.-P. Peng, "Ultra-long high-sensitivity ϕ-OTDR for high spatial resolution intrusion detection of pipelines," Opt. Express, **22**(11), 13804–13810 (2014).

[11] T. Zhu, Q. He, X. Xiao, and X. Bao, "Modulated pulses based distributed vibration sensing with high frequency response and spatial resolution," Opt. Express, **21**(3), 2953–2963 (2013).

[12] Y. Muanenda, C. J. Oton, S. Faralli, and F. D. Pasquale, "A Cost-Effective Distributed Acoustic Sensor Using a Commercial Off-the-Shelf DFB Laser and Direct Detection ϕ-OTDR," IEEE Photon. J., **8**(1), 1–10 (2016).

[13] M. A. Soto, J. A. Ramírez, and L. Thévenaz, "Intensifying the response of distributed optical fibre sensors using 2D and 3D image restoration," Nat. Commun., **7**, 10870 (2016).

[14] J. Pastor-Graells, H. F. Martins, A. Garcia-Ruiz, S. Martin-Lopez, and M. Gonzalez-Herraez, "Single-shot distributed temperature and strain tracking using direct detection phase-sensitive OTDR with chirped-pulses," Opt. Express, **24**(12), 13121 (2016).

[15] M. R. Fernández-Ruiz, J. Pastor-Graells, H. F. Martins, A. Garcia-Ruiz, S. Martin-Lopez, and M. Gonzalez-Herraez, "Laser Phase-Noise Cancellation in Chirped-Pulse Distributed Acoustic Sensors," J. Light. Technol., **36**(4), 979–985 (2018).

[16] J. C. Juarez and H. F. Taylor, "Field test of a distributed fiber-optic intrusion sensor system for long perimeters," Appl. Opt., **46**(11), 1968-1971 (2007).

[17] K. Miah and D. K. Potter, "A Review of Hybrid Fiber-Optic Distributed Simultaneous Vibration and Temperature Sensing Technology and Its Geophysical Applications," Sensors **17**(11), 2511 (2017).

[18] M. A. Soto, G. Bolognini, and F. Di Pasquale, "Enhanced Simultaneous Distributed Strain and Temperature Fiber Sensor Employing Spontaneous Brillouin Scattering and Optical Pulse Coding," IEEE Photon. Technol. Lett. **21**(7), 450–452 (2009).

[19] Y. Muanenda, C. J. Oton, S. Faralli, T. Nannipieri, A. Signorini, and F. D. Pasquale, "Hybrid distributed acoustic and temperature sensor using a commercial off-the-shelf DFB laser and direct detection," Opt. Lett. **41**(3), 587 (2016).

[20] Y. Koyamada, M. Imahama, K. Kubota, and K. Hogari, "Fiber-Optic Distributed Strain and Temperature Sensing With Very High Measurand Resolution Over Long Range Using Coherent OTDR," J. Light. Technol., **27**(9), 1142–1146 (2009).

[21] G. K. White, "Thermal expansion of reference materials: copper, silica and silicon," J. Phys. D, **6**(17), 2070-2078 (1973).

[22] J. S. Sirkis and H. W. Haslach, "Interferometric stain measurement by arbitrarily configured surface-mounted, optical fibers," J. Light Technol., **8**(10), 1497–1503 (1990).

Chapter 4

Optical frequency-domain reflectometry

4.1 Introduction

Optical frequency-domain reflectometry (OFDR) was first proposed by Eickhoff and Ulrich [1] in 1981 as a technique to analyze single mode fibers with much higher spatial resolutions than those achievable with optical time-domain reflectometry (OTDR). Differently from standard OTDR, the OFDR scheme requires a continuous wave coherent source and a method to sweep the propagation constant of the light $\beta = \frac{\omega n}{c}$. For practical reasons, the most common solution is to linearly sweep the temporal frequency ω of the laser source, but other solutions were proposed in recent years including sinusoidal sweeps [2] or frequency combs sources [3]. Commercial devices based on the OFDR scheme are available [4], implementing solutions that guarantee a fast linear tuning of the laser frequency over a large bandwidth. Such devices exhibits high sensitivities with nominal spatial resolutions of micrometer at the cost, however, of an increased complexity, cost and measurement range limited by the laser coherence [5].Such performances allows to perform characterization of optical components [6] and sensing of both static [7] and dynamic measurements for practical applications in safety-related fields like geotechnical monitoring [8] and structural health monitoring [9], or in harsh environments like for cryogenic temperature monitoring [10] and superconducting magnets quench detection [11].

Distributed acoustic sensing (DAS) based on OFDR schemes have been proposed for the first time in 2012 by Bao et al. [12], with a setup that guarantees good sensitivity and

spatial resolution, but bandwidth values strongly limited to few Hz. Other schemes have been discussed in the years, like the time-gated OFDR [13] which guarantees instead good sensitivity and acoustic bandwidths of kilohertz at the cost however of a reduced spatial resolution of meters. Eventually the DAS performance can be improved in post-processing by implementing proper denoising algorithms [14], but the nature of the noise affecting the measurement must be analized throughfully in order to correctly implement such techniques. Recently DAS schemes exploiting the phase information of the Rayleigh backscattering trace were reported, with algorithms already achieving performance similar to the intensity-based counterparts [15]. The analysis of the phase of the backscattered trace is attractive because any perturbation acting on the fiber causes a corresponding distributed phase modulation, linear to the dynamic of the stress applied [16]. It is then possible to perform quantitative analysis of the perturbations acting on the fiber. Unfortunately, any stress occurring on a particular position affects also the backscattered light coming from further points of the fiber, making all the subsequent contemporaneous perturbations hard to identify [17].
In this chapter the setup of a standard OFDR will be discussed and the correspondence between the parameters of the setup and the performance will be highlighted. Then, the main results of my research focused on the development of a high-frequency, high-resolution DAS based on OFDR will be presented [18].

4.2 OFDR setup

The standard setup for an OFDR is shown in Figure 4.1. The continuous wave signal generated by a tunable light source (TLS) $s(t) = E_0 e^{-j\omega(t)t}$ is split by a 99/1 coupler into two signals of different amplitude, $s_{ai}(t) = 0.01s(t)$ and $s_{ofdr}(t) = 0.99s(t)$. The first signal $s_{ai}(t)$ is used in the auxiliary interferometer to create the clock signal that triggers the data acquisition (DAQ) system. The auxiliary interferometer is a standard Mach-Zehnder interferometer where a delay line of length L_{ai} is inserted in one of the two branches. The signal s_{ai} is equally divided between the two branches, and recombined at the end by means of 50/50 couplers. The output signal of the auxiliary interferometer is:

$$s_{out,ai} = E_0 e^{-j\omega(t+\tau_1)t} + E_0 e^{-j\omega(t+\tau_2)t} \tag{4.1}$$

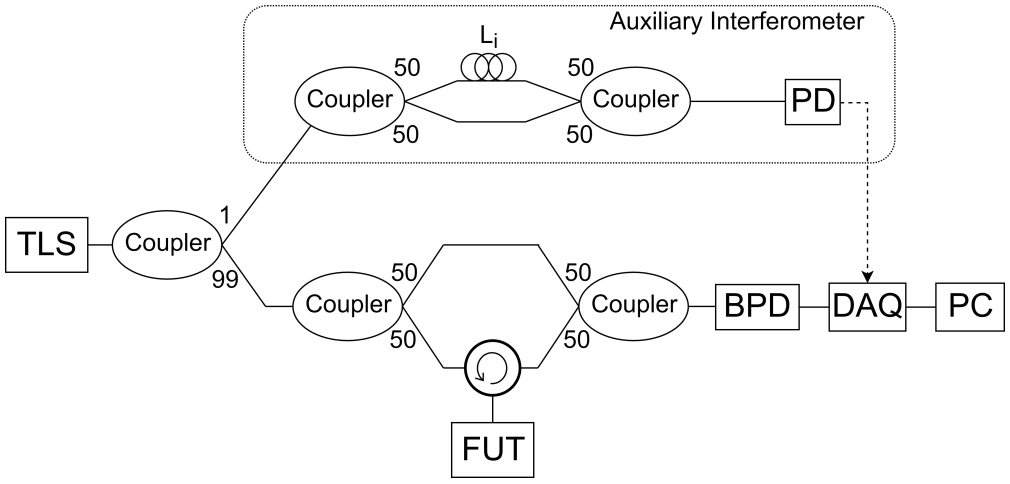

Figure 4.1. *Standard OFDR setup (the acronyms are explained in the text).*

where $\tau_1 = \frac{n_g(L_1+L_{ai})}{c_0}$ and $\tau_2 = \frac{n_g L_2}{c_0}$ are the delays accumulated during the propagation along the two paths of the interferometer, defining n_g as the fiber refractive index, c_0 as the speed of light and L_1 and L_2 as the length of the interferometer branches. Upon reception, the photodetector (PD) converts the signal in (4.1) into an electtrical signal by mean of direct detection:

$$i_{ai}(t) = |E_{out,ai}(t)|^2 = 2|E_0|^2 + 2|E_0|^2 cos(\omega(t)\Delta\tau(L_{ai})), \tag{4.2}$$

where $\tau(L_{ai}) = \tau_1 - \tau_2 = \frac{n(L_{ai}+(L_1-L_2))}{c}$.

As can be seen in 4.2 excluding the constant term, the pattern of the electrical signal $i_{ai}(t)$ is a sinusoidal function of $\omega(t)$. Such dependence is critical because of the way in which tunable laser source are usually implemented, which consists of an external cavity laser whose length can be linearly varied to generate a linear sweep of the wavelength, thus an inversely proportional shift of the frequency. Since the pattern of $i_{ai}(t)$ is related to $\omega(t)$, it will consequently shows non-uniformly spaced zero-crossing based on the non-linear frequency change of the laser. By triggering the data acquisition with such non-uniform clock, the backscattering signal samples acquired are linearized with respect to the frequency, guaranteeing the correct OFDR measurement.

The optical signal $s_{ofdr}(t)$ propagates to a different Mach-Zehnder interferometer with branches called respectively reference and measurement. The fiber under test (FUT) is reached through a circulator in the measurement branch and generates a backscattering signal that shows the same frequency sweep as $s(t)$, but with a progressively higher accumulated propagation delay. The backscattering signal is then recombined with

the signal coming from the reference arm and photodetected by balanced photodiodes (BPD) after a proper polarization-diverse scheme. Due to the time delay between the signal coming from the reference arm and the backscattering of the FUT, upon reception a beating signal $i(t)$ is generated, representing a compressed version of the frequency response of the fiber downshifted to an intermediate-frequency bandwidth. Since the frequency response of the fiber does not vary between consecutive acquisitions if the FUT is kept at rest, a proper analysis of $i(t)$ allows to perform distributed sensing.
The performance of the OFDR can be easily derived starting from the physical parameters of the components realizing the setup, which are:

- the total swept bandwidth B, in [Hz];
- the sweep rate σ, in [Hz/s];
- the length of the delay line of the auxiliary interferometer L_i, in [m].

The scan time, which defines the time window of the perturbations that can be observed with a single scan, and physically represent the time required to scan the entire bandwidth, can be directly derived as:

$$T_{scan} = \frac{B}{\sigma}. \tag{4.3}$$

Observing that the delay introduced by the delay line is $\tau_{ai} = \frac{n_g L_{ai}}{c_0}$, which induces a sampling frequency of $f_s = \sigma\tau_{ai} = \frac{\sigma n_g L_{ai}}{c_0}$, the number of samples generated in a single scan can be determined as:

$$N_{pts} = f_s T_{scan} = \frac{n_g L_{ai} B}{c_0}. \tag{4.4}$$

To perform a proper distributed analysis, the received time-domain beat signal $i(t)$ has to be Fourier transformed to the beat frequency domain. Since the scan time represents the temporal length of $i(t)$ it is possible to identify the spectral resolution as:

$$\delta f_B = \frac{1}{T_{scan}} = \frac{\sigma}{B} \tag{4.5}$$

Given that each scattering center in position z of the FUT generates a backscattering component that reaches the BPD after a delay $\tau(z)$, and that the propagation delays induces corresponding beat frequencies $f_B(z) = \sigma\tau(z)$, the beat frequencies domain

coincide, scaled, with the propagation delays domain and with the positions domain. The relations between the three transformed domains are the following:

$$\delta\tau = \frac{\delta f_B}{\sigma} = \frac{1}{B} \tag{4.6}$$

$$\delta z = \frac{c_0}{n_g}\frac{\delta\tau}{2} = \frac{c_0}{2n_g B} \tag{4.7}$$

By knowing the spatial resolution δz and the total number of points in the measurement, the maximum distance range can be identified:

$$\Delta z = \delta z N_{pts} = \frac{L_{ai}}{2}, \tag{4.8}$$

and consequently the maximum propagation delay and beat frequency can be computed:

$$\Delta\tau = \frac{2\Delta z n_g}{c_0} = \frac{L_{ai} n_g}{c_0}; \qquad \Delta f_B = \frac{2\Delta z n_g \sigma}{c_0} = \frac{L_{ai} n_g \sigma}{c_0}. \tag{4.9}$$

The original aim of the OFDR is to perform high spatial resolution measurement so, to minimize δz in (4.7), the only possibility is to increase the swept bandwidth B. The measurement range in (4.8) can be increased using longer delay lines, but for Δz the actual constraint is the coherence length of the laser source that cannot be arbitrarily extended. While the sweep rate does not appear directly into the relations of the OFDR parameters, it is better to have it as high as possible to increase the measurement speed and reduce the distortions caused by strong perturbations on the trace. Higher sweep rate however requires photodiodes with larger bandwidth since both the sampling frequency f_s and the maximum beat frequency Δf_B depends linearly on σ.

4.3 High-resolution, high-bandwidth algorithm

In this section we propose the data analysis algorithm presented in [18], based on the OFDR setup, that solves the issues of overlapped perturbations enabling the distributed detection of multiple high frequency stresses. High acoustic bandwidth of tens of kHz can be observed with spatial resolutions of centimeters. The algorithm performs a specific comparison of the phase of a reference OFDR trace, recorded before the perturbation, with the phase of a trace recorded during the perturbation. Moreover, a key aspect of the technique is a novel active compensation of the laser phase noise, described in

Sec. 4. The phase noise affecting the measurement is analyzed and the performance of the sensor are evaluated by computing the SNR of a signal in a progressively noisy environment.

4.3.1 Description of the proposed algorithm

Let's consider an ideal fiber at rest, with a strongly coherent light signal $s_{in}(t)$ propagating along $\hat{z}$ direction, characterized by a propagation constant $\beta(\omega) \approx \beta_0 + \omega\beta_1$. The fiber is considered short enough to neglect chromatic dispersion. The Rayleigh backscattering generated by the fiber can be modeled as the superposition of the reflections due to each scattering center [28]:

$$s_{out}(t) = \sum_n a_n \exp(-j\phi_n) s_{in}(t - \tau_n), \tag{4.10}$$

where z_n are the positions of the scattering centers, $a_n \in \mathbf{C}$ are the time-invariant scattering coefficients, $\phi_n = 2\int_0^{z_n} \beta_0 dz$ are the round trip phase terms and $\tau_n = 2\int_0^{z_n} \beta_1 dz$ are the round trip propagation delays. In a standard OFDR the input signal is linearly swept in frequency:

$$s_{in}(t) = s_0 \text{rect}\left(\frac{t}{T}\right) \exp(j\pi\sigma t^2), \tag{4.11}$$

where s_0 is an arbitrary amplitude, σ is the sweep rate and T is the sweep duration. At the receiver the backscattered signal of Eq. (4.10) interferes with the input one of Eq. (4.11), generating the signal:

$$i_0(t) \approx s_{out}(t) s_{in}^{\star}(t) \approx |s_0|^2 \text{rect}\left(\frac{t}{T}\right) \sum_n a_n \exp(-j\phi_n) \exp(-j2\pi\sigma\tau_n t), \tag{4.12}$$

where * stands for complex conjugate. Owing to the random nature of the amplitude a_n and position z_n of the scattering centers, the signal (3) is random. Nevertheless, as long as the fiber is not perturbed, $i_0(t)$ does not change and can therefore be considered as the fingerprint of the fiber [29]. To simplify the notation it is convenient to introduce a function $b(t; z_1, z_2)$ representing the summation of Eq. (4.12) when limited to the scattering centers between the positions z_1 and z_2. As an example, with this notation the signal for the fiber at rest can be decomposed in the contribution of two arbitrary subsections as:

$$i_0(t) = Kb(t; 0, L) = K\left(b(t; 0, z_0) + b(t; z_0, L)\right), \tag{4.13}$$

where $z = 0$ is the fiber input, L is the fiber length, z_0 an arbitrary point and $K = |s_0|^2 \text{rect}\left(\frac{t}{T}\right)$. Note that in an OFDR measurement the two contributions generate beat signals in different frequency bands, therefore the contributions can be easily separated with a filter.

If a time-varying stress $\varepsilon(t)$ is applied on a section of the fiber $I = [z_1, z_2]$, of length $\delta z = z_2 - z_1$, the elasto-optic effect causes a local change $\Delta\beta_0(t) \propto \varepsilon(t)$ on the propagation constant:

$$\tilde{\beta}_0(z,t) = \begin{cases} \beta_0 + \Delta\beta_0(t) & z_n \in I \\ \beta_0 & z_n \notin I. \end{cases} \tag{4.14}$$

The change in β_1 is negligible for any practical stress intensity, therefore the stress changes the phase term ϕ_n in (3) as follows:

$$\tilde{\phi}_n(z,t) = 2\int_0^{z_n} \tilde{\beta}_0(z,t)dz = \begin{cases} \phi_n & z_n \leq z_1 \\ \phi_n + \Delta\phi(n,t) & z_n \in I \\ \phi_n + \Delta\phi(t) & z_n > z_2, \end{cases} \tag{4.15}$$

where $\Delta\phi(n,t) = 2(z_n - z_1)\Delta\beta_0(t)$ is the phase perturbation induced along the section I, and $\Delta\phi(t) = 2\delta z\Delta\beta_0(t)$ is the space-invariant phase shift induced beyond the perturbed section. Consequently, the beat signal can be expressed as a sum of the three contributions generated by each fiber section as:

$$i_1(t) = K\left[b(t;0,z_1) + \tilde{b}(t;z_1,z_2) + \exp(-j\Delta\phi(t))b(t;z_2,L)\right], \tag{4.16}$$

where:

$$\tilde{b}(t;z1,z2) = K\sum_{n\in I} a_n \exp(-j(\phi_n + \Delta\phi(n,t)))\exp(-j2\pi\sigma\tau_n t). \tag{4.17}$$

Notice that the $b(\cdot)$ function appearing in the first and third contributions is exactly the same of the unperturbed fiber of Eq. (4.13), because the fiber span before section I is unperturbed, while the fiber span after section I is entirely affected by the same z-invariant phase perturbation $\Delta\phi(t)$. The Rayleigh signal generated by an arbitrary fiber section beyond section I can be easily obtained by applying a proper bandpass filter with impulse response $w(t)$ to the beat signal. Then, the perturbation can be calculated as:

$$\exp\left(-j\Delta\phi(t)\right) = \frac{w(t) * i_1(t)}{w(t) * i_0(t)}. \tag{4.18}$$

where $*$ denotes a convolution operation.

If K localized dynamic perturbations act on the fiber in different positions $z_{s,k}$, $k = 1, ..., K$, the phase variations $\Delta\phi_k(t)$ induced by each stress sum up, causing cumulative phase change terms that read as:

$$\tilde{\phi}_n(z,t) = \begin{cases} \phi_n & z_n \leq z_{s,1} \\ \phi_n + \Delta\phi_1(t) & z_{s,1} < z_n < z_{s,2} \\ ... & \\ \phi_n + \sum_k \Delta\phi_k(t) & z_{s,k} < z_n < z_{s,k+1} \\ ... & \end{cases} \tag{4.19}$$

where for simplicity we are omitting the fiber sections where the perturbations are acting, since they are not required in the analysis. Correspondingly, the beat signal can be expressed as

$$\begin{aligned} i_2(t) \approx K\Big[& b(t;0,z_{s,1}) + \exp(-j\Delta_1\phi(t))b(t;z_{s,1},z_{s,2}) + \\ & + \cdots + \exp\left(-j\sum_k \Delta\phi_k(t)\right) b(t;z_{s,k},z_{s,k+1}) + \dots \Big] \end{aligned} \tag{4.20}$$

where the k-th fiber section $I_k = [z_{s,k}, z_{s,k+1}]$ is affected only by z-invariant phase shifts. Generalizing the method discussed above for a single perturbation, the proposed solution to recover all the dynamics in the case of multiple perturbations consists in implementing a bandpass filter with a progressively increasing central frequency. The filter impulse response becomes $w(t; f_c(z))$, where $f_c(z)$ highlights the central frequency of the filter corresponding to a particular fiber position. Conceptually the bandpass filter acts as a moving window with bandwidth B_w and allows the distributed extraction of the local phase terms:

$$\exp\left(-j\sum_k \Delta\phi_k(t)\right) = \frac{w(t;f_c(z)) * i_2(t)}{w(t;f_c(z)) * i_0(t)}. \tag{4.21}$$

where $z \in I_k$.

When the filter bandwidth is completely inside the spectra spanned by $b(t; z_{s,k}, z_{s,k+1})$, the extracted phase coincides exactly with the cumulative phase terms reported in Eq. (4.19), otherwise some undesired distortions arise. However, by subtracting consecutive exact cumulative phase terms the single dynamic can be recovered.

The bandwidth B_w of the bandpass filter, expressed as a spatial width $L_w = c_0 B_w/(2n_g)$, defines the minimum spatial separation between any two consecutive perturbations to correctly extract at least one replica of each exact cumulative phase change $\sum_k \Delta\phi_k(t)$. If the distance between any couple of consecutive perturbations is greater than L_w then more replicas of such phase changes $\sum_k \Delta\phi_k(t)$ are extracted. The phases extracted at this point of the analysis are the cumulative effect of the perturbations acting along the fiber. The local information can be extracted by subtracting the phase terms calculated from two different windows separated by a distance ΔL. As a result, the parameter $SR = \Delta L + L_w$ represents the spatial resolution of our algorithm, since it defines the distance required to efficiently discriminate two consecutive perturbations. An increase of ΔL, which worsen the spatial resolution, allows for a SNR increase since a greater number of measured perturbation dynamic replicas can be averaged. The acoustic bandwidth achievable with this algorithm is $B_{a,max} = B_w/2 = n_g L_w/c_0$ and can be computed from the filter bandwidth according to the Nyquist theorem. A larger L_w guarantees an higher $B_{a,max}$ at the cost, however, of a worse spatial resolution.

If the perturbations acting on the fiber are not localized, the terms $\tilde{b}(\cdot)$, neglected in the previous analysis, become significant. The phase change terms $\Delta\phi_k(n,t)$ cannot be factorized, due to the dependence on position, resulting in an incorrect ratio operation in Eq. (4.21) which introduces distortions on the amplitude and dynamic of the extracted signals. When the stress intensities are not too high, such distortions are limited and the results can still be approximated with a sequence of phase terms with linearly increasing intensity, due to the progressively longer section of perturbed fiber considered. The dynamics and the positions of the perturbations can still be estimated with sufficient precisions.

4.3.2 Noise correlation analysis

The performance of the algorithm can be improved by averaging among replicas of the same perturbation measured at different fiber locations. The number of replicas available for averaging is $N_R = \Delta L/\delta L_w$ and depends on ΔL and on the spatial step of the moving bandpass filter δL_w. Assuming the noise affecting the different traces to be white, a smaller step should provide greater improvements at the cost of an increased computational time. Unfortunately any stress acting on the fiber, including undesired ones, generates a phase change term which sums coherently with all the others along

the fiber, causing a non negligible degree of correlation even among traces extracted from well separated positions. This is expecially true if the undesired perturbations are relatively large, since they will cause strong and well defined phase change terms that strongly correlate all the subsequent extracted phase traces and make averaging mostly insignificant. Small and uniformly distributed environmental stresses however can be assumed to be low and random enough that, along the fiber, the sum of all their contributions tends to cancel out. Without strong perturbations then the degree of correlation of traces extracted from increasingly separated positions will decrease and a proper step can be identified to perform a fast analysis with a meaningful averaging operation.

To verify experimentally how the degree of correlation of the noise changes, the reference and stressed OFDR traces of a bare fiber of length $L = 3$ m have been measured without applying any perturbation, i.e. with only environmental noise acting, and the analysis has been performed setting $L_w = 15$ cm, $\delta L_w = 0.1$ cm and $\Delta L = 15$cm. The noise correlation is computed among traces extracted in five increasingly separated positions of the fiber, respectively after $d_n = [0.1,\ 1,\ 5,\ 10,\ 15]$ cm, $n = 1, ..., 5$, with respect to the initial one located at the beginning of the fiber. The autocorrelation of the initial trace was computed to normalize, with respect to it, all the other values. No more positions have been investigated since the differentiation operation in the algorithm will remove any correlation in traces extracted from positions separated by a distance greater or equal to ΔL. The process was repeated along the whole fiber, by shifting forward the initial trace with steps of 15 cm, allowing the analysis on twenty non-overlapped sections. The results are reported in Fig. 4.2a where it can be seen that the behavior of the correlation degrees remain the same along the whole fiber. Traces extracted from positions 1 mm away are strongly correlated, eventually making the averaging operation less efficient, while a separation of 1 cm exhibits a very low correlation. For greater distances the degree of correlation decreases to zero as expected, but the number of traces collected becomes too low to guarantee a satisfactory noise reduction. Hence the value of $\delta L_w = 1$ cm was selected as the optimum one.

The other sources of noise that affect the system, mainly receiver noise and laser phase noise, can be modeled as uncorrelated white processes, for which the effectiveness of averaging is largely independent of δL_w.

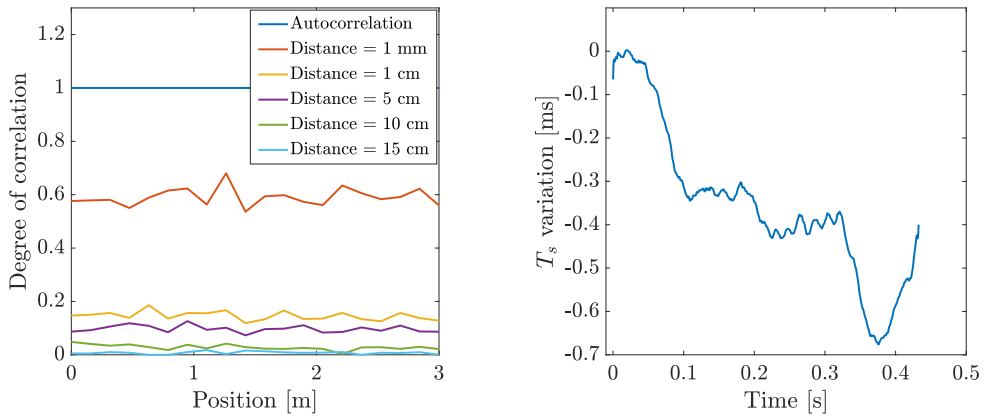

(A) (B)

Figure 4.2. *(a) Noise degree of correlation. (b) Undesired sampling period variations.*

4.3.3 Further linearization of the data acquisition trigger

The standard OFDR setup is based on a highly coherent source, linearly swept in frequency over a wide band, which generates the signal of Eq. (4.11). The linearity of the frequency sweep is usually guaranteed by an auxiliary interferometer which output allows to precisely trigger the data acquisition. As a consequence of this correction, the time scale of the measured data is distorted and not consistent with the time scale of the perturbation. If the data of the linearizing interferometer were available, this inconsistency could be corrected. However, this is not the case with commercial OFDRs.

To remove this distortions we stressed a section of fiber at the beginning of the link with a PZT driven by a known sinusoidal perturbation $\xi(t) = \xi_0 \sin(2\pi f_p t)$. The algorithm proposed previously can then be used to extract the distorted spectrum of such perturbation $\mathcal{F}\{\Delta\phi_p(t)\} = [S_b(f - f_p)]$, which will be a shifted version of the spectral broadening due to the spectral properties of $\xi(t)$. A homodyne demodulation scheme with a proper lowpass cut-off frequency, that should be low enough to cut-off the noise, but large enough to include all of the stress components, can then successfully retrieve an estimate of $S_b(f)$ and, by anti-transforming, an estimate of the undesired time variations. By resampling all the phase traces extracted from the subsequent spans of fiber, the spectral broadening can be effectively removed everywhere.

To experimentally verify the effects of the frequency sweep non linearity and the results of the proposed solution, a sinusoidal perturbation with a frequency arbitrarily set to $f_p = 3$ kHz was applied through a PZT in position $z_p = 2$ m of a 3 m long fiber. The algorithm parameters used where $L_w = 15$ cm, $\delta L_w = 1$ cm and $\Delta L = 15$ cm. Figure

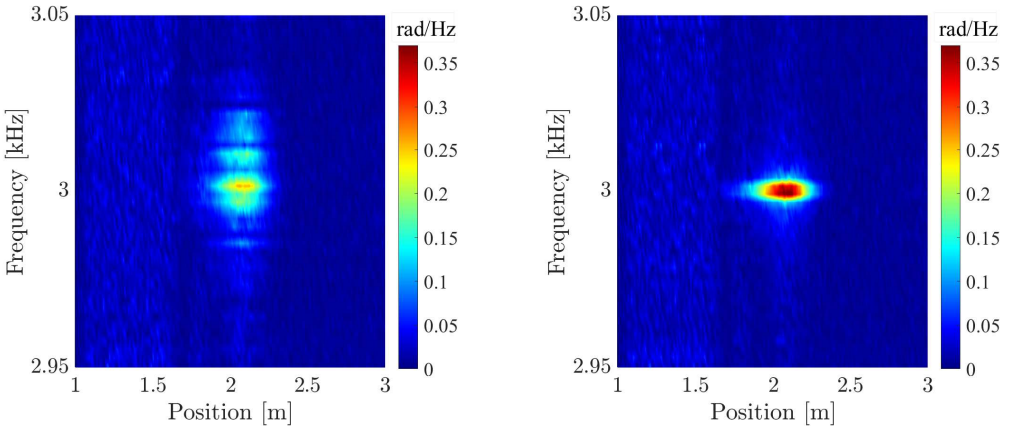

Figure 4.3. *(a) Perturbation spectrum before resampling. (b) Perturbation spectrum after resampling.*

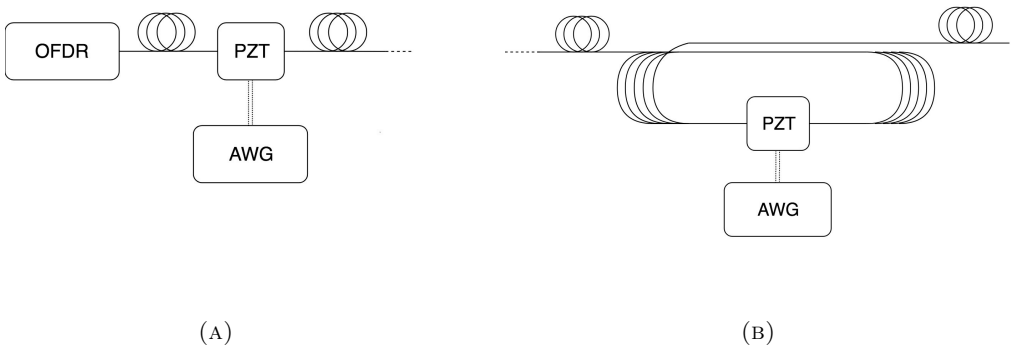

Figure 4.4. *(a) Interrogation unit of the sensor. (b) Fiber loops to realize multiple identical localized perturbations.*

4.3a shows the raw spectrum of the retrieved perturbation without any correction and, as can be seen, instead of a clean peak there is an evident spectral broadening with a 20dB-bandwidth of about 80 Hz. Through the homodyne demodulation scheme the spectral broadening is shifted back to baseband and a proper lowpass filter is applied. Considering our setup and instrumentation, a cut-off frequency $f_{co} = 160$ Hz, which is twice as large as the bandwidth of the observed perturbation, was selected. An instance of the undesired time sampling variations as function of the measurement time is shown in Fig. 4.2b. It is important to highlight that due to its intrinsically random nature, this is just an example and that it is thus not possible to find a general correction term. Finally, the perturbation spectrum after the resampling operation is shown in Fig. 4.3b where a clean spectral peak at f_p is clearly visible.

4.3.4 Experimental results

To experimentally demonstrate the possibility of sensing high frequency perturbations, thirty meters of a standard telecommunication fiber were connected to a commercial OFDR (OBR 4600, Luna Innovation) with a sweep rate $\sigma \approx 25$ THz/s. To correct the frequency scan non-linearities, as explained in the previous section, a known reference stress was applied through a PZT to the fiber section located immediately after the instrument. Such setup, shown in Fig. 4.4a, represents the interrogation unit of the sensors and it is left unchanged during all the following experiments.

The first test was performed by placing a PZT, driven by a sinusoidal signal at $f_{s,1} = 41$ kHz under the fiber in position $z_s = 4.60$ m. The algorithm parameters chosen for this first measurement were $L_w = 40$ cm, $\Delta L = 10$ cm, guaranteeing an acoustic bandwidth of $B_{a,max} = 50$ kHz and an effective spatial resolution of 50 cm. The filter step was fixed at the optimum value of $\delta L_w = 1$ cm, to guarantee a good number of traces for averaging while limiting the computational time. To assess the intrinsic performances of the technique, the reference and stressed traces were collected one right after the other, since the longer the time that elapses between the two measurements, the higher the environmental noise affecting the result. As can be seen in Fig. 4.5, which represents the spectrogram of the retrieved dynamic, the perturbation oscillating at $f_{s,1}$ is clearly visible around z_s. The extracted perturbation is spread over a length of 50 cm which corresponds to the effective spatial resolution achievable with the selected algorithm parameters.

The fiber has then been arranged in five loops with a common point placed above the PZT, as can be seen in Fig. 4.4b. The PZT was driven by an arbitrary signal generated as the sum of three sinusoidal waves oscillating at frequencies $f_{a,1} = 2.5$ kHz, $f_{a,2} = 5$ kHz and $f_{a,3} = 12.5$ kHz. The fiber layout ensures the application of the same perturbation to five different positions, and it allows to verify the capability of the proposed algorithm to discriminate between spatially distinguished, but spectrally overlapped stresses. To sharpen the spatial resolution, the filter spatial width was reduced to $L_w = 25$ cm, guaranteeing an acoustic bandwidth of $B_{a,max} \simeq 30$ kHz. The other algorithm parameters were left untouched resulting in a spatial resolution of 35 cm. After collecting the stressed and reference traces, the raw spectrogram was computed and reported in Fig. 4.6a, where the five perturbations oscillating at the three frequencies $f_{a,1}$, $f_{a,2}$ and $f_{a,3}$ are clearly discriminated. Even if the setup in Fig. 4.4b show that the

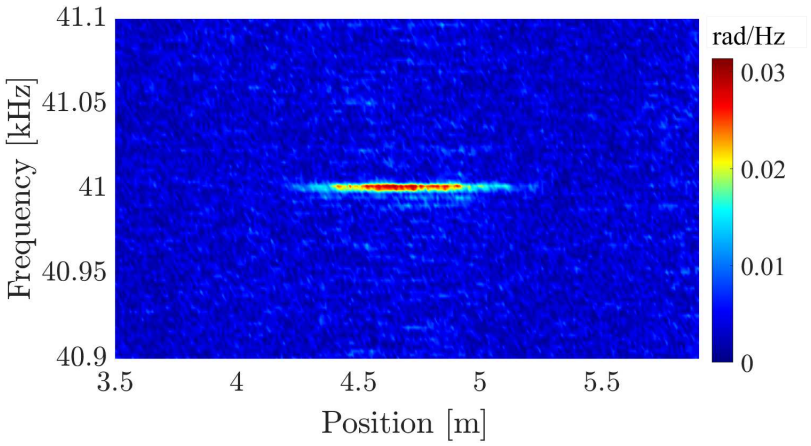

Figure 4.5. *Spectrum measured for a localized high-frequency sinusoidal perturbation at 41 kHz.*

same perturbation is applied to all fiber loops, the coupling coefficient between the PZT and the fiber is different for each loop, thus the experienced perturbation intensity will vary. This justifies the different amplitudes of the signals in Fig. 4.6a and is confirmed by measurements taken from the other end of the fiber. As can be seen in Fig. 4.6b, the amplitudes from the other end of the fiber appears almost identical to the ones in Fig. 4.6a, but with reversed positions. A further detail that can be observed from both Fig. 4.6b and 4.6a is the weak sideway propagation of the vibrations that appears on the side of some peaks. Given however the reduced amplitude, such phenomenon does not impair the quality of the measured results and instead highlight the sensitivity of distributed acoustic sensors based on the analysis of the phase of the Rayleigh backscattering signal.

To evaluate if the performance of the algorithm varies when multiple localized perturbations act on the fiber, two PZTs were placed under two different positions of a fiber $z_{s,1}$ and $z_{s,2}$, 1.5 meters away. The first PZT was used as an acoustic disturbance oscillating at the same frequency of the useful signal generated by the second PZT. The signal to noise ratio (SNR) was defined as the ratio between the power of the extracted useful signal with respect to the power of the noise and it was computed multiple times as a function of the acoustic signal-to-disturbance ratio (acoustic SDR), defined as the ratio between the power of the extracted useful signal with respect to the power of the disturbance, when the algorithm parameters ΔL and L_w were varied. Our analysis started by fixing the filter spatial width to $L_w = 15$ cm and by computing the SNR variations for different values of ΔL. The curves were normalized by the value of SNR obtained

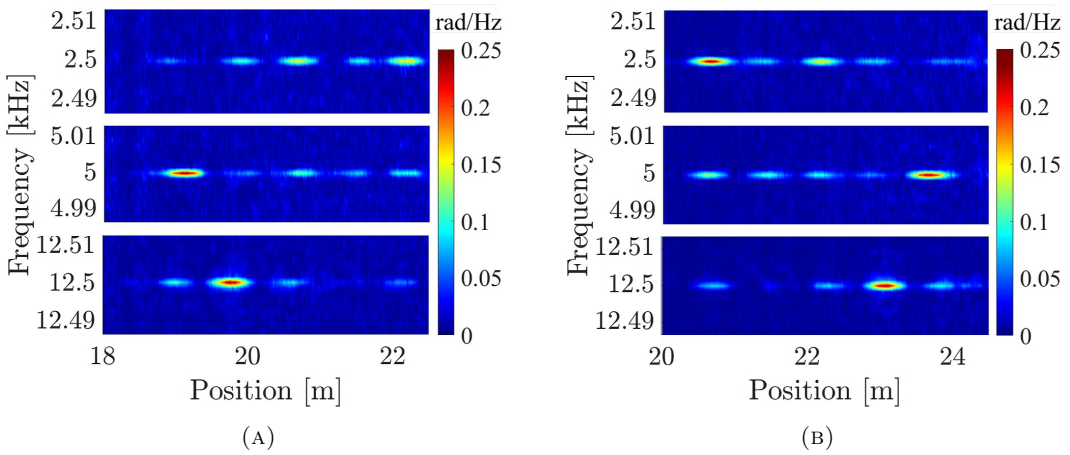

Figure 4.6. *Spectra of the phase measured when three different frequencies (2.5, 5 and 12.5 kHz) are applied simultaneously in five different positions along the fiber. Only the portions of the spectra around the main frequencies are shown for clarity. (a) Measurement taken in the forward direction. (b) Measurement taken in the reverse direction.*

for $\Delta L = 15$ cm and $L_w = 15$ cm, at maximum acoustic SDR. The result is shown in Fig. 4.7a, where it is possible to see that the SNR is almost constant with respect to the acoustic SDR. Since, as discussed in the previous section, all the traces in the spatial interval defined by ΔL represent the same perturbation, increasing such parameter allows to average more terms, obtaining an increase in the SNR at the cost of a duller spatial resolution. Figure 4.7b shows the SNR variations for different values of L_w, fixing $\Delta L = 15$ cm and normalizing the results for the same value as in the previous case. Once again the curves appear almost constant with respect to the acoustic SDR, except for high values of L_w. The reason is that for a filter with a wide spatial width the environmental noise affecting the traces impact more than for smaller ones, limiting the SNR and increasing the measurement uncertainty. For small value of L_w however, the influence of the receiver noise affects significantly the measurement, resulting in a lower SNR.

To experimentally verify the possibility of monitoring a spread stress the setup was then changed again including a fiber stretcher with an effective length of 12 meters. The displacement generated by the fiber stretcher is uniformly spread over the whole length of the fiber and depends on both the frequency and the amplitude of the driving signal. A sinusoidal driving signal $s_d = V_d \sin(2\pi f_d t)$ at frequency $f_d = 50$ kHz was applied and the analysis was performed by setting $L_w = 50$ cm and $\Delta L_w = 50$ cm, guaranteeing an acoustic bandwidth of 62.5 kHz with and an effective spatial resolution of $SR = 1$ m. To assess the intrinsic performance of the technique, the rms amplitude V_d of the signal was

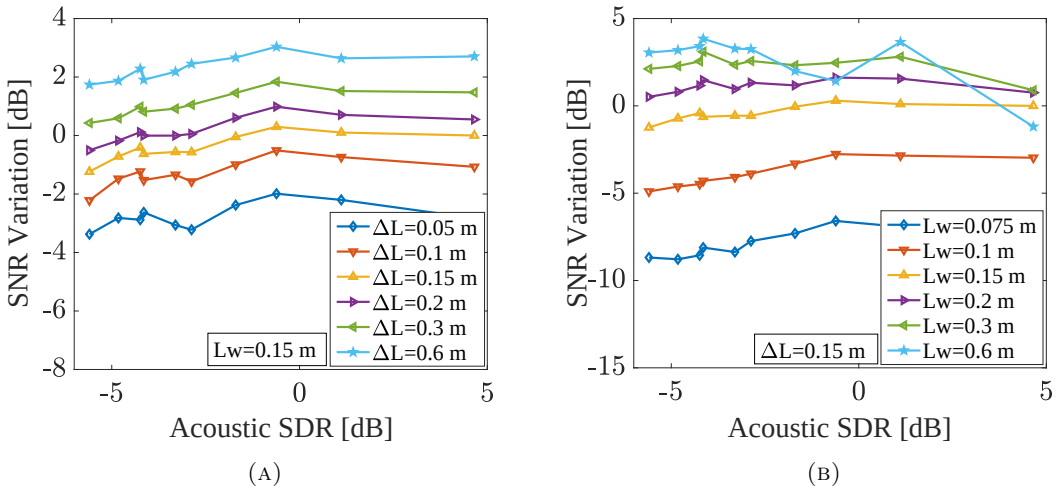

Figure 4.7. *(a) SNR as function of the acoustic SDR for different values of ΔL; (b) SNR as function of the acoustic SDR for different values of L_w.*

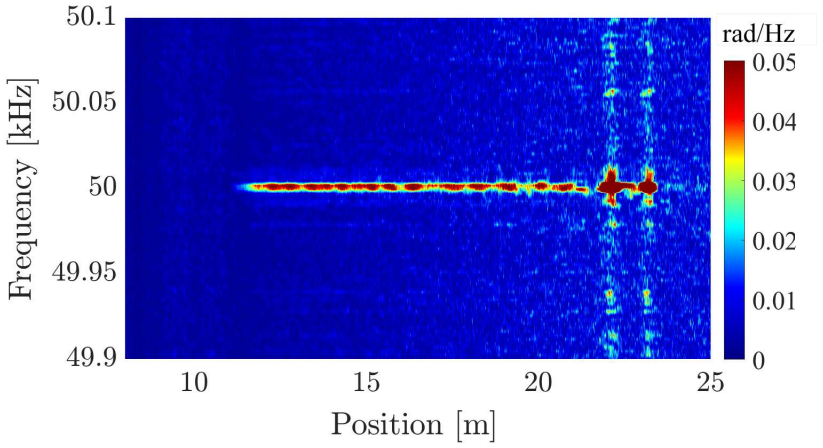

Figure 4.8. *Spectrum measured for a 12.3 meters long high-frequency sinusoidal perturbation at 50 kHz.*

set to just 0.15 V, so to avoid phase variations larger than 2π and the related problems of phase unwrapping. As can be seen in Fig. 4.8 the extracted signal is centered at f_d and the result of the differentiation operation is a 12 m long signal. Differently from the localized perturbation reported in Fig. 4.5, in Fig. 4.8 it is possible to see that the extracted perturbation is mostly flat, due to the linearly increasing phase change induced by the spread perturbation, but slightly more distorted both in amplitude and frequency. These distortions are caused by both the non constant coupling of the perturbation of the fiber and by the above-mentioned non ideal ratio operation that affects the performance of the algorithm. The strong distortions visible around $z = 23$ m in Fig. 4.8 are caused by the final connector of the fiber stretcher and are not significant.

The algorithm proposed allows the analysis of the magnitude of the stress as well. In the

Table 4.1. Comparison between the Nominal and Measured Values of the Modulation Constant of the Fiber Stretcher.

	20 kHz	30 kHz	40 kHz	43 kHz	47 kHz	50 kHz
Setting values [rad/V]	1.00	1.20	1.60	1.88	2.68	3.60
Measured values [rad/V]	0.86	1.38	1.95	2.13	2.17	3.15

case of the fiber stretcher, the generated displacement depends on both the amplitude and frequency of the driving signal. This relation is generally expressed through the modulation constant $\Delta\gamma(f)$ $\left[\frac{\text{rad}}{V}\right]$, which represents the phase change per Volt induced at a given frequency. If the differentiation operation of the algorithm proposed is avoided, it is possible to relate the total cumulated phase change induced by the fiber stretcher $\Delta\gamma(f)V_d$ when driven by a signal s_d to the phase term $\Delta\phi(t)$, defined in Eq. (4.15), extracted just before the final connector of the fiber stretcher:

$$\Delta\gamma(f_d)V_d = \frac{\Delta\phi(t)}{2} \tag{4.22}$$

where the factor 2 is due to the round trip of the light during the OFDR measurement. Experimental measurements have been performed applying a driving signal with variable voltage and frequency $s_d^{i,j}(t) = V_{d,i}\sin(2\pi f_{d,j}t)$, with $V_{d,i} \in [0.05, 0.10, 0.15, 0.20, 0.25]$ V and $f_{d,j} \in [20, 30, 40, 43, 47, 50]$ kHz. We tested more frequencies between 40 and 50 kHz due to the closeness to the resonance peak of the piezoelectric component and the consequent sharper increase of the modulation constant. The setting values of $\Delta\gamma(f_d)$ were computed by using the datasheet of the fiber stretcher and they are reported in the first row of Table 4.1. For each frequency $f_{d,j}$ the extracted values of $\Delta\phi(t)$ at different driving amplitudes were fitted with a first order polynomial function; the resulting slopes are reported on the second row of Table 4.1 and the R^2 value of the fitting was always around 0.95. As can be seen the data are correlated, even if there is a non negligible difference between them. The main cause of this variance can be found in the ratio operations described in Eqs. (4.18) and (4.21) which amplify the phase noise at those points where the signal amplitude is particularly low due to Rayleigh fading. A support to this argument is given by the fact that the ratio between the actual modulation constant (first row) and the measured one (second row) is on average about 1.02, i.e. very close to the ideal unity.

Bibliography

[1] W. Eickhoff and R. Ulrich, "Optical frequency domain reflectometry in single mode fiber," Appl. Phys. Lett. **39**(9), 693-695 (1981).

[2] L. Shiloh and A. Eyal, "Sinusoidal frequency scan OFDR with fast processing algorithm for distributed acoustic sensing," Opt. Express **25**(16), 19205 (2017).

[3] Z. He, T. Kazama, Y. Koshikiya, X. Fan, F. Ito, and K. Hotate, "High-reflectivity-resolution coherent optical frequency domain reflectometry using optical frequency comb source and tunable delay line," Opt. Express **19**(26), B764 (2011).

[4] "OBR Reflectometers.", *Luna, defying impossible.*, 17th September 2019, https://lunainc.com/product/reflectometers/.

[5] L. Palmieri and L. Schenato, "Distributed Optical Fiber Sensing Based on Rayleigh Scattering," The Open Optics Journal **7**(1), 104-127 (2013).

[6] B. J. Soller, D. K. Gifford, M. S. Wolfe, and M. E. Froggatt, "High resolution optical frequency domain reflectometry for characterization of components and assemblies," Opt. Express **13**(2), 666–674 (2005).

[7] M. Froggatt, B. Soller, D. Gifford, and M. Wolfe, "Correlation and Keying of Rayleigh Scatter for Loss and Temperature Sensing in Parallel Optical Networks," in Proceeding of OFC Technical Digest (2004), PDP17.

[8] L. Schenato, M. Camporese, S. Bersan, S. Cola, A. Pasuto, A. Galtarossa, P. Salandin, and P. Simonini, "Distributed optical fibre sensing for early detection of shallow landslides triggering," Sci. Rep. **7**(1), 14686 (2017).

[9] A. Barrias, J. R. Casas, and S. Villalba, "A Review of Distributed Optical Fiber Sensors for Civil Engineering Applications," Sensors **16**(5), 748 (2016).

[10] A. Chiuchiolo, L. Palmieri, M. Consales, M. Giordano, A. Borriello, H. Bajas, A. Galtarossa, M. Bajko, and A. Cusano, "Cryogenic-temperature profiling of high-power superconducting lines using local and distributed optical-fiber sensors," Opt. Lett. **40**(19), 4424 (2015).

[11] F. Scurti, S. Ishmael, G. Flanagan, and J. Schwartz, "Quench detection for high temperature superconductor magnets: a novel technique based on Rayleigh-backscattering interrogated optical fibers," Supercond. Sci. Technol. **29**(3), 03LT01 (2016).

[12] D. P. Zhou, Z. Qin, W. Li, L. Chen, and X. Bao, "Distributed vibration sensing with time-resolved optical frequency-domain reflectometry," Opt. Express **20**(12), 13138 (2012).

[13] S. Wang, X. Fan, Q. Liu, and Z. He, "Distributed fiber-optic vibration sensing based on phase extraction from time-gated digital OFDR," Opt. Express, **23**(26), 33301–33309 (2015).

[14] M. A. Soto, J. A. Ramirez, and L. Thevenaz, "Intensifying the response of distributed optical fibre sensors using 2D and 3D image restoration," Nat. Commun. **7**, 10870 (2016).

[15] D. Chen, Q. Liu, X. Fan, and Z. He, "Distributed Fiber-Optic Acoustic Sensor With Enhanced Response Bandwidth and High Signal-to-Noise Ratio," J. Light. Technol. **35**(10), 2037-2043 (2017).

[16] J. S. Sirkis and H. W. Haslach, "Interferometric stain measurement by arbitrarily configured surface-mounted, optical fibers," J. Light. Technol. **8**(10), 1497-1503 (1990).

[17] S. T. Kreger, J. W. Klein, N. A. A. Rahim, and J. J. Bos, "Distributed Rayleigh scatter dynamic strain sensing above the scan rate with optical frequency domain reflectometry," Proc. SPIE 9480, 948006 (2015)

[18] L. Marcon, A. Galtarossa, and L. Palmieri, "High-frequency high-resolution distributed acoustic sensing by optical frequency domain reflectometry," Opt. Express **27**(10), 13923 (2019).

[19] X. Bao and L. Chen, "Recent Progress in Distributed Fiber Optic Sensors," Sensors **12**(7), 8601-8639 (2012).

[20] S. V. Shatalin, V. N. Treschikov, and A. J. Rogers, "Interferometric optical time-domain reflectometry for distributed optical-fiber sensing," Appl. Opt. **37**(24), 5600-5604 (1998).

[21] M. Froggatt and J. Moore, "High-spatial-resolution distributed strain measurement in optical fiber with Rayleigh scatter," Appl. Opt. **37**(10), 1735-1740 (1998).

[22] R. Rathod, R. D. Pechstedt, D. A. Jackson, and D. J. Webb, "Distributed temperature-change sensor based on Rayleigh backscattering in an optical fiber," Opt. Lett. **19**(8), 593-595 (1994).

[23] B. J. Soller, D. K. Gifford, M. S. Wolfe, and M. E. Froggatt, "High resolution optical frequency domain reflectometry for characterization of components and assemblies," Opt. Express **13**(2), 666-674 (2005).

[24] Y. Lu, T. Zhu, L. Chen, and X. Bao, "Distributed Vibration Sensor Based on Coherent Detection of Phase-OTDR," J. Light. Technol. **28**(32), 3243-3249 (2010).

[25] A. K. Sang, "Distributed Vibration Sensing using Rayleigh Backscatter in Optical Fibers" Ph.D Thesis, Virginia Polytechnic Institute and State University (2011).

[26] H. Gabai and A. Eyal, "On the sensitivity of distributed acoustic sensing," Opt. Lett. **41**(24), 5648-5651 (2016).

[27] J. Pastor-Graells, H. F. Martins, A. Garcia-Ruiz, S. Martin-Lopez, and M. Gonzalez-Herraez, "Single-shot distributed temperature and strain tracking using direct detection phase-sensitive OTDR with chirped pulses," Opt. Express **24**(12), 13121-13133 (2016).

[28] P. Healey, "Statistics of Rayleigh backscatter from a single-mode optical fibre," Electron. Lett. **21**(6), 226-228 (1985).

[29] S. T. Kreger, D. K. Gifford, M. E. Froggatt, B. J. Soller, and M. S. Wolfe, "High Resolution Distributed Strain or Temperature Measurements in Single- and Multi-Mode Fiber Using Swept-Wavelength Interferometry," in *Optical Fiber Sensors*, OSA Technical Digest (CD) (Optical Society of America, 2006), paper ThE42.

Chapter 5

Distributed sensing at cryogenic temperatures

5.1 Introduction

As reported in [1], the assessment of advanced technologies and devices designed to operate in cryogenic environments for several fields of applications, such as aerospace vehicles, superconducting magnets, and high-energy physics experiments [2, 3], is leading to an increasing interest in the development of accurate cryogenic sensors. Long-term robustness and reliability have to be insured to guarantee good operation and safe working conditions of the equipment. To date, resistive sensors represent the standard technology commonly used to meet the requirement of monitoring wide temperature ranges from room temperature down to ultra-low temperature in harsh environments and extreme working conditions. However, some of their limitations, typically associated with their sensitivity to the magnetic field and the amount of electrical wires needed for their operation, may be efficiently overcome by implementing fiber-optic-based monitoring systems.

Optical fibers rely on appealing advantages such as reduced spatial occupation, and electromagnetic interference immunity. The application of fiber-optic sensors (FOS) at cryogenic temperatures is, however, not straightforward. Among the fiber-optic technologies considered so far, the most promising ones for low-temperature monitoring are fiber Bragg grating (FBG) and Rayleigh backscattering based distributed fiber-optic sensors (DOFS). Bare-silica FBG sensors and fiber are not effective for cryogenic applications because of the thermo-optic and thermo-elastic coefficients of silica becoming negligible

below 40 K [4, 17]. In particular, experiments conducted down to 2.2 K [5] highlighted the need to consider additional coatings able to transfer a temperature variation into a measurable strain [6]. Several materials and coating techniques have been explored in order to realize coated optical fiber thermal sensors operating at cryogenic temperatures [7]. The material selection mainly focuses on the thermal expansion coefficient (CTE) of the host material (coating material) in order to achieve a good thermo-mechanic response (thermal apparent strain) from the grating, also at temperatures in which the pure thermal effect of silica starts to be negligible. Besides maximizing the CTE values at cryogenic temperatures, the selected coating material must also exhibit a good adhesion to the fiber, which is fundamental to assure a good strain transfer. The final coatings geometries and thickness must avoid residual radial and longitudinal stresses, which can compromise the quality of the reflection spectrum of the fiber or of embedded grating.

The use of Raman or Brillouin scattering in this field has highlighted that the main limitations are, respectively, a sever lack of sensitivity and a highly non-monotonic behavior [11]. Differently, DOFSs based on Rayleigh backscattering, and in particular those implementing optical frequency domain reflectometry (OFDR) which guarantees high sensitivity and spatial resolution over the considered lengths with respect to the time-domain alternative, have found preliminary successful applications [12–14]. Recalling that an OFDR works by comparing the spectra reflected by a fiber section at two different times, it is possible to understand if that section has experienced a variation of temperature and/or strain by measuring the eventual wavelength shift. Owing to the high sensitivity of the Rayleigh backscattering it is difficult in practice (although not impossible in principle) to relate an absolute Rayleigh reflected spectrum to an absolute temperature and strain condition. Therefore, only relative strain and/or temperature changes can be reliably measured. In any case, the relationship between the measured wavelength shift and the applied strain/temperature variation, as discussed in section 2.3, depends on the characteristics of the fiber (its non-linear thermo-optic coefficient) and its coating (causing strain on top of the thermo-optic effect) and, hence, needs to be calibrated. Despite being subject to a decrease in thermal sensitivity, Rayleigh scattering does not loose sensitivity to strain at cryogenic temperatures. Therefore, appropriate coatings [13] and fiber design [16] can impact the thermo-mechanical behavior of the fiber, preserving high sensitivity.

In this chapter the results of the research performed in collaboration with the European Organization for Nuclear Research (CERN) will be presented and discussed. The first section will focus on the computation of the calibration curves for four optical fiber samples with different coatings, namely acrylate of external diameter $ED = 250$ μm, PEEK of external diameter $ED = 400$ μm, polyimide of external diameter $ED = 155$ μm and acrylate of external diameter $ED = 400$ μm. Such calibration curves have been computed by inserting the fiber samples into a cryocooler which allows a fine tuning of the temperature between 5 and 300 $°K$. The calibrations curves have then been used in the monitoring of a 50 meter long superconducting power link (SC-Link) by means of fibers with coatings in acrylate of external diameter $ED = 250$ μm and PEEK of external diameter $ED = 400$ μm. The temperatures measured with the distributed fibers are validated by comparison with the results of standard resistive sensors (CERNOX). Finally the cooldown and the powering of a high-temperature superconducting (HTS) magnet called Feather 2 (FM 2) is monitored through several optical fibers with coating in polyimide and external diameter $ED = 155$ μm impregnated directly on top of the magnet superconducting cables.

5.2 Fibers thermal responses at cryogenic temperatures

The first experiment performed in collaboration CERN, consisted in computing the calibration curves and the sensitivity of four optical fiber samples coated with different materials, namely acrylate of external diameter $ED = 250$ μm, PEEK of external diameter $ED = 400$ μm, polyimide of external diameter $ED = 155$ μm and acrylate of external diameter $ED = 400$ μm. The four fiber samples were selected based on their theoretical thermal properties which makes them potentially good candidates for cryogenic temperatures monitoring. The fibers are interrogated by means of an optical frequency domain reflectometer (OFDR), whose working principle has been explained in details in the previous chapter.

Supposing that the temperature of the fiber is lowered to cryogenic levels and in particular below a temperature of 40 K, the thermo-optic coefficient α_{TO} and the thermo-elastic coefficient α_{TC} of the silica becomes negligible [17]. Due to the specific thermal properties of the polymers, the coating of the fiber will continue to shrink also for lower temperaturesand, as long as the coating properly adheres to the silica fiber, its shrink

will induce a measurable strain. The consequent wavelength shift allows to perform distributed temperature sensing by means of OFDR also at cryogenic temperatures. The relation between the wavelength shift measured with the OFDR and the temperature change of the fiber is however non-linear, because of the non-linear behavior of the thermo-optic coefficient α_{TO} and of the contemporaneous action of strains and thermal contraction. Moreover, the wavelength shift extracted by the OFDR is relative to the temperature change experienced by the fiber with respect to a reference measurement: the same wavelength shift will correspond to a completely different temperature change if the reference was collected when the fiber was at room temperature, with respect to cryogenic temperature. To realize a reliable distributed temperature sensor based on optical fiber it is then fundamental to compute the calibration curves of the specific fiber in use and to duly note the temperature of the fiber T_{ref} when the reference backscattering trace was collected. All the wavelength shifts will correspond to a temperature change with respect to that reference temperature. Nevertheless, if the experimental measurement is performed using a reference trace collected when the fiber was at a temperature T_{exp} different from T_{ref}, it is not necessary to recompute the calibration curve. By extracting analytically the wavelength shift $\Delta\lambda(\Delta T)$ induced by the temperature change $\Delta T = T_{ref} - T_{exp}$ it is enough to add it to any further shift measured to obtain a result analogous to performing the measurement with the reference at T_{ref}. As a final remark, to avoid error in the calibration curves, the fiber must be monitored using a strain-free setup, so that only the effects generated by the temperature change will induce the measured wavelength shifts.

The calibration curves not only convert an optical fiber into a reliable temperature sensor, but also allow to extract the sensitivity of the fiber as a function of the temperature, which is a fundamental parameter in the evaluation of the performance of the fiber for cryogenic temperatures monitoring. For instance, the temperature at which the sensitivity drops below a minimum threshold, thus making the measurement not reliable since even a small noise-induced peak in the wavelength shifts will be strongly amplified during the conversion to temperature, will depend on the properties of the coating and allows for comparisons. The sensitivity of the fiber can be easily extracted from the calibration curves by computing their first-order derivative with respect to the temperature.

(A)

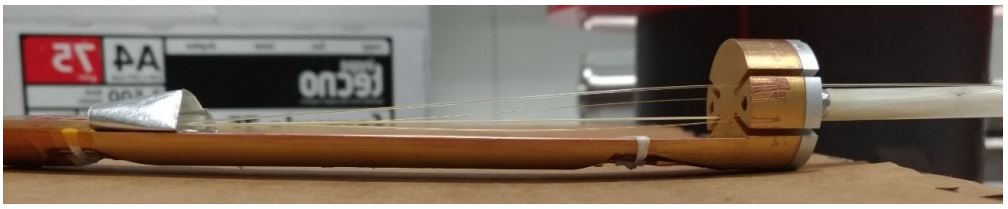

(B)

Figure 5.1. *(a) Top view of the four fiber samples in the cryocooler insert. (b) Side view of the four fiber samples in the cryocooler insert. Looking at the top of the insert and moving clockwise the fibers samples are: Acrylate 250, Acrylate 400, Polyimide 155, PEEK 400.*

5.2.1 Experimental setup

The experimental setup for this first experiment consisted in an OBR 4600 built by Luna Inc [18]. connected to a 1x4 optical switch which allowed the monitoring of four fiber samples, with different coatings and external diameter, during three repeated thermal cycles in the temperature range $T \in [5, 300]$ K. The fibers were inserted into a particular device, called cryocooler, where a closed feedback helium circuit allowed a fine tuning of the temperature of a small cryostat. An angled cut of 8° was realized at the end of each fiber sample to reduce undesired reflections. The cuts were protected from damages by inserting the last 2 cm of fiber into a 4 cm all-plastic heat-shrinkable protective sleeve. The fiber samples were connected to the optical switch through gas-tight FC/APC connectors embedded in the sealing valve of the cryocooler. The cryocooler consisted of a small cryostat of vertical length $L \approx 20$ cm and diameter $D \approx 10$ cm where a small rectangular plate of dimension 15×2 cm, called insert, could be inserted from the top without touching the surrounding walls. Two small pipes at the bottom of the cryostat allowed a tunable flow of helium gas, which was feedback-controlled by the CERNOXs to guarantee a fine control of the temperature in the range $T \in [5, 300]$ K.

The four fiber samples were 1.5 meter long to account for the length of the pipes in the cryocooler but, as can be seen in Figure 5.1b and 5.1a, only the last $z_{samples} = 15$ cm were placed on the insert, with a particular care to not let them touch the metallic plate. The

fibers were loose on the top end, to avoid strain, and fixed with Kapton tape on bottom end to prevent floating. Close to the top and bottom positions of the insert two extra electrical temperature sensors were fixed with a small white elastic band. The sensor closer to the insert top end, at position $z_B = 0.02$ m from the top of the insert, was called *CERNOX B* while the other, at position $z_C = 10.5$ cm, was called *CERNOX C*. To avoid as much as possible the temperature changes and strains introduced by the insert plate and by the Kapton tape, the wavelength shifts were extracted in correspondence to z_B and compared with the temperature measured by CERNOX B. To simplify the notation, from now on the fiber samples will be called after the material of their coating and by their diameter, i.e. *Acrylate 250*, *PEEK 400*, *Polyimide 155* and *Acrylate 400*. Both the OBR and the optical switch were electronically synchronized in order to select the fiber sensors and perform the measurement autonomously at a fixed rate. The OBR was set-up to scan $B = 88$ nm of optical bandwidth with a sweep rate $\sigma = 200$ nm/s, thus allowing a maximum measurement rate of $F_{s,agg} \approx 2$ Hz that has to be divided between the four channel, obtaining an effective measurement rate per fiber of $F_s \approx 0.5$ Hz. The sensor gauge, which defines the spatial resolution, was set to $SG = 1$ cm and the spacing between consecutive sample was set to $SS = 0.25$ cm.

5.2.2 Results

The cryocooler was programmed to perform three thermal cycles, at a slow pace, from room temperature $T_r = 300$ K to the minimum temperature possible $T_{min} \approx 5$ K. At the end of each cooldown and warmup phase the temperature was kept stable for a couple of hours to guarantee a complete thermalization of the fiber samples. Due to the slow temperature change induced, the sampling rate F_s was reduced to one measurement per fiber per minute to prevent memory consumption. The wavelength shifts were then extracted using as reference a trace collected when the temperature in the cryostat was exactly $T_r = 300$ K and the temperature data from both CERNOXs were saved at time instants corresponding to the measurements of the fiber samples.

The first thing that has been verified was the possible hysteresis of the fiber due to lamination of the coating from the fiber, or other unexpected events. The wavelength shifts measured in position z_B for the four fiber samples and for all three complete thermal cycles, thus both the cooldowns and warmups of the fibers, have been represented with a scattering plot as a function of the temperature measured by CERNOX B at

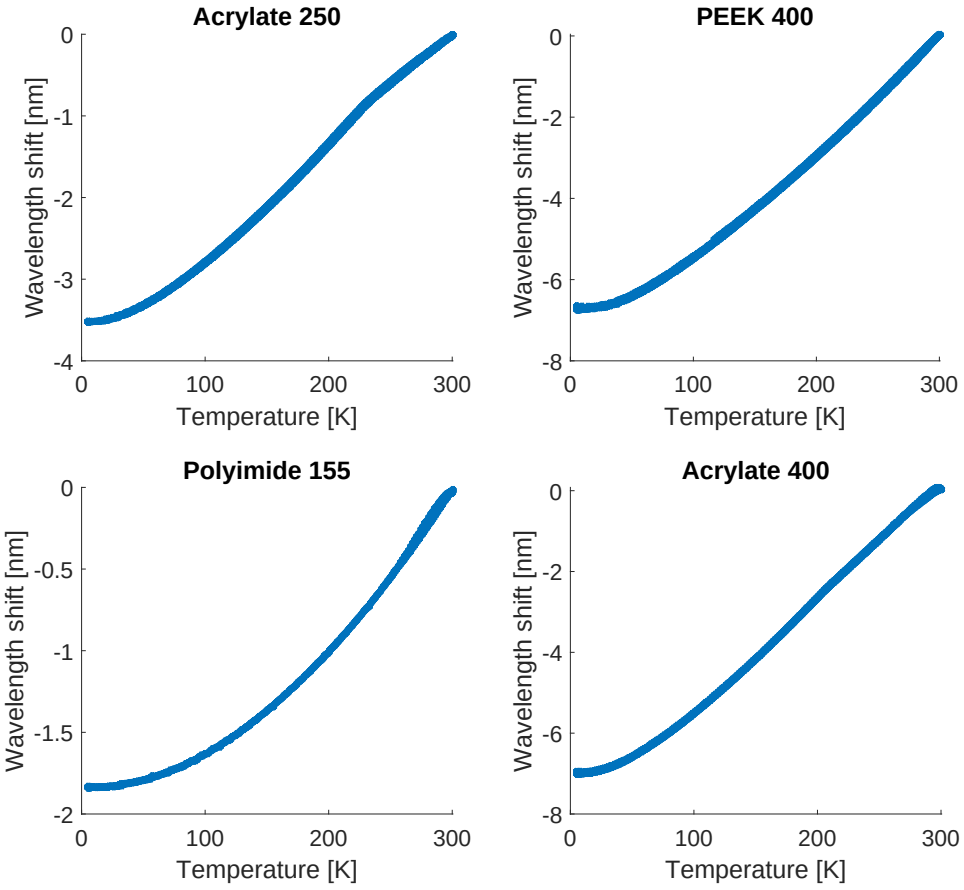

Figure 5.2. *Scatter curves of the wavelength shift vs temperature, for the four fiber samples*

corresponding time instants. The results are shown in Figure 5.2. As can be seen, the points of the curves are sufficiently overlapped confirming that no significant hysteresis were induced during the thermal cycles, and that the measurements are repeatable. The Acrylate curves in Figure 5.2 exhibit similar behaviors with however different magnitudes, differently from Polyimide 155 which approaches a parabolic shape and PEEK 400 that seems almost linear till 75 K. The calibration curves, for the reference temperature $T_f = 300$ K, were computed by fitting the data in Figure 5.2 with polynomial functions of order 6 and are shown in Figure 5.3a. As can be seen, an apparent linear dependence between the thickness of the coating and the maximum wavelength shift may be inferred. Such relation was expected since the wavelength shift is generated by the strain between the coating and the fiber, and the thicker the coating, the stronger the strain.

The sensitivities of the fiber samples are extracted by computing the first derivative of

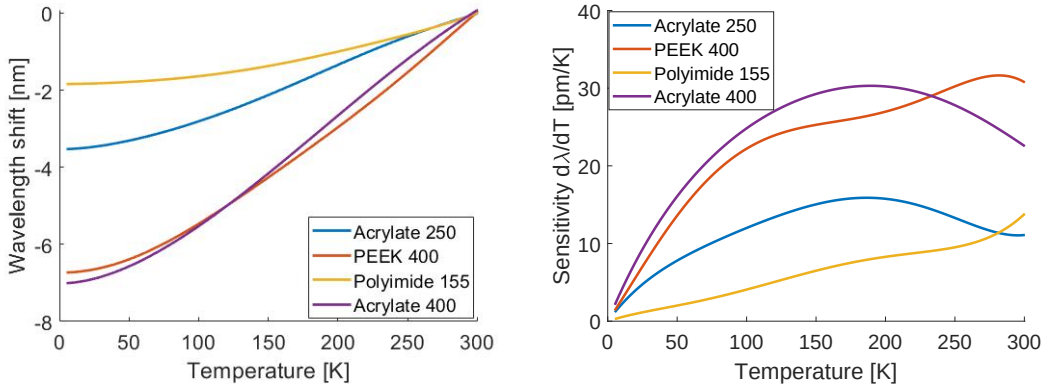

(A) (B)

Figure 5.3. *(a) Calibration curves for the four different fiber samples obtained after 6th degree polymonial fit. (b) Sensitivity curves for the four different fiber samples.*

the calibration curves and the results are shown in Figure 5.3b. As can be seen, for temperatures close to the absolute zero all the fiber samples shows almost null sensitivity. The sensitivity of Polyimide 155 is the lowest between the four samples, but shows a very good linearity over the whole temperature range, confirming that its calibration curve effectively approaches a parabolic shape. Both acrylate samples show a bell-shaped sensitivity with a peak centered around 180 °K. Finally the PEEK sample shows the highest sensitivity at high temperature, but fall below the Acrylate 400 sample for temperatures lower than 230 °K. Figure 5.3b further confirms the benefit of a thicker coating, as the higher sensitivity of PEEK 400 and Acrylate 400 guarantees a reliable wavelength shifts even for very low temperatures. Finally it can be seen that the calibration curves and the sensitivities computed for the Acrylate 250 and Polyimide 155 samples strongly agree with the results published in [1], further confirming the repeatability of the measurement.

The fits representing the calibration curves where then tested by converting the wavelength shifts measured during the thermal cycles into the corresponding absolute temperature of the cryocooler. As can be seen from Figure 5.4, the temperatures measured with CERNOX B and with the four fibers strongly agree. A more accurate analysis of the quality of the calibration curves extracted however, can be performed observing the errors between the temperatures measured with CERNOX B and with the fiber samples, which are shown in Figure 5.5. As can be seen Polyimide 155, characterized by the lowest sensitivity, exhibits high errors with magnitudes reaching up to 5 K. For the other fiber samples instead, the magnitude of most errors falls below the 2 K threshold, even if a general increasing behavior can be observed for low temperatures where the sensitivity

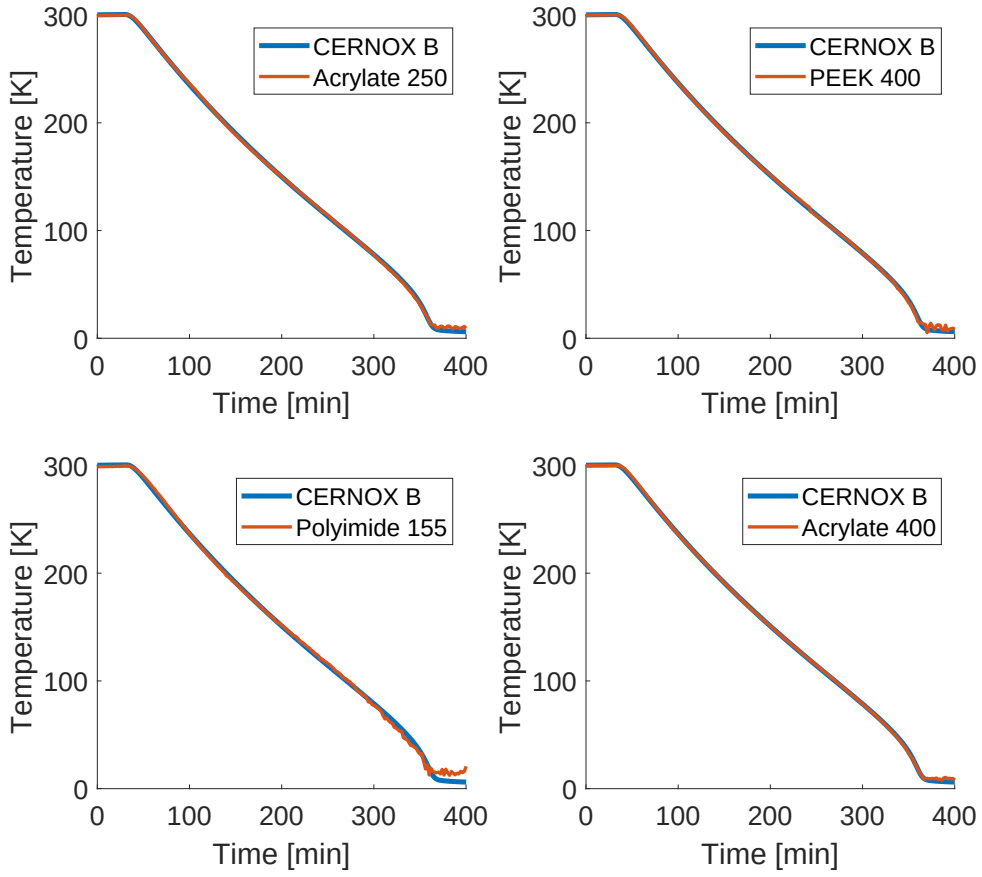

Figure 5.4. *Comparison between the absolute temperature measured with the electrical sensor CERNOX B and the temperature measured with the fiber samples after calibration.*

start to decrease. All the curves in Figure 5.5 show a more or less evident oscillating behavior which is induced by the non ideal polynomial fit performed. A more precise analysis of the thermal response of the fiber for cryogenic temperatures may eventually highlight a model that fit the experimental data with higher precision.

5.3 Cooldown of a superconducting link

The second experiment performed at CERN consisted in monitoring the cooldown of a $L_{SCL} = 55$ meter superconducting link (SC-LINK), which is being developed to allow a more efficient current transport from the power supply to the superconducting magnets. The SC-LINK consists of a superconducting cable inserted into a flexible pipe thermally isolated by layers of specific isolating materials and pumped void. The ends of the pipe are closed by two pumps, called respectively Feedbox and Returnbox, which allows to blow helium gas at a temperature of about 50 K into the pipe. The helium flows from

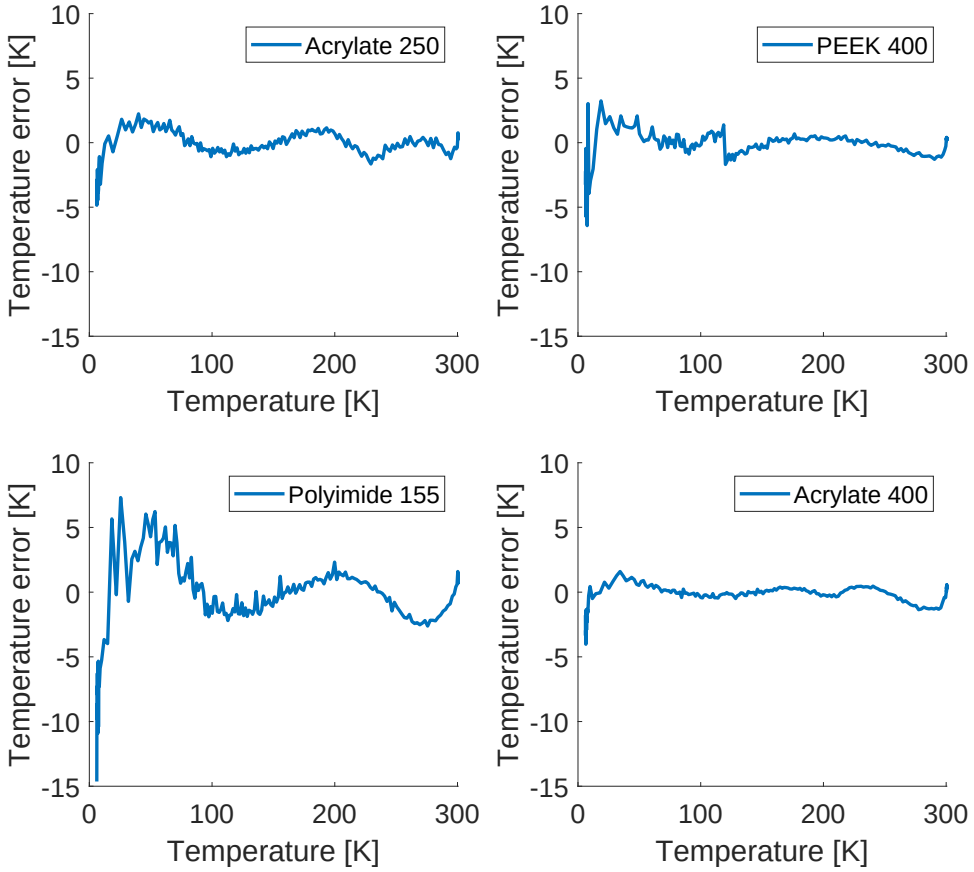

Figure 5.5. *Errors between the absolute temperatures measured with the electrical sensor CERNOX B and the temperatures measured with the fiber samples after calibration.*

the Feedbox toward the Returnbox, thus inducing a non-uniform cooldown of the link until full thermalization is reached. Close to the superconducting cable, a 2 centimeter wide flexible polymeric strip of length equal to L_{SCL} was deployed, carrying on top two fibers with different coatings, namely Acrylate 250 and PEEK 400 of respective length $L_{a,250} = 55$ meter and $L_{P,400} = 25$ meter. The fibers were loose to perform strain-free measurement, but kept into position by parallel polymeric rings of 2 mm diameter (much larger than the external diameter of the fiber), uniformly spaced (≈ 1 m) along the full length of the strip. As for the previous experiment, the final ends of the fibers were cut with an 8° angle to reduce undesired reflections and protected by mean of all-plastic heat-shrinkable protective sleeves. The fibers in the SC-Link are monitored through gas-tight FC/APC connectors embedded in a sealing valve on the Returnbox, thus the farthest positions along the fiber will be closer to the Feedbox and will experience the cooldown earlier. The interrogation system used to monitor the wavelength shifts of the

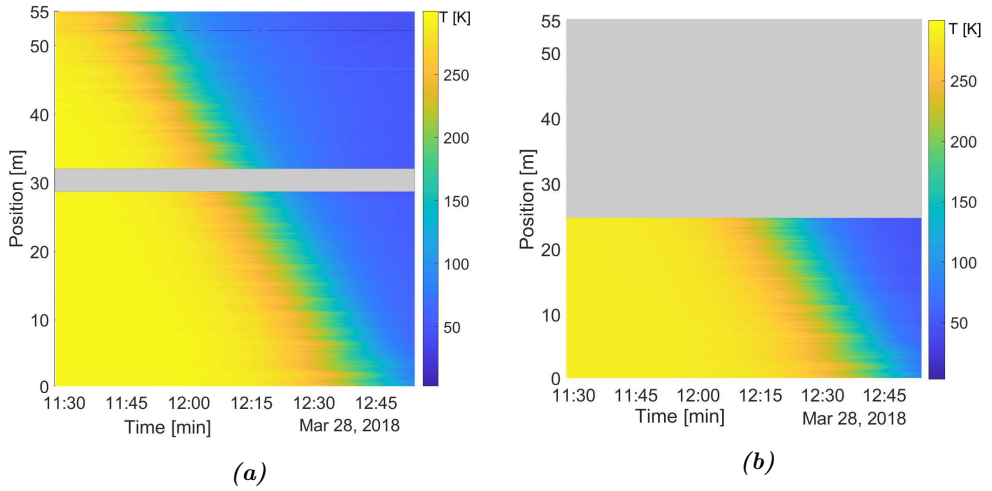

Figure 5.6. *(a) Cooldown of the SC-Link monitored with the Acrylate 250 fiber. (b) Cooldown of the SC-Link monitored with the PEEK 400 fiber.*

two fibers consisted of a LUNA Inc. OBR 4600 connected and synchronized to a 1x4 optical switch to autonomously acquire the traces. Only two of the four channels of the switch were used, guaranteeing a maximum measurement rate per fiber of $F_s = 1$ Hz. To avoid excessive storage consumption, the measurement rate was reduced to two measures per minutes. Due to the long length of the fibers to monitor, the sensor gauge, which defines the spatial resolution, was set to $SG = 10$ cm and the spacing between consecutive sample was set to $SS = 2.5$ cm. Due to technical issues during the deployment of the Acrylate fiber, the data acquired from positions $z \in [28.5, 32]$ m were not reliable and have been removed from the analysis.

The temperature of the SC-Link was then reduced from $T_{11:30} \approx 300$ K to $T_{13.00} \approx 50$ K in about 1h and 30 minutes, blowing helium from the Feedbox to the Returnbox. The wavelength shifts induced on the backscattering traces by the temperature change were measured and the calibration curves presented in the previous section were used to convert them into temperatures. The results are shown in Figure 5.6a and 5.6b, respectively for the Acrylate 250 and PEEK 400. As can be seen, considering only the first 25 meter where both fibers were monitoring, the temperatures measured as a function of the position and the dynamic of the cooldown strongly agree between the two fibers and, as expected, they show a propagation of the cooldown starting from the positions closer to the Feedbox.

A more accurate analysis of the results can be seen in Figure 5.7 where the temperatures measured by the two fibers are compared with the temperatures measured by electrical

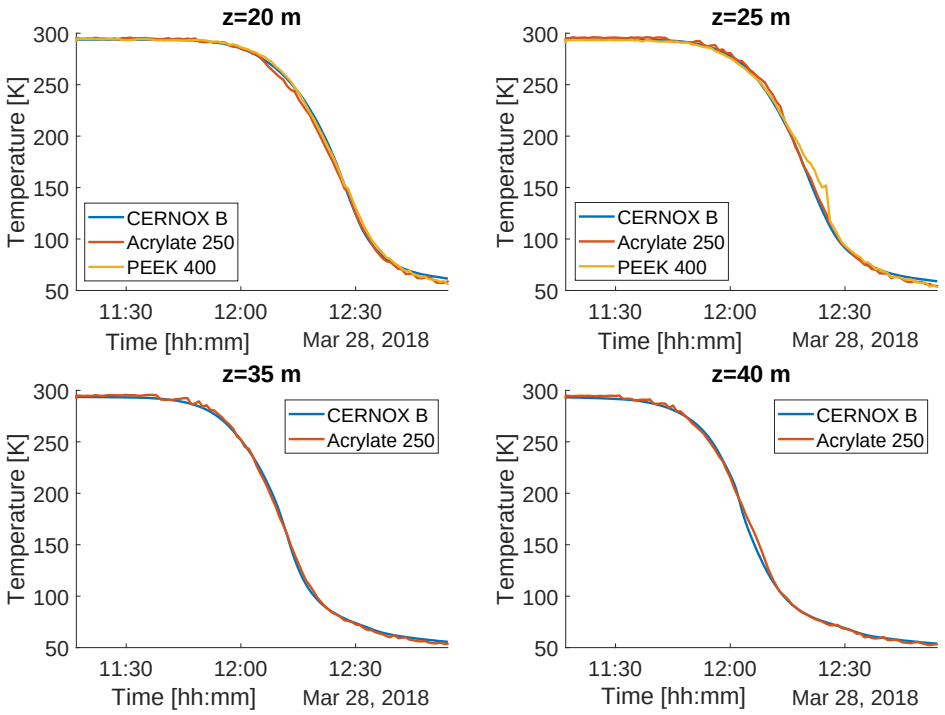

Figure 5.7. *Comparison between the temperatures measured with the CERNOX at different positions and the fiber sensors. Due to the reduced length of the PEEK fiber samples no data were available after $z = 25$ m.*

sensors at four specific location, namely $z_{c,1} = 20$ m, $z_{c,1} = 25$ m, $z_{c,1} = 35$ m and $z_{c,1} = 40$ m. Note that for the last two plot only the temperatures measure by Acrylate 250 were available. As can be seen in Figure 5.7, the temperatures measured by the optical and electrical sensors strongly agrees, proving the quality of the calibration curves used to convert the wavelength shifts and confirming that the OFDR scheme allows proper distributed cryogenic sensing. A little distortion can be seen in the temperature measured by PEEK 400 in position $z_{c,2} = 25$ m, which is however very close to the fiber's end. Since such distortion was not observed in any previous position, as can be seen in Figure 5.6b where there are no evident sharp changes, the distortion was not further discussed.

Observing the measured temperatures as function of the position allows to observe further details that were not discussed so far. The temperature of the SC-Link at three different times is plotted in Figure 5.8 as a function of the position. As can be seen both fibers are represented as well as the temperatures measured by the CERNOX, which however corresponds to only 4 central positions of the full 55 meters of the SC-Link.

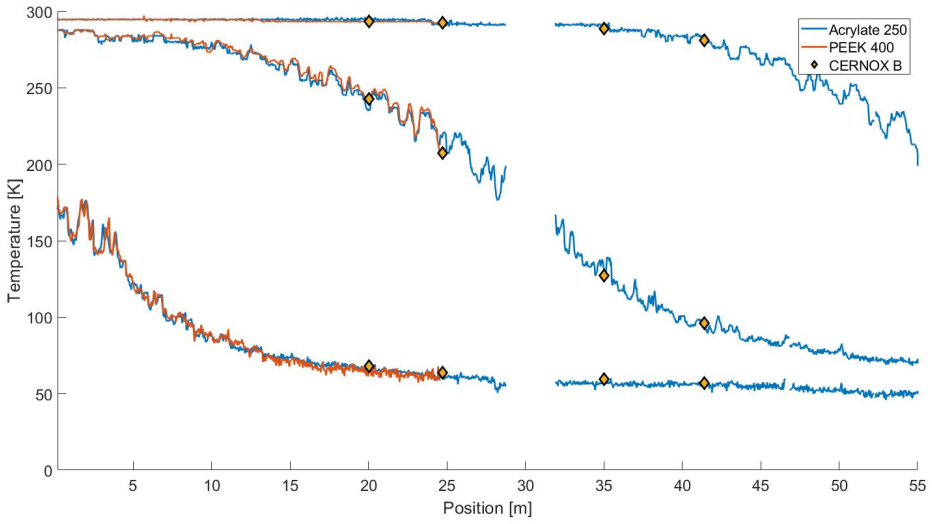

Figure 5.8. *Temperature measured along the fiber sensors at different time. The markers correspond to the temperatures measured with the CERNOX sensors at the same temperatures.*

Figure 5.8 highlight a small increase of the noise affecting the measurement for progressively colder temperatures, as the variance of the trace computed at $t = 12:45$ for temperatures lower than 100 K is higher than the variance of the trace measured at $t = 11:45$ when the temperature was close to 300 K. The distributed evolution of the temperature shown in Figure 5.8 provides reliable informations about the temperature gradient experienced by the superconducting cable and all the other devices in the SC-Link eventually allowing to tune down the cooldown rate to reduce temperature change-induced deformations. Finally, in Figure 5.8 it can be seen that when the temperature gradient is high between neighboring positions, both Acrylate 250 and PEEK 400 experience matching temperature variations of magnitude up to 10 K over relatively small spatial scales. The causes of such temperature fluctuations are not clear and further investigations are being performed.

5.4 Monitoring of a superconducting magnet

High temperature superconducting (HTS) materials are the only option for the generation of magnetic fields exceeding 25 T and for magnets operating over a broad range of temperature and magnetic field for power applications. HTS magnets remain a risky endeavor due to intrinsic differences in their quench behavior (i.e. how they react to a

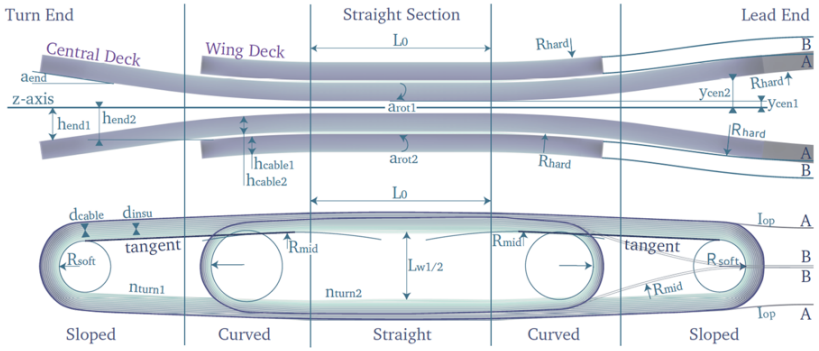

Figure 5.9. *Geometrical scheme of the Feather Magnet 2 with highlighted upper (wing) and lower (center) decks. Figure courtesy of Dr. J. Van Nugteren*

local failure of the superconducting property) relative to low temperature superconductor (LTS) magnets. In particular, HTS magnets have very slow normal zone propagation velocities, on the order of a few millimeters per second, as compared to a few meters per second for LTS magnets. Furthermore, HTS conductor operating limits during a quench are not yet fully understood, and are likely to evolve as the conductor technologies mature. Thus, HTS systems require a novel approach to quench detection that provides sufficient spatial and temporal resolution to detect incipient quenches with sufficient time remaining to protect a magnet.

The last implementation of distributed sensing for cryogenic application discussed in this chapter focus on verifying the possibility of monitoring an HTS magnet. The original objective of the test was the monitoring of a quench, which is an abnormal termination of magnet operation that occurs when part of the superconducting coil enters the normal (resistive) state, but unfortunately no detectable quench was induced close to the monitoring fibers. Nevertheless, the cooldown and the powering of the magnet was monitored, highlighting phenomena that could not be seen with standard sensors.

5.4.1 Experimental setup

The magnet under test was a high temperature superconductor dipole, called *Feather magnet 2*. The dipole was divided into two coils (FM 2.3 and FM 2.4) composed of a lower deck (FM 2.3 LD and FM 2.4 LD) and an upper deck (FM 2.3 UD and FM 2.4 UD) (see Figure 5.9). Each deck was monitored with CERNOX electrical sensors and with optical sensors. The optical sensors could be divided into localized and distributed sensors: one fiber Bragg grating (FBG) array cable and two redundant distributed fiber sensors were embedded in each deck, for a total of three optical fibers per deck

and 12 fibers embedded in the magnet. The distributed fiber sensors monitoring the upper decks were 4m long while the fibers monitoring the lower decks were 13m long. The fibers were wound and glued without pre-tensioning with two-components glue on four thin soft polymeric sheets. The sheets with the fibers were placed above the superconducting wires and covered with the other layers of the magnet. All the layers were then impregnated with epoxy resin. During the assembly of the magnet, one of the FBG arrays and one of the two distributed fiber sensors monitoring FM 2.3 UD were broken on the fiber lead outside the magnet, very close to the optical connector. The fiber leads were too short to splice new connectors, so the broken fibers were discarded and no longer monitored during the tests.

The distributed fiber sensors integrated in the magnet were low bending-losses polyimide coated fibers with total external diameter of 155 μm, provided by LUNA Inc. During the tests they were monitored through two LUNA ODiSI 6104, with 4 measurement channels each. The first ODiSI was used to monitor the distributed fiber sensors in the lower decks and guaranteed up to 50m of sensing length (the total required length was 19m: 13m for the distributed fiber sensors and 6m for feed-through and patch-cords). The spatial resolution was set to 2.6 mm to guarantee the highest possible sampling rate of 3.1 Hz/channel, when monitoring 4 channels (aggregate sampling rate about 12.5 Hz). The second ODiSI was used to monitor the distributed fiber sensors in the upper decks (only 3 of the 4 fibers due to the broken one) and guaranteed up to 10 m of sensing length (the total required length was about 10m: 4m for the distributed fiber sensors and 6m for feed-through and patch-cords). The spatial resolution was again set to 2.6 mm guaranteeing a sampling rate of 16.7 Hz/channel, when monitoring 3 channels (aggregate sampling rate $\approx$50 Hz). All the remote modules were connected to the ODiSIs with standard 50 m stand-off cables connectorized with joint couples of LC/APC connectors. The distributed optical sensors in the magnet were connected to the ODiSI through three different fiber sections. The integrated distributed fiber sensor were connected with FC/APC connectors to three feed-through cables, 2m longs, that ended on the insert of the cryostat through gas-tight connectors. From the insert of the cryostat to the desk there were three more feed-through cables, 3m longs, connectorized with gas tight connectors on one end and FC/APC connectors on the other. The feed-through cables outside the cryostat were connected to the remote modules through hybrid patch-cords FC/APC - LC.

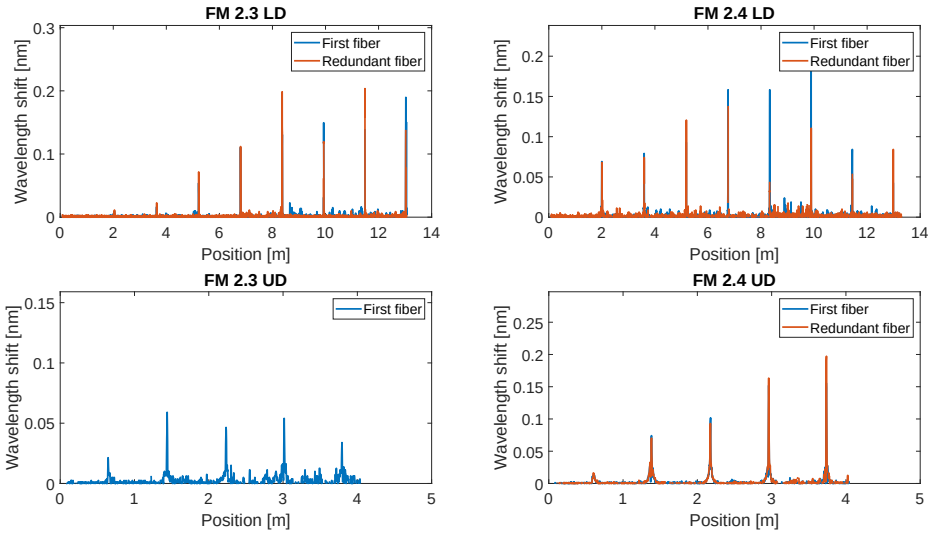

Figure 5.10. *Geometrical calibration of the fibers impregnated in the different coils.*

5.4.2 Results

While the ODiSI represent the measured results on a linear position axis, the fibers inside the coils are wound into concentric rings. A geometrical calibration allows then to identify some known positions of the fiber along the linear z-axis and to map the shifts measured by the ODiSI on the wound geometry of the fibers. The geometrical calibration can be realized thanks to four electrical resistances, called spot-heater, placed on the upper-most positions of the four coil right above the fibers. By powering such resistances while measuring the fiber, multiple peaks will appear in the positions of the linear axis corresponding to the spot-heater, and the map can be easily computed. The results are shown in Figure 5.10, where it can be seen that the fibers in the lower decks exhibits 8 peaks, corresponding to 7 windings, while the lower decks exhibits 5 peaks, corresponding to 4 windings. The mean length of the windings in the lower deck is then $\approx$1.6 meter, while the one in the upper deck is $\approx$ 0.8 meter. A correspondence between the results obtained from redundant fibers can be observed.

The early stages of the magnet cooldown was then monitored and the results for one of the four coils (the others are analogous) are shown in Figure 5.11. As can be seen a periodical pattern corresponding to the multiple winding of the fiber around the coil is clearly visible and has been highlighted by drawing red dashed lines in correspondence to the position of the spot-heater. Since the spot-heater is placed on the upper-most end of the magnet, closer to the current lead and to the insert of the cryostat, the bottom of the coil correspond to the central position between two consecutive red dashed lines.

Since the helium gas is pumped into the cryostat from the bottom, the expected results should highlight a bottom-up cooldown but, as can be seen in Figure 5.11, the first section to cooldown is the one closest to the current lead. This behavior can be explained considering that the fibers are impregnated inside the magnet, thus they are shielded from the temperature changes by a thick layer of copper. While the temperature of the helium reaching the top of the cryostat is warmer than the one exiting the pump at the bottom, it is still sufficiently cold to remove heat from the current leads. Due to their good thermal conductivity however, the heat of the section of the leads that enter the magnets will cooldown as well, and the fiber, which is impregnated just few microns away from the superconducting cable, will measure the change. As time passes, the copper at the bottom of the cryostat will get colder at a faster rate than the current leads, resulting in a temperature distribution consistent with the expectations. As can be seen then, the analysis of Figure 5.11, which is possible only using distributed sensors, allows to investigate phenomena that will be impossible to see using point sensors, either optical or electrical.

By realizing a 3D geometry of the coils of the magnet, and plotting the ODiSI results using the geometrical calibration to map the positions on the geometry, a much clearer representation of the data can be realized, as can be seen from Figures 5.12a and 5.12b. The four coils are colored as functions of the wavelength shift measured, highlighting the early cooldown of the current lead and the final thermalization. Since the number of windings of the superconductor is different with respect to that of the fibers, the final section of the coils in Figure 5.12a and 5.12b does not report any useful data.

When the complete thermalization of the magnet at $T_{FM} = 40K$ was reached, a constant current flow of 800 A was used to power the magnet. At such temperature, due to instrumental limitations, the ODiSI was monitoring only FM 2.4 UD to spot the local heating forecasting a quench. While no quenches were induced close to the fiber, as can be seen in Figure 5.13a we observed a distributed pattern in the measured wavelength shift. Such pattern, that exhibits an equivalent tensile strain on the sides of the coil and a compressive strain on the ends of the coil, can be related to the strain generated on the structure by the magnetic field-induced Lorentzian forces. Due to the small current flow, the wavelength shift induced was particularly low and the measurement resulted noisy, so a second test was performed raising the amplitude of the current flow to 2000 A. The results are shown in Figure 5.13b, where a much stronger shift is visible and a

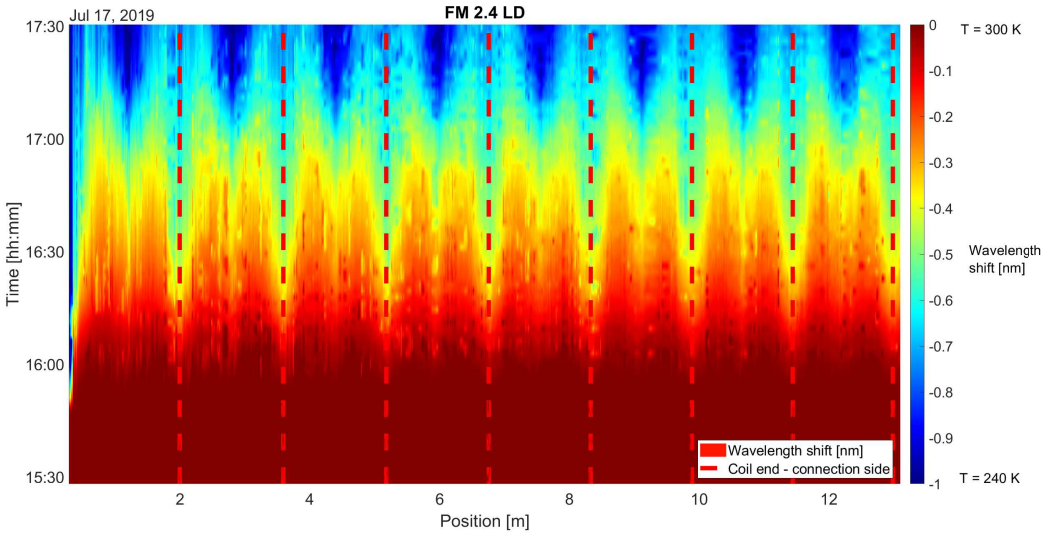

Figure 5.11. *Distributed cooldown of the coil FM 2.4 LD.*

more defined pattern appears. As can be seen, the side of the coil tries to push on the edge to achieve a more circular shape.

5.4.3 Conclusion

In this section the results of the monitoring of an HTS magnet performed with distributed optical fiber sensors based on OFDR was reported. In particular both the cooldown and the powering of the magnet were observed with high spatial resolution and sensitivity. The monitoring of the HTS magnet with the distributed sensors allowed to highlight details in the dynamic of the cooldown that point sensors, both optical and electrical, could not easily identify. The knowledge that some sections of the magnet were cooling down earlier than other is fundamental as the temperature gradient may induces dangerous deformations. Moreover, the strain induced during the powering due to Lorentzian forces may lead to a further analysis of the distribution of the current along the superconducting cable or to an independent measurement of the amplitude of the current flow.

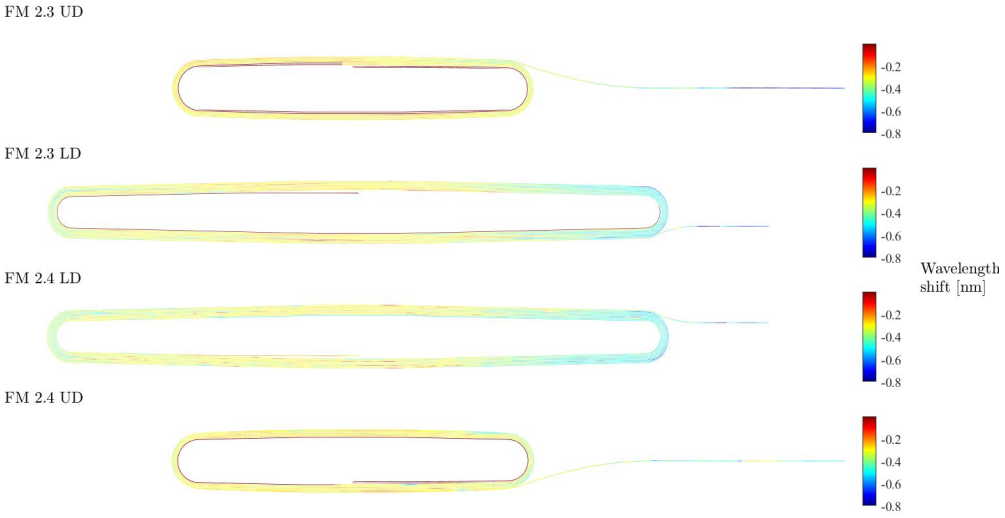

(a)

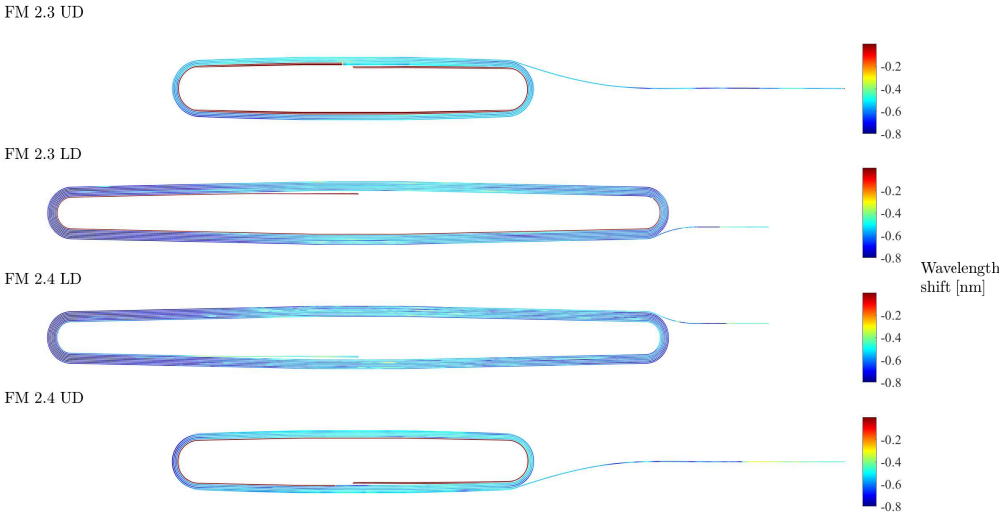

(b)

Figure 5.12. *(a) 2D representation of the magnet cooldown at* $t = 16:30$. *(b) 2D representation of the magnet cooldown at* $t = 17:15$.

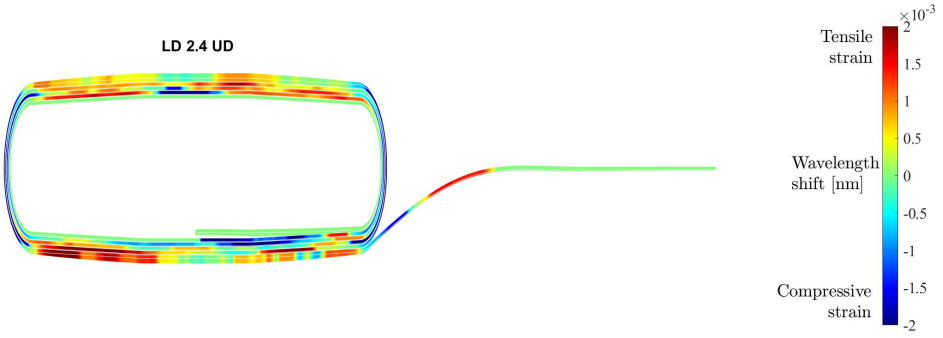

(a)

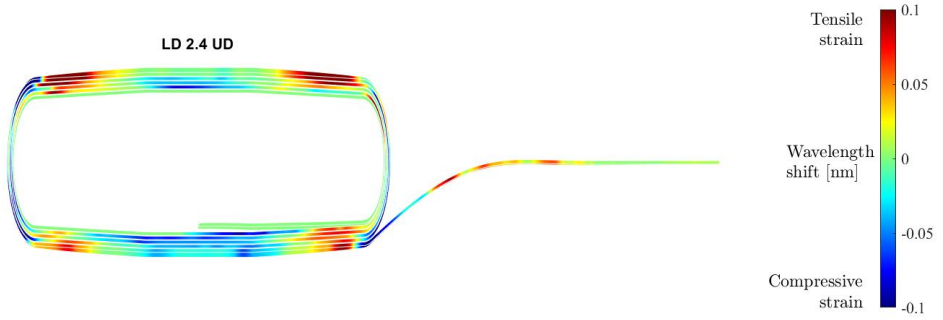

(b)

Figure 5.13. *(a) 2D representation of the wavelength shift experienced by FM 2.3 UD for a current $I = 800$ A (b) 2D representation of the wavelength shift experienced by FM 2.3 UD for a current $I = 2000$ A*

Bibliography

[1] A. Chiuchiolo, L. Palmieri, M. Consales, M. Giordano, A. Borriello, H. Bajas, A. Galtarossa, M. Bajko, and A. Cusano, "Cryogenic-temperature profiling of high-power superconducting lines using local and distributed optical-fiber sensors," Opt. Lett. **40**(19), 4424 (2015).

[2] I. Latka, W. Ecke, B. Höfer, C. Chojetzki, and A. Reutlinger, "Fiber optic sensors for the monitoring of cryogenic spacecraft tank structures," Proc. SPIE 5579, 195 (2004).

[3] R. Rajinikumar, K. G. Narayankhedkar, G. Krieg, M. Suber, A. Nyilas, and K. P. Weiss, "Fiber Bragg gratings for sensing temperature and stress in superconducting coils," IEEE Trans. Appl. Supercond. **16**(2), 1737-1740 (2006).

[4] H. Zhang, F. Deng, Q. Wang, L. Yan, Y. Dai, and K. Kim, "Development of strain measurement in superconducting magnet through fiber Bragg grating," IEEE Trans. Appl. Supercond. **18**(2), 1419-1422 (2008).

[5] S. W. James, R. P. Tatam, A. Twin, M. Morgan, and P. Noonan, "Strain response of fibre Bragg grating sensors at cryogenic temperatures," Meas. Sci. Technol. **13**(10), 1535 (2002).

[6] S. Gupta, T. Mizunami, T. Yamao, and T. Shimomura, "Fiber Bragg grating cryogenic temperature sensors," Appl. Opt. **35**(25), 5202 (1996).

[7] C. Lupi, F. Felli, A. Brotzu, M. A. Caponero, and A. Paolozzi, "Improving FBG sensor sensitivity at cryogenic temperature by metal coating," IEEE Sens. J. **8**(7), 1299 (2008).

[8] R. RajiniKumar, M. Suesser, K. G. Narayankhedkar, G. Krieg, and M. D. Atrey, "Performance evaluation of metal-coated fiber Bragg grating sensors for sensing cryogenic temperature," Cryogenics **48**(3-4), 142 (2008).

[9] T. Mizunami, H. Tatehata, and H. Kawashima, "High-sensitivity cryogenic fibre-Bragg-grating temperature sensors using Teflon substrates," Meas. Sci. Technol. **12**(7), 914 (2001).

[10] R. Martins, P. Caldas, B. Teixeira, J. Azevedo, J. Monteiro, J. H. Belo, J. P. Araujo, J. L. Santos, and G. Rego, J., "Cryogenic temperature response of reflection-based phase-shifted long-period fiber gratings," Lightwave Technol. **33**(12), 2511 (2015).

[11] L. Thévenaz, A. Fellay, M. Facchini, W. Scandale, M. Niklès, and P. A. Robert, "Brillouin optical fiber sensor for cryogenic thermometry," Proc. SPIE **4694**, 22 (2002).

[12] C. D. Boyd, B. D. Dickerson, and B. K. Fitzpatrick, "Monitoring distributed temperatures along superconducting degaussing cables via Rayleigh backscattering in optical fibers," in Proceedings of the Intelligent Ships Symposium **IX**, 25-26, 2011.

[13] X. Lu, M. A. Soto, and L. Thévenaz, "MilliKelvin resolution in cryogenic temperature distributed fibre sensing based on coherent Rayleigh scattering," Proc. SPIE **9157**, 91573R (2014).

[14] Y. Du, T. Liu, Z. Ding, Q. Han, K. Liu, J. Jiang, Q. Chen, and B. Feng, "Cryogenic temperature measurement using Rayleigh backscattering spectra shift by OFDR," IEEE Photon. Technol. Lett. **26**(11), 1150 (2014).

[15] L. Palmieri and L. Schenato, "Distributed Optical Fiber Sensing Based on Rayleigh Scattering," The Open Optics Journal **7**(1), 104-127 (2013).

[16] M. Sabaeian, H. Nadgaran, M. De Sario, L. Mescia, and F. Prudenzano, "Thermal effects on double clad octagonal Yb: glass fiber laser," Opt. Mater. **31**(9), 1300 (2009).

[17] J. Komma, C. Schwarz, G. Hofmann, D. Heinert, and R. Nawrodt, "Thermo-optic coefficient of silicon at 1550 nm and cryogenic temperatures," Appl. Phys. Lett. **101**(4), 041905 (2012).

[18] "OBR 4600", *Luna, defying impossible.*, 30th November 2019, https://lunainc.com/product/sensing-solutions/obr-4600/.

Chapter 6

Conclusions

6.1 Summary

In this thesis the results achieved during my three-year long research in the Ph.D. program have been proposed. Thanks to the chance of collaborating with different research groups on both theoretical and practical applications of Rayleigh backscattering-based optical fiber sensors, my knowledge in the field has grown to the point that I realize how far I am from a deep understanding of the topic. Nevertheless, I am confident in the robustness of the foundations build to so far that will definitely help with my future objectives. As specified in the first chapter, in this thesis different results have been discussed:

About optical time domain reflectometry, an original mathematical model describing the stress induced virtual perturbations measured by a chirped-pulse ϕ-OTDR has been developed and experimentally validated. The application of such method in the estimation and correction of stress-induced virtual perturbation allows further improvements in the quality of the measurements performed with chirped-pulse ϕ-OTDR. Moreover, the issue of limited spatial resolution of the OTDR-based sensors have been tackled by developing a method that allows a 15-fold improvement without significant changes in the setup and with almost null drawbacks.

In optical frequency domain reflectometry, a novel algorithm exploiting the phase of the Rayleigh backscattering signal have been developed. Such algorithm allows to realize distributed acoustic sensing with high acoustic bandwidth up to tens of kilohertz and spatial resolution of centimeters.

Finally the early results of the experiments performed in collaboration with European

Organization for Nuclear Research have been discussed, proving the advantages that distributed sensing provides with respect to standard point-based electrical sensors. The possibility of computing the calibration curves of different samples of fibers at cryogenic temperatures as low as 5 K has been shown, as well as the possibility of using them to monitor the cooldown of a 55 meters long superconducting power cable. Distributed sensors shows great performance also while monitoring the powering of an HTS magnet, highlighting phenomena that could not be seen with traditional sensors.

6.2 Future works

During these three-years many issues have been investigated and solved, but there are still details that require further work. About the research performed on optical time domain reflectometry, while the spatial resolution may be improved using sub-bands processing, the total chirp in each sub-band is reduced with respect to the original pulse, thus proportionally limiting the maximum measurable temperature or strain change. This issue can be readily avoided by comparing traces separated by a small temporal windows and keeping trace of the previous changes, but the cumulative noise induced by frequent updates of the traces used for the measurement may become a significant issue. Moreover, to avoid distortions in the linear chirp generated by the Mach-Zehnder modulator, the magnitude of the chirped side-bands of the input pulse was reduced, limiting the maximum measurement range. More precise techniques to realize the chirped side-bands or different way to add the optical carrier to the input pulse, without increasing the phase noise, must be then researched.

The algorithm proposed to realize high-resolution, high-bandwidth acoustic sensing with an OFDR shows excellent results, but in some situation the measurement may exhibits low SNR, due to the intrinsic issues occurring when dealing with phase signals. A method to extract more stable phase signal, or to reduce the impact of phase noise must be researched.

Finally, while distributed cryogenic sensing exhibits clear advantages with respect to standard electronic-based point sensors, due to its relative novelty it still appears too unreliable. Many situations have been observed where, for issues related to the interrogation systems, or to an incorrect deployment of the fibers, or to a break, etc. it became impossible to perform the measurement or to obtain reliable results. Since it is evident

that standard sensors are not enough anymore for the cryogenic applications under research, and given the benefits that robust distributed sensing may provide, more studies should be done to improve the robustness of optical-fiber based sensors.

As a final remark, while the performance of distributed sensors may be already competitive, the costs of the interrogation systems are still too high. Such costs limit the diffusion of distributed systems in the market to universities and large research centers. More research need then to be invested in realizing cost-effective setups that will allow a distributed sensing to become a commercially available standard.